CHARACTER OF THE DIATOM ASSEMBLAGE SPANNING A DEPOSITIONAL TRANSITION IN THE EASTERN EQUATORIAL PACIFIC OCEAN AT 6.6 Ma

A Thesis

by

BRIAN NEVILLE BROOKSHIRE JR.

Submitted to the Office of Graduate Studies of
Texas A&M University
in partial fulfillment of the requirements for the degree of

MASTER OF SCIENCE

December 2003

Major Subject: Oceanography

CHARACTER OF THE DIATOM ASSEMBLAGE SPANNING A DEPOSITIONAL TRANSITION IN THE EASTERN EQUATORIAL PACIFIC OCEAN AT 6.6 Ma

A Thesis

by

BRIAN NEVILLE BROOKSHIRE JR.

Submitted to the Office of Graduate Studies of
Texas A&M University
in partial fulfillment of the requirements for the degree of

MASTER OF SCIENCE

Approved as to style and content by:

Jack Baldauf (Chair of Committee)	Niall Slowey (Member)
John Firth (Member)	Anne Raymond (Member)
Wilford Gardner (Head of Department)	

December 2003

Major Subject: Oceanography

ABSTRACT

Character of the Diatom Assemblage Spanning a Depositional Transition in the Eastern Equatorial Pacific Ocean at 6.6 Ma. (December 2003)

Brian Neville Brookshire Jr.,

B.S., Eckerd College

Chair of Advisory Committee: Dr. Jack Baldauf

Approximately 6.6 million years ago in the Eastern Equatorial Pacific a large increase in biogenic mass accumulation rates (MAR's) occurred. This increased level of biogenic mass accumulation persisted until about 4.4 Ma at which time levels returned to those similar to before the transition at 6.6 Ma. The exact nature of the change that facilitated this transition in biogenic MAR's, however, was not understood. Here we present the results of a study which characterizes the diatom assemblage spanning the depositional transition at 6.6 Ma from sediments taken from ODP Hole 850B. A close inspection of lithology reveals a clear change in lithology from a diatom nannofossil ooze to a nannofossil diatom ooze at 6.6 Ma. This transition is immediately followed by the occurrence of laminated diatom ooze (LDO). Diatom absolute abundance data reveals three levels of productivity associated with pre-transitional, post-transitional, and LDO formational sediments. An increase in the absolute abundance of *Thalassionema nitzschioides* was the major contributor to the formation of post-transitional, and LDO sediments. The known ecological preferences of this species indicate an overall increase

in nutrient availability followed by sporadic changes in nutrient availability. These changes in nutrient availability could be associated with the establishment, or increase in strength, of an upwelling cell and/or the increase in nutrients made available via upwelling due to a shoaling of the thermocline.

ACKNOWLEDGMENTS

I would like to thank my advisor, Jack Baldauf, for his support and guidance throughout the process of completing my thesis. He always pointed me in the right direction, but was wise enough to allow me to assess problems, and make decisions for myself - a collective lesson that will benefit me through all of my scientific endeavors. I would also like to thank my other committee members: Niall Slowey - for his support, confidence and for opening numerous windows of opportunity for me during my time here at Texas A&M. John Firth - for his valuable suggestions and for his insights on microscopic methods, and Anne Raymond - for her "out of the box" perspective which helped me to assess critical problems in a different light. I would also like to thank the Ocean Drilling Program and the GCR crew (Phil Rumsford and Bruce Horan) for use of multiple facilities and, often, much needed assistance. Finally, I would like to thank Sandy Drews for keeping me on track and on time in regards to numerous aspects of my life here at Texas A&M.

TABLE OF CONTENTS

Page

LIST OF TABLES

LIST OF FIGURES

FIGURE Page

INTRODUCTION

The Eastern Equatorial Pacific (EEP) is one of the most productive oceanic regions in the world, with estimates of annual new production as high as 56% of the global total [1]. The EEP also plays an extremely important role in the flux of CO_2 from the ocean to the atmosphere. It is estimated that about 0.7 to 1.5 Pg of carbon a year as CO_2 is released to the atmosphere from areas of equatorial upwelling. The EEP supplies as much as five times the amount of carbon to the atmosphere as all other equatorial upwelling sites combined [2]. Therefore, it is easy to understand why this region is of importance in terms of global nutrient and carbon cycling. However, the extent to which the EEP has influenced global nutrient and carbon cycling throughout the geologic past is not nearly as certain. This uncertainty stems from the changes in oceanic and tectonic conditions, such as the closure of the Isthmus of Panama, and the associated oceanographic adjustment that occurred during Neogene. Particularly, the interruption of flow between the Pacific and Atlantic Oceans effected equatorial flow and water mass characteristics, and the locus of deep thermohaline water mass formation [3-5]. Also, the proposed commencement of the East Asian paleomonsoon cycle around 7.2 million years ago (Ma), and the associated changes in global trade wind strength, could have played a significant role in upwelling intensity [6].

Numerous studies indicate substantial changes in biogenic mass accumulation

---

This thesis follows the style and format of *Nature.*

rates (MAR's) in the EEP throughout the late Cenozoic [5,7,8]. Biogenic opal MAR's range from less than 1 g/cm^2/ky to greater than 3 g/cm^2/ky. Biogenic carbonate MAR's range from less than 1 g/cm^2/ky to greater than 6 g/cm^{2}ky [5]. Between 6.7 Ma and 6.6 Ma there is an abrupt increase in biogenic opal MAR's from less than 0.2 g/cm^2/ky to greater than 2.5 g/cm^2/ky. Laminated diatom ooze (LDO) also occurs discontinuously between approximately 15.0 Ma and 4.4 Ma [9,10]. The period of high biogenic mass accumulation continued until approximately 4.4 Ma when rates dropped to levels equal to or below those prior to the transition at approximately 6.6 Ma. The transition itself is marked by the occurrence of LDO in the sedimentary record. The large range in biogenic accumulation rates, and the discontinuous occurrence of LDO in the sedimentary record point to the variable nature of primary production during the late Neogene in the EEP.

This study characterizes trends in the diatom population during the transition from low to high biogenic mass accumulation at 6.6 Ma. This study focuses on the change in relative and absolute abundance, and the emergence and disappearance of ecologically indicative species. Understanding the variation in diatom composition and abundance contributes to our understanding of the paleoceanographic significance of this transition, and the occurrence of LDO in the sedimentary record.

BACKGROUND AND PERTINENT RESEARCH

1. Tectonic Setting

The EEP ocean, east of about 115º W, and between about 10º N and 5º S, overlays a complex tectonic region. Here the sea floor is composed of three lithospheric plates: the Pacific Plate to the west, the Cocos Plate to the northeast, and the Nazca Plate to the southeast. The divergent boundaries between these plates form the East Pacific Rise and Galapagos spreading centers (Figure 1). The differential spreading along these ridges must be considered when conducting paleoceanographic reconstructions due to the temporal changes in location of the sea floor. It is estimated that the rate of rotation of the Pacific plate is approximately 0.79º/m.y. [11]. Extrapolated estimates of the rate of motion for the Caribbean Plate suggest that the portion of Central America south of the Yucatan began its estimated 1,400 km migration from the then leading edge of the Caribbean Plate about 8 Ma [12]. The final closure of the Isthmus of Panama estimated from records of land mammal migration, isotopic shifts, and changes in biogenic sedimentation rates [4,5,13,14], commenced about 11 Ma and terminated between 3.5 and 4.5 Ma. The closure was a sequential process mediated by the motion of the Caribbean Plate and the shoaling of the sill within the Panamanian Seaway. Subsequently, oceanographic adjustment in the region occurred over an extended period of time resulting from the sequential interruption of deep, intermediate, and shallow circulation between the Pacific and Atlantic. This interruption of equatorial circulation between the

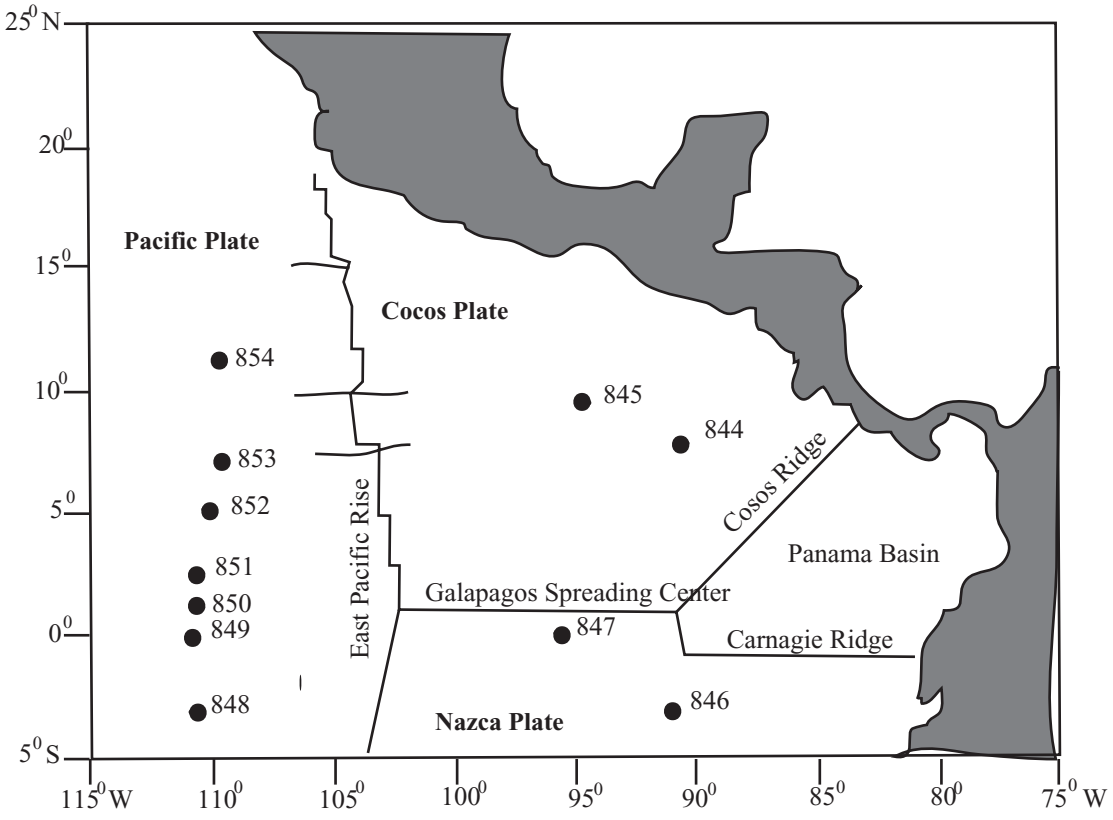

Figure 1 Current plate configuration in the EEP[5].

Pacific and Atlantic had significant effects on EEP circulation, and potentially the locus of maximum deep water formation [3].

The late middle Miocene collision of Australia with Indonesia is proposed to have played an integral role in the establishment of current equatorial oceanographic conditions. This tectonic reorganization created a barrier between the westward flowing north and south Pacific equatorial currents and the Indian Ocean. As a result, a pressure gradient was established between the western and eastern Pacific due to water pileup in the western Pacific [15]. It has been speculated that the initiation of this pressure gradient led to the formation of the equatorial undercurrent (UC) [8].

2. Current Oceanographic Setting

Surface Currents

Surface to intermediate circulation in the equatorial Pacific results from a complex mosaic of forcing mechanisms. Frictional coupling between the westward flowing northeast and southeast trade winds and the ocean surface provides the momentum necessary to drive the north and south equatorial currents. The area of relatively weakened wind stress lying between the northeast and southeast trade winds, termed the doldrums, also plays an important role in equatorial circulation. As a result of the meridional change in wind stress across the equator, a process known as wind curl occurs. This drives the eastward flowing north equatorial countercurrent (Figure 2A) [15].

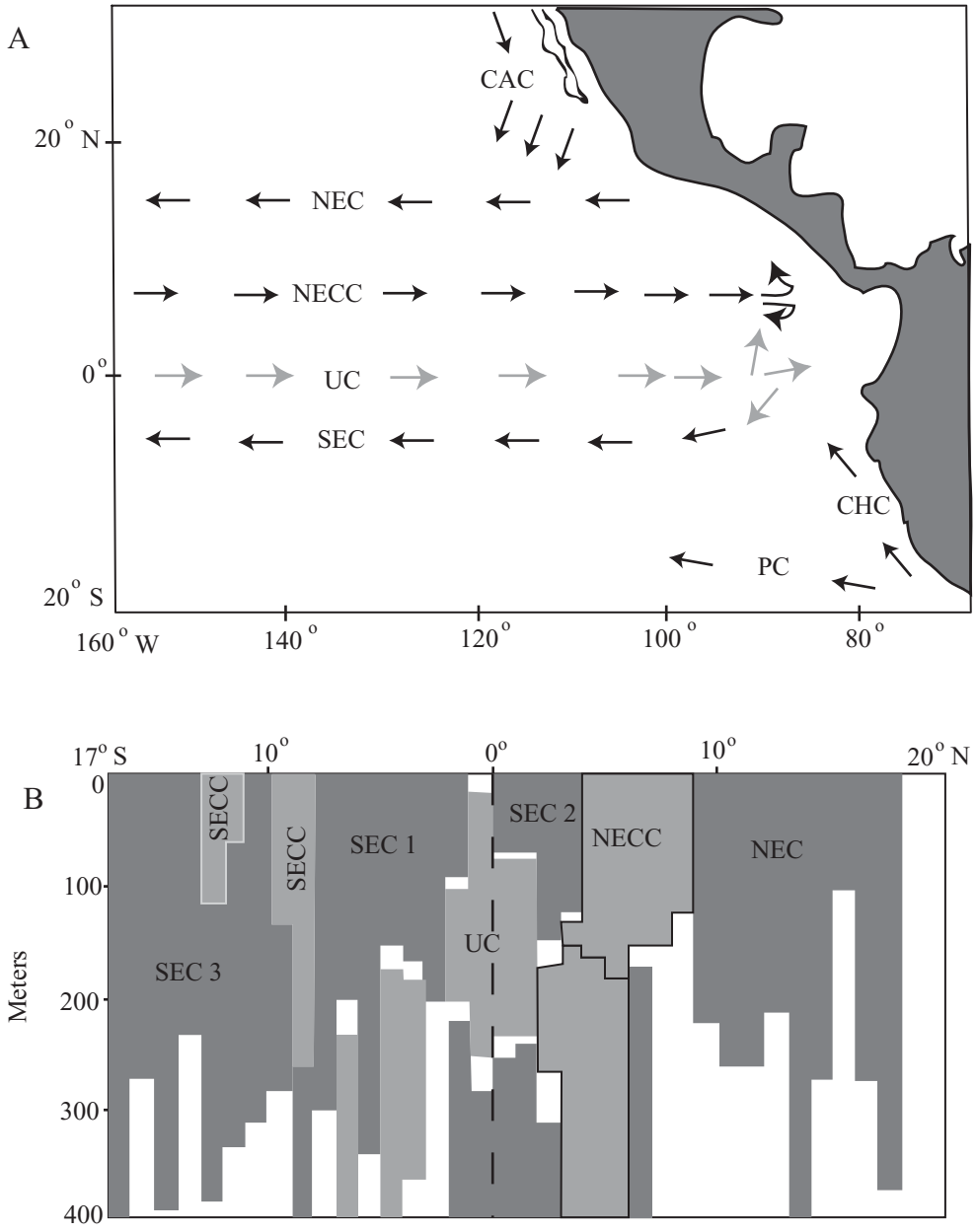

Figure 2 The equatorial current system. A = Map showing the proximal relationship of equatorial surface currents;[69] B = Vertical profile showing proximal relationship of equatorial surface and subsurface currents (SEC = South Equatorial Current, NEC = North EquatorialCurrent, NECC = North Equatorial Countercurrent, SECC = South Equatorial Countercurrent, UC = Equatorial Undercurrent) [16].

The strongest current in the equatorial Pacific system in terms of volume transport is the westward flowing South Equatorial Current (SEC). The total transport of the SEC is approximately 55 Sv [16], and it is separated into three branches due to the equatorial divergence, and the relatively weak south equatorial counter current (SECC), which occurs between about 8º and 10º S. The main branch (SEC 1) occurs between the equator and 8ºS with an approximate speed of 5cm sec^{-1} extending to a depth of 300 m along its southern flank. The second branch of the SEC (SEC 2) occurs between the equator and 4º N , and extends down to a depth of 150 m. This section of the current has a transport of 15Sv [16]. The third branch of the SEC (SEC3) occurs between approximately 9º and 17º S (Figure 2A & B).

The westward flowing North Equatorial Current (NEC) occurs between 9º and 18ºN. This current has a mean transport of 23.3 Sv [16], and extends to a depth of approximately 300 m. This current has a subsurface split around 15ºN. The SEC and NEC are divided by the eastward flowing North Equatorial Counter Current (NECC), which occurs between 2º and 6ºN. This current transports approximately 19.8 Sv [16], and extends to a depth of approximately 170 m (Figure 2A & B).

Equatorial Undercurrent

The UC is a subsurface current flowing along the equator between 2ºN and 2ºS with a mean transport of 32.3 (±3.5) Sv [16,17]. It originates in the western Pacific at a depth of about 280 m and flows eastward, shoaling to depths as shallow as 40 m between about 110º and 90ºW. It reaches a maximum speed of 102 cm sec^{-1} at 130 m depth

(Figure 2A & B)[16,17]. This current occurs primarily as a result of the pressure gradient between the western and eastern Pacific. This pressure gradient exists due to the pileup of warm surface waters in the western Pacific derived from the NEC and SEC [15].

Associated Divergences and Convergences

Divergence and convergence in the equatorial Pacific (most notable in the eastern equatorial Pacific) facilitate the formation of distinct hydrographic boundaries, and have marked effects on the horizontal and vertical distribution of chemical and biological parameters. There are two areas of divergence in the equatorial current system. Along the equator, Ekman driven divergence occurs due to the westward flow of the SEC along the equator, and the change in sign of the Coriolis parameter at 0º. At the boundary between the NECC and the NEC Ekman driven divergence occurs due to the westward flow of the NEC and the eastward flow of the NECC associated with displacement to the right in the northern hemisphere due to the Coriolis parameter. As a result of the surface water divergence, and the necessity of conservation of mass, upwelling occurs in these regions. Productivity along the equator in the eastern Pacific is increased due to the upwelling of nutrient rich water originating near the core of the UC [16] (Figure 2). Convergence occurs at the boundary between the SEC and the NECC due to the westward movement of the SEC and the eastward movement of the NECC (and associated displacement due to Coriolis). This convergence forms a sharp chemical/biological boundary often evident by the coagulation of biogenic particles on one side or the other [9,18].

3. Modern Chemical Processes

As a result of the upwelling of subsurface waters in the EEP, atmosphere/ocean chemical exchanges are greatly effected. The upwelling of this water represents one terminus of the conveyor belt of deep and intermediate water thermohaline circulation. Consequently, this water brings large quantities of CO_2, derived from the atmosphere to ocean flux at temperate and high latitudes, back in contact with the atmosphere. In fact, the equatorial Pacific is responsible for emitting 0.35 – 0.79 Gt-C yr^{-1} to the atmosphere. This represents about five times the amount of CO_2 supplied to the atmosphere from the corresponding areas of equatorial divergence in the Atlantic and Indian Oceans [2].

Upwelling also has a great impact on nutrient availability in the EEP. Transport of nutrient rich waters from below the euphotic zone provides the potential for greatly enhanced primary production (Figure 3)[19]. Nitrate concentrations in the upwelling regions of the equatorial Pacific are greater than 4uM. However, despite the high primary productivity in the region, all of the available nutrients are not utilized [1,20]. The EEP is referred to as a high nutrient low chlorophyll (HNLC) area[21-23]. Specifically, HNLC refers to the disproportionately low concentration of chlorophyll in relation to the supply of biolimiting nutrients. This is assumed to be a direct result of inadequate availability of iron to the region. Iron is a primary element affecting uptake efficiencies of nitrate and silica [24-26].

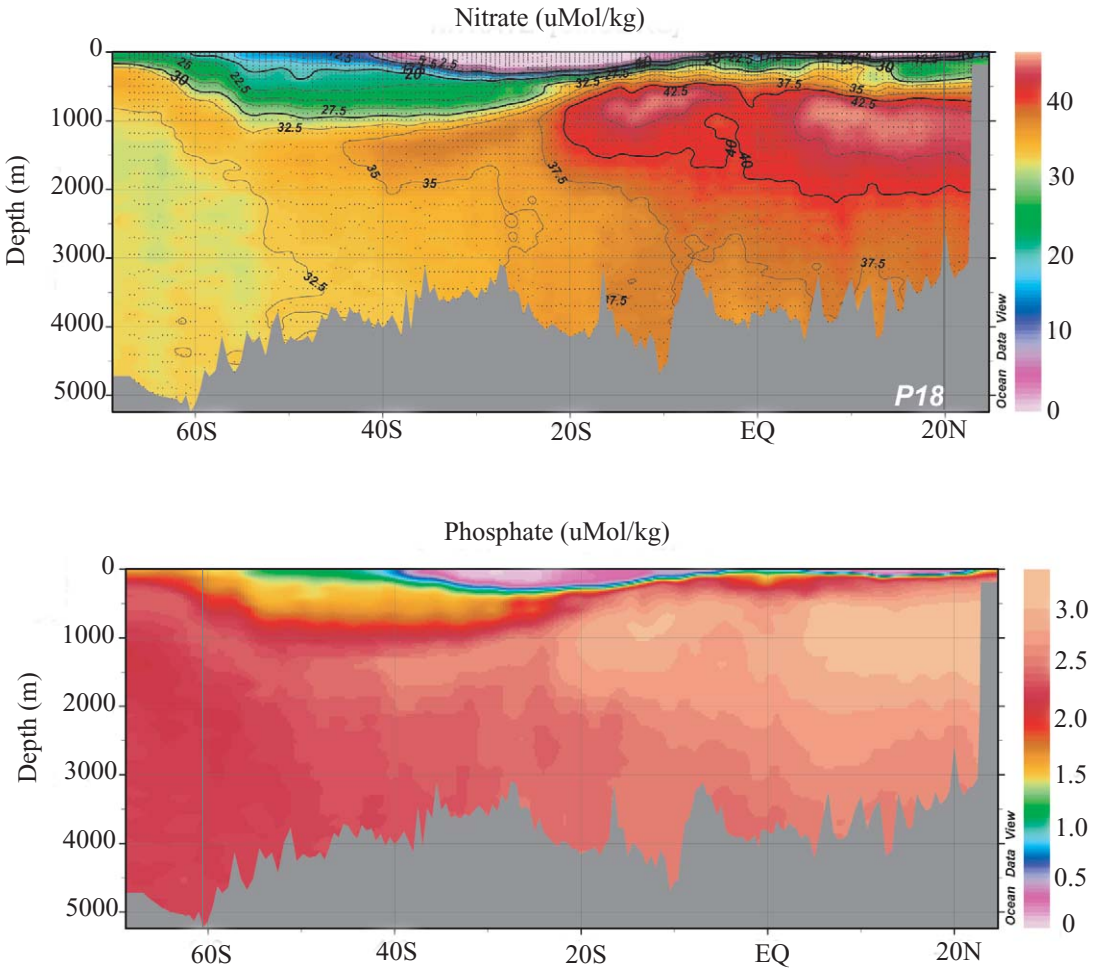

Figure 3 Meridional nutrient profiles at 110^0 W compiled from eWOCE data[19].

4. Modern Biological Processes

Along 110º W primary production rates range from 755 (+–304) mg C m^{-2} day^{-1} to 894 (+–238) mg C m^{-2} day^{-1} (depth integrated values averaged between 5º N and 5º S). The total autotrophic biomass ranges from 17.2 (+– 4.5) µg C l^{-1} to 27.1 (+–3.5) µg C l^{-1} [27]. Here, as with the majority of the equatorial Pacific, the phytoplankton assemblage is dominated by small solitary organisms typically less than 5um in size. The major components are dinoflagellates, eukaryotic picoplankton, *Synechococcus*, haptophytes, and prochlorophytes [27]. Diatoms are found in abundance in areas of active upwelling and near hydrographic fronts. The assemblage is typically composed of small *Pseudonitzschia spp*., *Thalassionema spp., Thalassiothrix spp*., *Thalassiosira spp*., *Chaetoceros spp*. and *Rhizosolenia spp*. [27-31]. In some instances, such as during El Nino/La Nina events, coagulated mats of *Rhizosolenia spp.* formed along the frontal boundary of tropical instability waves can dominate the near surface assemblage [18,29].

5. Regional Paleoceanography

Previous Work in Diatom Paleoceanography/Chronostratigraphy

A great many individuals have contributed to the understanding of diatom biostratigraphic zonations and low latitude assemblages found in the eastern equatorial Pacific. Burkle's numerous early contributions [32-34] laid the framework for this collective effort. Further investigations by Barron[35], and most recently by Baldauf and

Iwai[36] led to the biostratigraphic model we have for the eastern equatorial Pacific today. Barron's work in the equatorial Pacific[37], along with Schrader's work in the north Pacific and equatorial Indian Oceans[38,39] provide the basis for our understanding of the tropical diatom assemblage throughout the Cenozoic.

Sancetta[40,41] was perhaps the first to emphasize the "overwhelming predominance" of the *Thalassionema* and *Thalassiothrix* generas in upper Miocene equatorial Pacific sediments. She also noted rapid species turnover in the upper Miocene and numerous extinctions at the Miocene/Pliocene boundary, which she attributed to environmental instability. Baldauf[42], and also Barron[43,44], noted the high relative abundance of *Thalassionema nitzschioides* in Late Miocene sediments underlying areas of high productivity. These authors concluded that pulses in cold-water diatom species such as *Thalassionema nitzschioides* indicate increased upwelling and perhaps episodes of increased polar cooling.

Ocean Drilling Program (ODP) Leg 138 Contribution

Numerous paleoceanographic studies have been conducted in the EEP that have contributed to our understanding of the coupled physical, chemical, and biological processes that have influenced this region throughout the geologic past[3-5,8,9,14,35,36,42,45-52]. Many of these studies are resulted from ODP Leg 138, which recovered sediments along two meridional transects, one along 110ºW, and the other between 95º and 100ºW. The latter transect was partitional. Two sites were occupied in the area of the Costa Rica Dome between about 7º and 11º N, and two sites were occupied in the vicinity of the

Galapagos Islands between about 0º and 5º S (Figure 4). Together, these transects span the equatorial circulation system encompassing all major hydrographic boundaries. A total of eleven sites were occupied, and multiple holes were cored at each site. Composite sedimentary sequences were constructed from offset core sections in adjacent holes using physical properties data and graphic correlation techniques [47]. The combination of high sedimentation rates (in excess of several centimeters per thousand years), and the acquisition of near continuous composite sedimentary sequences provided the basis for a well constrained chronology. Chronological control points were provided by magnetostratigraphic [53] and biostratigraphic [36,54,55] means. Multiple paleontological indicator species, including diatoms, nannofossils, and radiolarians, were utilized in the determination of biostratigraphic control points. This combined evidence provided the age control needed for stratigraphic and geochemical correlation.

Farrell et al.[5] documented three distinct sedimentary events in the upper Neogene stratigraphic record based on the Leg 138 results. These events are similar to those recognized previously by several workers [7,8,56,57]. First, beginning about 11.2 Ma and continuing to approximately 9.4 Ma was the "carbonate crash". The reduction of carbonate MAR's was a stepwise process with the greatest reduction occurring at approximately 9.5 Ma. At this time carbonate mass accumulation nearly ceased in the EEP (dropping from levels often much greater than 1 $gcm^{-2}ky^{-1}$), with levels above 0.2 $gcm^{-2}ky^{-1}$ recorded only at Sites 850 and 851 (Figure 4). Lyle et al.[4] speculated that this peak in carbonate dissolution occurred due to the shoaling of the calcite compensation

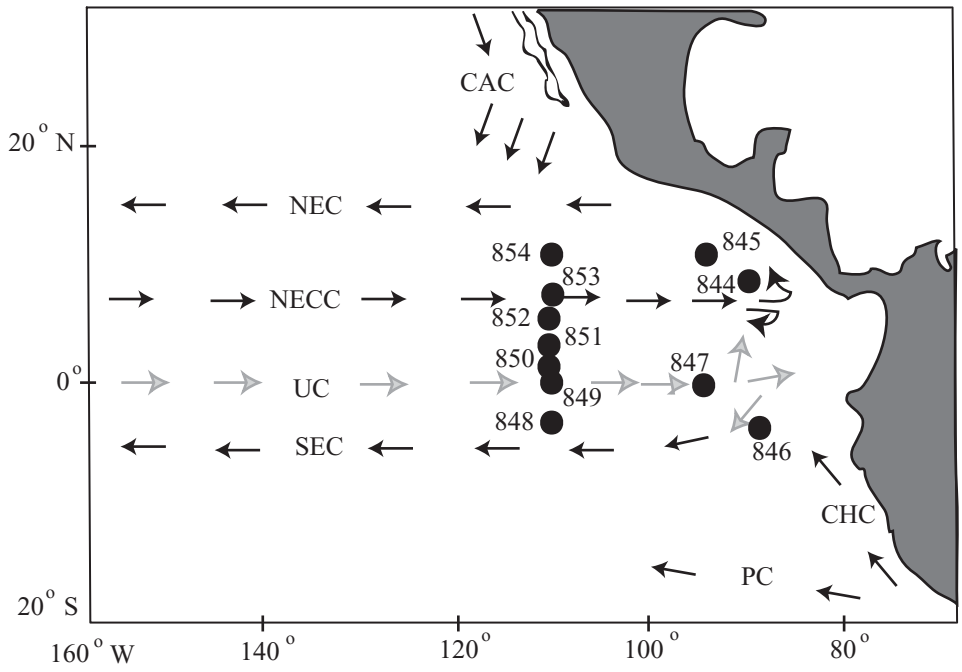

Figure 4 Location of Leg 138 sites in relation to major currents.[69]

depth (CCD) as a result of the restriction of less corrosive deep water flow from the Atlantic through the Panamanian Seaway [4].

Second, between 6.6 and 4.5 Ma, was the "biogenic bloom". During this period, biogenic sedimentation rates dramatically increased along the equator. Carbonate MAR's increased from less than 4 $gcm^{-2}ky^{-1}$ to greater than 6 $gcm^{-2}ky^{-1}$ at Sites 846, 847, 849, 850, and 851, with a peak value (Figure 5) at Site 850 of 15.23 $gcm^{-2}ky^{-1}$ at approximately 5.8 Ma. Similarly, opal MAR's increased from less than 1 $gcm^{-2}ky^{-1}$ to greater than 2 $gcm^{-2}ky^{-1}$ at Sites 846, 849, 850, and 851, with a peak value at Site 849 of 4.92 $gcm^{-2}ky^{-1}$ at approximately 6.6 Ma (Figure 6). The initiation of the "biogenic bloom" is thought by previous workers to coincide with the shoaling of the Panamanian sill to approximately 150 m [46]. The dramatic increase in biogenic MAR's suggests that this potentially effected upwelling dynamics and or nutrient availability by interrupting the flow of intermediate water (i.e. – the equatorial undercurrent) from the Pacific to the Atlantic. The transition to the period of high biogenic sedimentation at approximately 6.6 Ma is marked by the occurrence of LDO in the sedimentary record.

Third, at about 4.4 Ma a distinct and permanent shift in the locus of maximum opal deposition from Sites 849 and 850 along the western transect to Sites 846 and 847 in the Galapagos area occurred. This coincides closely with the speculated time for the final closure of the Panamanian Seaway.

Kemp et al.[9] recognized possible causes for diatom mat formation and deposition, and LDO preservation in the sedimentary record. They speculate that the diatom mats formed as a result of specific surface water conditions, and were coagulated

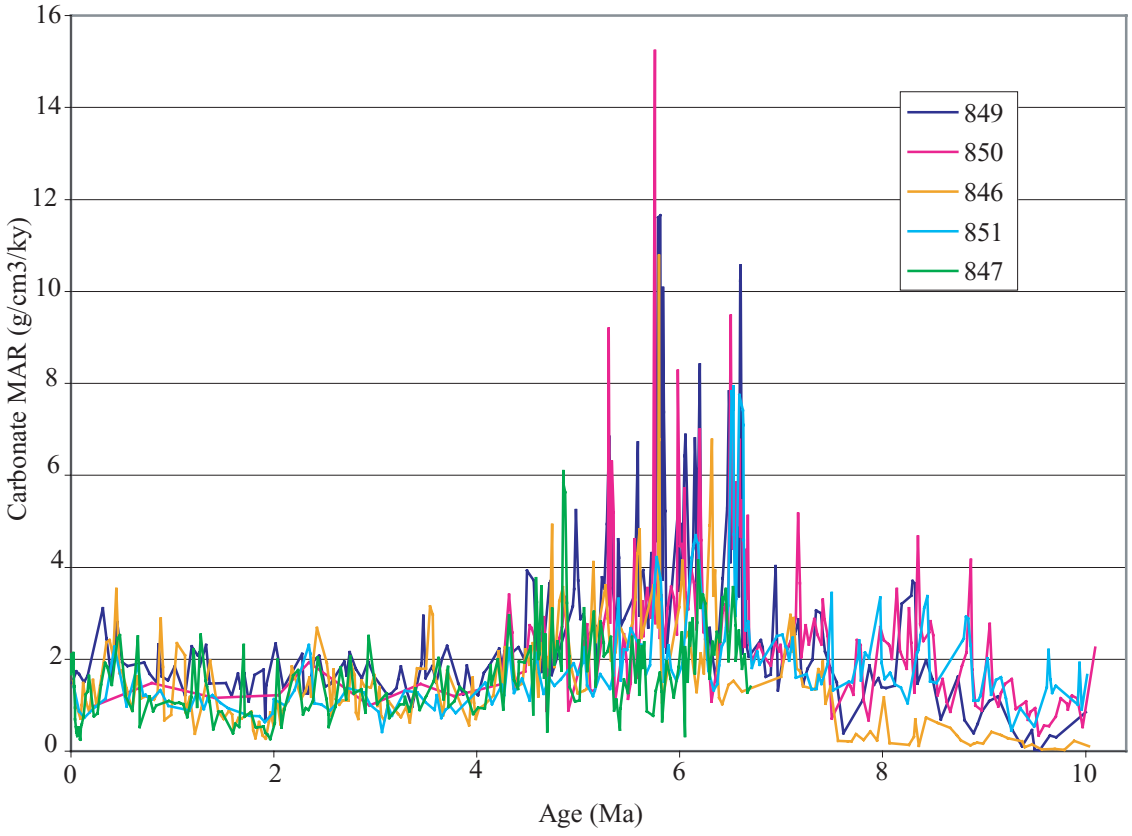

Figure 5 Carbonate mass accumulation rates over the last 10 Ma for select ODP Leg 138 Sites [69].

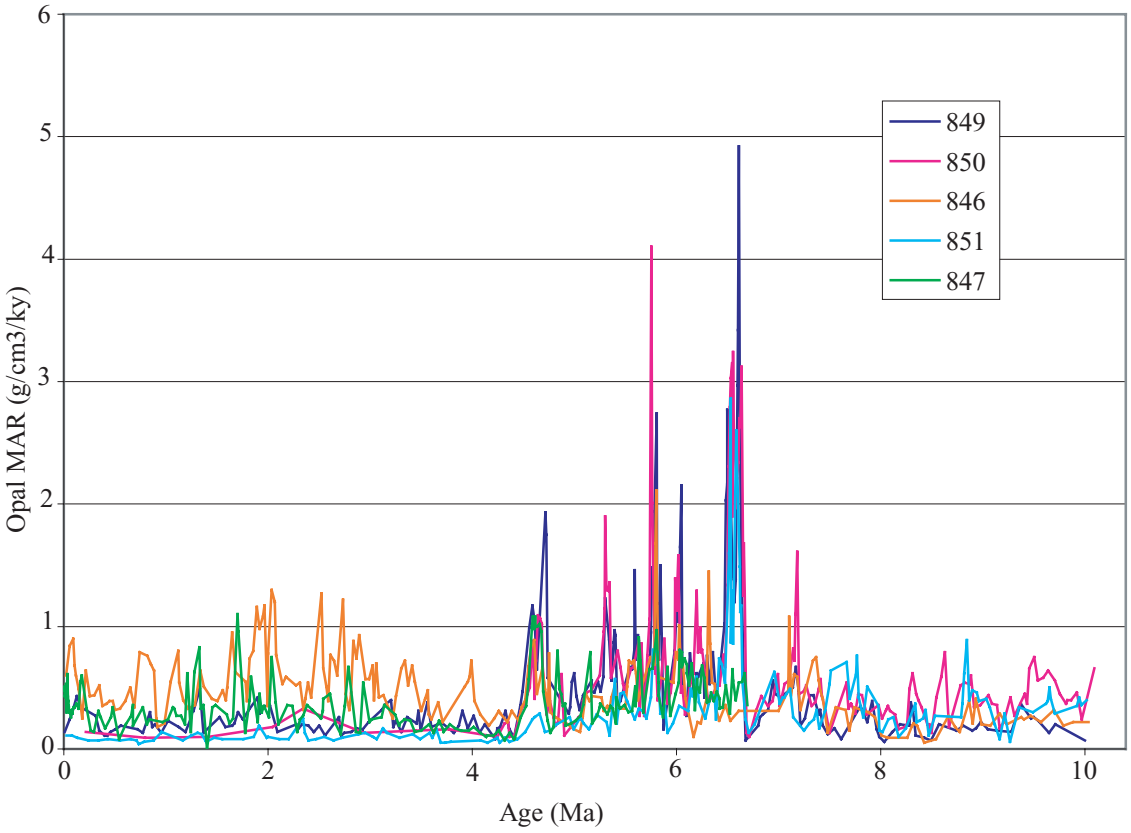

Figure 6 Opal mass accumulation rates over the last 10 Ma for select ODP Leg 138 sites [69].

along convergent boundaries (SEC and NECC) during the migration of hydrographic fronts (Figure 7). This agrees well with observations by Yoder et al.[18] of the contemporary formation of coagulated diatom mats along the boundary between the SEC and the NECC associated with the propagation of tropical instability waves. LDO deposits have been characterized as typically occurring as "packets" between 10 and 20 meters thick. Within these large packets are three scales of alternation. These scales occur at the submillimeter, millimeter to centimeter, and decimeter level[10]. At the submillimeter level, packets have been described as being near monospecific, mixed-assemblage, and nannofossil-rich. Of the described sequences, the typical progression consists of *Thalassiothrix longissima* specific laminae composed of approximately 25 individual *T. longissima* mats (average thickness 20 μm) interbedded with mixed and nannofossil-rich laminae[58]. The millimeter to centimeter level is described as alternations between nannofossil-bearing diatom ooze[58] and a "purer" diatom ooze. The decimeter level is characterized by the alteration of LDO and non-laminated/bioturbated beds[10]. Observations revealed that laminated sequences were of sufficient tensile strength to impede bioturbation[49].

Shackleton and Hall[52] conducted isotopic analysis of bulk sediments (representing surface water fractionation) from Leg 138 sites and discovered a synchronicity between an oxygen isotopic shift, and the increase in biogenic sedimentation at Sites 849, 850, and 851 during the period of the "biogenic bloom". At the peak of the biogenic bloom, there was a positive oxygen isotopic shift of greater than

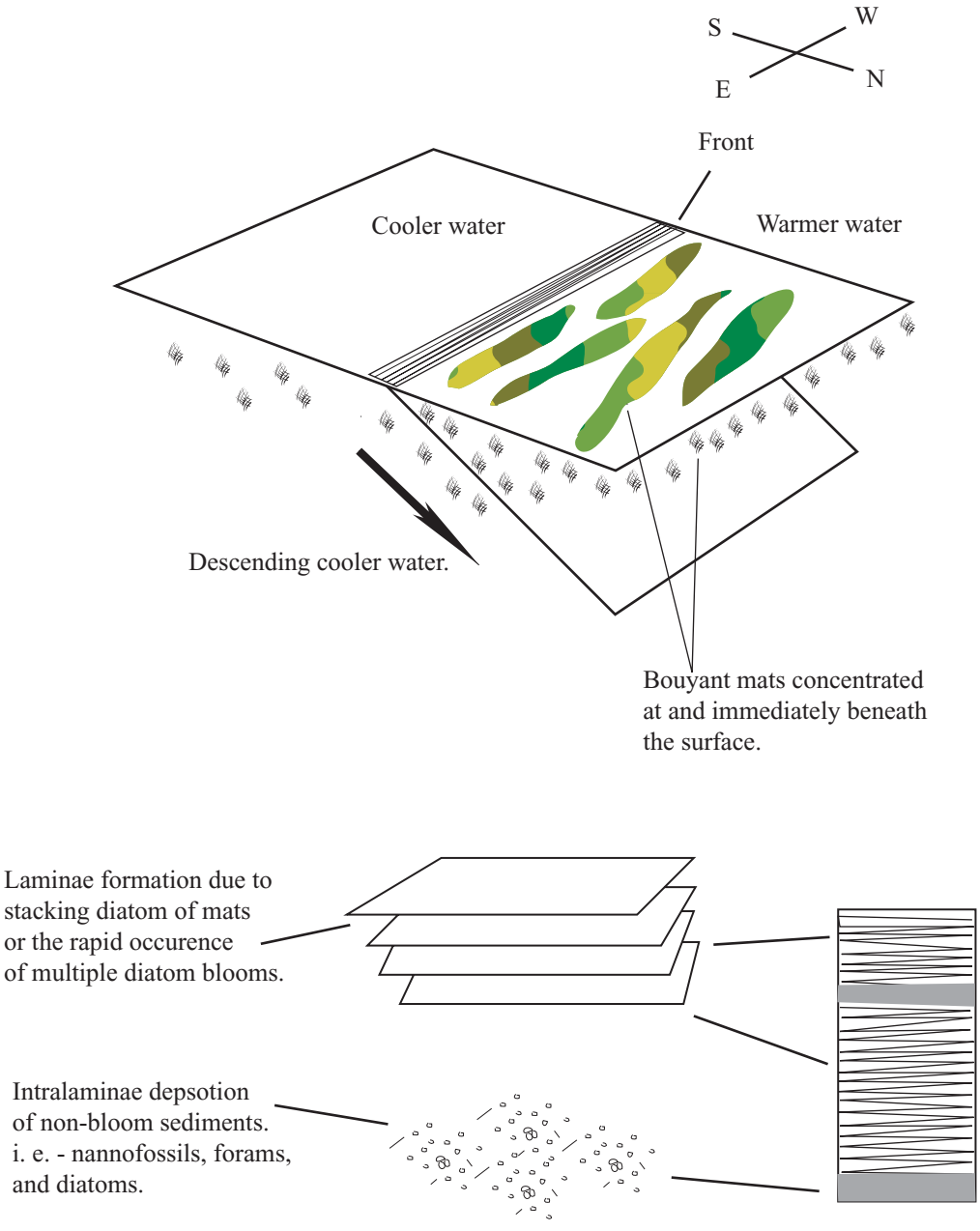

Figure 7 Model for diatom mat production and LDO preservation [9].

1‰. This evidence suggests an increase in equatorial divergence and /or shoaling of the thermocline during the period of the biogenic bloom relative to today.

RESEARCH AND METHODS

1. Objectives

The primary objective of this project is to better understand the diatom paleoecology over a 113 Ky period during which the transition from low to high productivity, which occurred at approximately 6.6 Ma in the EEP. In order to accomplish this, slides prepared from processed silica residues were counted to determine the absolute abundance of all species observed. Once collected, these data were statistically analyzed to determine any trends in absolute abundance and/or change in species composition during the period of interest. The secondary objective of this project is to utilize these data in a comparative study to assess paleoceanographic changes that might have facilitated the increase in biogenic sedimentation rates. In order to accomplish this, comparisons will be made with previously established diatom paleoecological data [9,10,35-37,40-42,44,45,49,56,59-65], and current diatom assemblage data [18,27,28,30,31,66-68]. By establishing paleo and modern analogues, these data will provide valuable insight into the changing paleoceanographic conditions of the EEP during the Late Miocene.

2. Eastern Equatorial Pacific Study Site

ODP Site 850, representative of sediments deposited beneath the area of equatorial divergence, was selected for sampling because it displays the sharpest

occurrence, and best preservation of LDO among the Leg 138 sites for the interval of interest. This site displays relatively good biostratigraphic age constraints. However, considering the narrow interval to which this study addresses, the available constraints are sparse, occurring at approximately 6.54 and 6.69 Ma [36]. Yet, due to the weak magnetic signal, and the lack of biostratigraphicaly useful events, these constraints provide the only control points for this and adjacent (849 and 851) sites. Two holes were cored at Site 850. Hole 850A is located at 1º 17.837' N, 110º 31.283' W at a water depth of 3797.1 m below sea level (mbsl) (Figure 4). Penetration was 74.2 meters below sea floor (mbsf). The total length of core recovered was 77.12 m, with a total core recovery of 103.9%. Values greater than 100% for core recovery occur because of expansion of the cored material as it is brought up from depth. Hole 850B is located at 1º 17.827' N, 110º 31.286' W at a water depth of 3786.1 mbsl. Penetration at this hole was 399.8 mbsf. The total length of core recovered was 393.58 m, with a total core recovery of 99.2%.

3. Lithostratigraphy/Physical Properties

The upper 76 m at Site 850 consists of calcareous nannofossil ooze with varying amounts of diatoms, foraminifera, and radiolarians. Below this, the major lithology is a pale yellowish gray (N8 to 5Y8/2) diatom nannofossil ooze. Also occurring is nannofossil diatom ooze, which is interbedded with diatom laminae (LDO). The most

notable LDO occurrences are between about 192 and 213 mbsf. These sediments range in color from light to dark yellow olive gray (5Y 6/3 to 5Y 7/2) [58,69].

Numerous physical properties measurements were conducted on cores from Site 850. Of particular importance to this study was the acquisition of a continuous record of GRAPE density at a frequency of one measurement per 2 cm. This information can be used as a viable, high resolution, proxy for bulk density and carbonate content [70]. The continuous and high frequency nature of GRAPE density measurements also makes this a valuable tool for graphic correlation [47,71].

4. Sampling Strategy

During periods of the sedimentary record where LDO occurs, interpolation between scattered age control points to devise a linear sedimentation rate is not adequate. LDO represents the massive, geologically instantaneous, flux of coagulated diatom mats to the sea floor [9,29,49,72]. Therefore, in order to accurately sample the transition from low to high productivity at approximately 6.6 Ma, a linear sedimentation rate (LSR) had to be determined that accounts for the occurrence of LDO. The only available age constrains for this period are the first occurrence of *Thalassiosira praeconvexa* (6.69 Ma)[36] between 214.9 and 212.8 mbsf and the first occurrence of *Thalassiosira miocenica* and *Thalassiosira convexa* (6.54 Ma)[36] between 206.9 and 203.1 mbsf (the midpoint of the depth constraints for the biostratigraphic markers was used as the reference depth). The total depth encompassed by LDO between the two

available age constraints was subtracted as a geologically instantaneous event. The results suggest a linear sedimentation rate of approximately 4.43 $cmyr^{-1}$ between the age control points. This estimate differs from that utilized by Shackleton and Hall[52] (approximately 5.93 $cmyr^{-1}$) in constructing their oxygen isotope chronology, because they did not consider the relatively instantaneous nature of the LDO. Using this LSR, and assuming a constant sedimentation rate for the non-laminated sequences, the age of the first LDO was determined to be approximately 6.6 Ma. This approximates the actual transition into a high productivity regime. Samples taken from 215 to 210 mbsf represent approximately 113 Ky.

5. Analysis

Weighing/Chemical Processing

The 5 cm^3 samples were taken using sample tubes above and below the LDO interval. No less than 0.5 cm of sediment was removed from the portion of the sample that was in contact with the core tube. This was to ensure the removal of the "rind" created by flow-through between the core and barrel. Following this, an approximately 0.25-0.5 cm thick disc was removed and examined. The amount of heterogeneity (color variation) in the sub-sample was recorded.

A quarter round section was taken from the LDO interval to insure the preservation of the laminae in their correct orientation. This quarter round section was sub-sampled using an osmotic/electric knife in order to isolate the thinnest samples

possible (approximately 0.1 cm) spanning the occurrence of diatom laminae. The thin samples insure that time averaging is at a minimum.

Prior to processing, the samples were placed in a glass vial and allowed to dry at low heat for 24 hours. After drying, approximately 0.0200 to 0.005 grams of sediment (depending on percent silica) was weighed out and washed from the weighing paper with 2 mL of de-ionized (DI) water into a 40 mL vial. The sediment was disaggregated for weighing by gently breaking off chunks of the appropriate weight from the dried sample. This was done, as opposed to powdering the sample, in order to keep frustule fragmentation at a minimum. Following weighing and transfer to the vial, 2 mL of 30% H_2O_2 was added, and the vial was placed in a warm DI water bath and allowed to react for about 4 to 6 hours. Following the oxidation of all organic matter, 2 mL of HCl was added to the vial to dissolve all carbonates. This reaction usually took less than an hour. After all the carbonates were dissolved, 10 mL of sodium hexametaphosphate was added to aid in the disaggregation of flocculated particles. The sediment was allowed to disaggregate for no more than one hour [73]. This insured that the sediment did not settle to the bottom of the vial and re-flocculate. Following disaggregation, DI water was added until the meniscus reached the break in the top of the 40 mL vial (this was predetermined to represent 43 mL).

Settling Apparatus and Procedure

The settling apparatus and procedure follow the same basic design as outlined by Scherer[73]. The settling chamber is a 1000 mL glass beaker. Within this chamber is

placed the settling platform. The settling platform is composed of a raised square plastic slab. The feet were sanded to ensure the platform is as stable and level as possible. One corner of the platform was drilled and fitted with 0.25 inch glass tubing which extends through the platform. The glass tubing remains stationary about 0.5 cm above the bottom of the beaker. Attached to the top of the glass tubing, which extends to just beyond the lip of the beaker, is soft latex hosing (Figure 8A). The other end of the hosing is fitted with a plastic stopcock. The tubing is held in place above the beaker, and directed into the sink by two stationary clamps.

Particles were settled onto pre-cleaned glass cover slips. The glass cover slips were coated with a starch solution produced from rubbing DI water over a freshly sliced potato. This solution was then applied in a thin layer to the cover slip with a gloved hand. The cover slips were then allowed to air dry. Once dried, two cover slips were mounted to a glass microscope slide with a small amount of rubber cement (Figure 8B). This was to ensure that the slips remained relatively stationary during mixing, and also that they could be handled without disturbing the silica residue prior to permanent mounting [73].

The settling chamber was assembled and the mounted cover slips were placed on the platform. Following this, 870 mL of DI water was funneled into the chamber (Figure 8A & B). The silica residue was then shaken well for several seconds and two drops of wetting agent were added to the residue. Immediately following the addition of the wetting agent, the silica residue was added to the chamber at the same time that the water in the chamber was mixed with an up and down motion using a perforate plunger

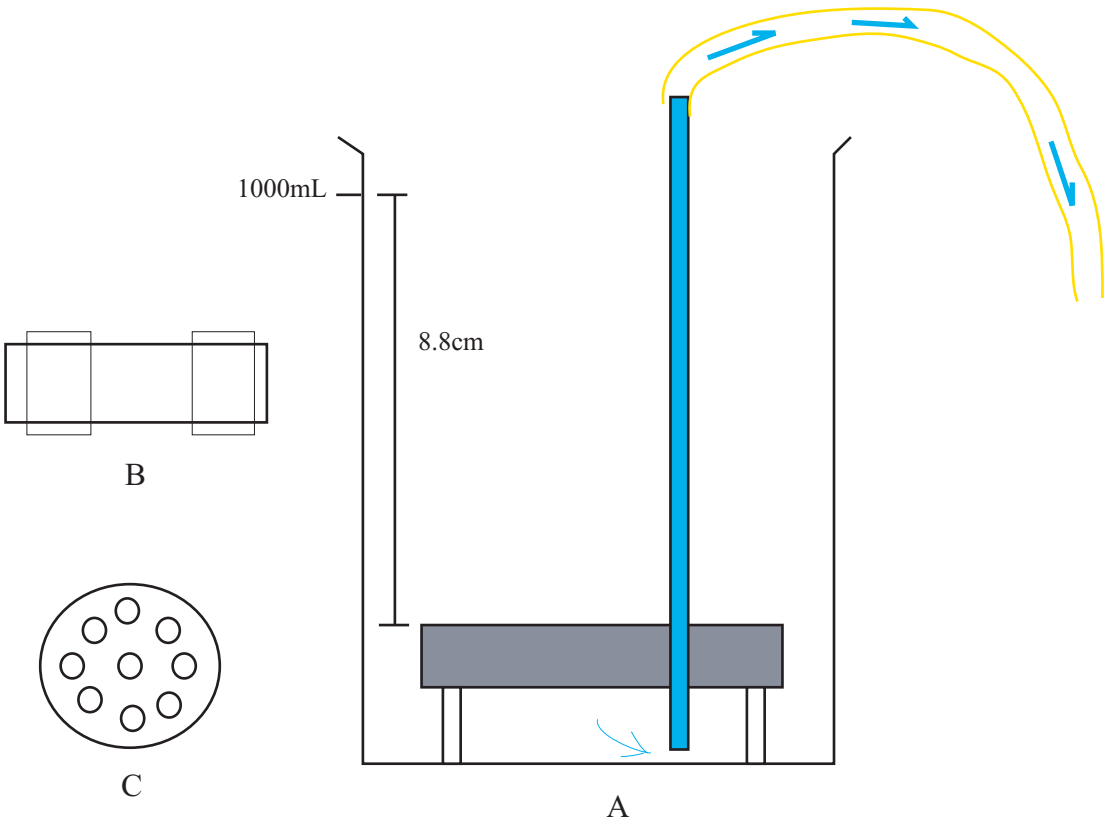

Figure 8 A = settling chamber; B = settling medium; C = perforate plunger.

(Figure 8C). The vial was then rinsed with 10 mL of DI water which was added to the chamber. This brings the total volume of material (fluid and settling platform) to 1000 mL. Mixing was continued for approximately one minute, following which the plunger was shaken into the chamber to avoid loss of material. The chamber was then covered and allowed to sit undisturbed for at least 40 hours.

Following settling, a siphon was established using a pipette pump, and the chamber was allowed to drain completely at a rate no higher than 4 mL per minute. The siphoning procedure has no effect on the cover slips because the water was siphoned from below the platform at an extremely slow rate. Once the chamber was drained, the cover slips were allowed to dry for at least 24 hours and then permanently mounted to microscope slides using Hyrax mounting medium.

Counting Procedure

The counting procedure follows the method outlined by Shrader and Gersonde [74]. A total of no less than 300 frustules were counted from each slide at a magnification of x788 [73,75]. The number of fields of view observed in order to count 300 frustules was also recorded. Following counting, three transects were scanned along the long axis of the cover slip, and three transects were scanned along the short axis of the cover slip. This was done to include uncommon taxa not observed during tabulation.

Relative Abundance Calculation

Relative abundance is determined using the following equation:

$$[VC/VT * 100]\ [v/v]$$

$$= \text{percent total}$$

Where:

VC = valves counted (per individual species) [v]

VT = total valves counted per slide [v]

Counts to 300 valves gives a confidence interval of 95% for encountering any species present in a concentration of 1% or higher[79].

Absolute Abundance Determination

Absolute abundance is determined by using the following equation:

$$[\{(VC/(FV * VFV)) * VW\}/IWS\}]\ [(vcm^3/cm^3)/g]$$

$$= \text{absolute abundance [v/g]}$$

Where:

VC = valves counted [v]

FV = number of fields of view

VFV = volume above field of view = area of field of view * 8.8 [cm]

VW = volume of water in beaker = 923 [cm^3]
Silica residue = 43 mL
Rinse = 10 mL
Water = 870 mL

IWS = initial weight of sample [g]

Initial Counts

Initial counts reveal a percent error similar to that reported by Scherer for estimates of absolute abundance. The initial counts were conducted on material processed from the same sediment sample. Of three counts, two were conducted on slides from the same settling chamber at an initial sample weight of 0.02785 g, and the third was conducted on a slide from a separate settling chamber at an initial weight of 0.03417 g (Table 1). This yields an error of approximately plus or minus 4.4 percent. However, the actual error is probably lower than this because at a weight of 0.03417 g the diatoms are somewhat layered on the slide (too dense). This leads to underestimates of total abundance. During actual data collection, the initial weight of the samples was varied between 0.0200 and 0.0050 g based on the abundance of diatom frustules in the sediment. This was determined by making smear slides, and also by trial and error. Slide densities were kept low enough to avoid layering and underestimation of total frustule abundance.

These initial counts also reveal an excellent statistical correlation between individual species absolute abundance ($r^2 = >0.9$). These initial counts were conducted as a check on the reproducibility of the method. The results suggested that further, extensive counts were not warranted. Numerous studies have tested and documented the reproducibility and accuracy of this method [73,75-78].

Table 1 Absolute abundance calculated from initial counts.

Sample (g)	Abundance (v/g)
0.02785 a	1.1×10^8
0.02785 b	1.2×10^8
0.03417	9.8×10^7

RESULTS

1. Initial Results

Sedimentary Interval

Initial estimates of the temporal occurrence of LDO between 215 and 210 mbsf were based entirely on core descriptions produced by the shipboard party of ODP Leg 138. These estimates were sufficiently accurate to determine the depth range of material necessary to sample in order to encompass the onset of LDO production. These estimates were also used to determine a precursory linear sedimentation (as discussed above). However, prior to sampling, core sections deemed to contain LDO by the shipboard party were described in detail. Along with descriptions, smear slides were produced in order to gain a rough idea of percent silica. All material between 214.30 and 210.60 mbsf was observed and described in detail (Figure 9). Sediments between 214.30 and 211.83 mbsf consist of a diatom nannofossil ooze with no sharp contacts and moderate to heavy burrowing (30-60% of core surface). Millimeter scale LDO may be present at 211.99 mbsf and 212.06 mbsf. Sediments between approximately 211.83 and 211.69 mbsf consist of a nannofossil diatom ooze with no evident burrowing. There is a sharp color contact between this nannofossil diatom ooze (5Y 7/2) and the diatom nannofossil ooze (5Y 8/1) below. No laminations are visible by direct observation within this interval. Between approximately 211.69 and 211.65 mbsf there is a dark brown chert layer (5Y 4/2). This layer has been crumbled as a result of the drilling process, however, observations of paracontemporaneous material from Site 849

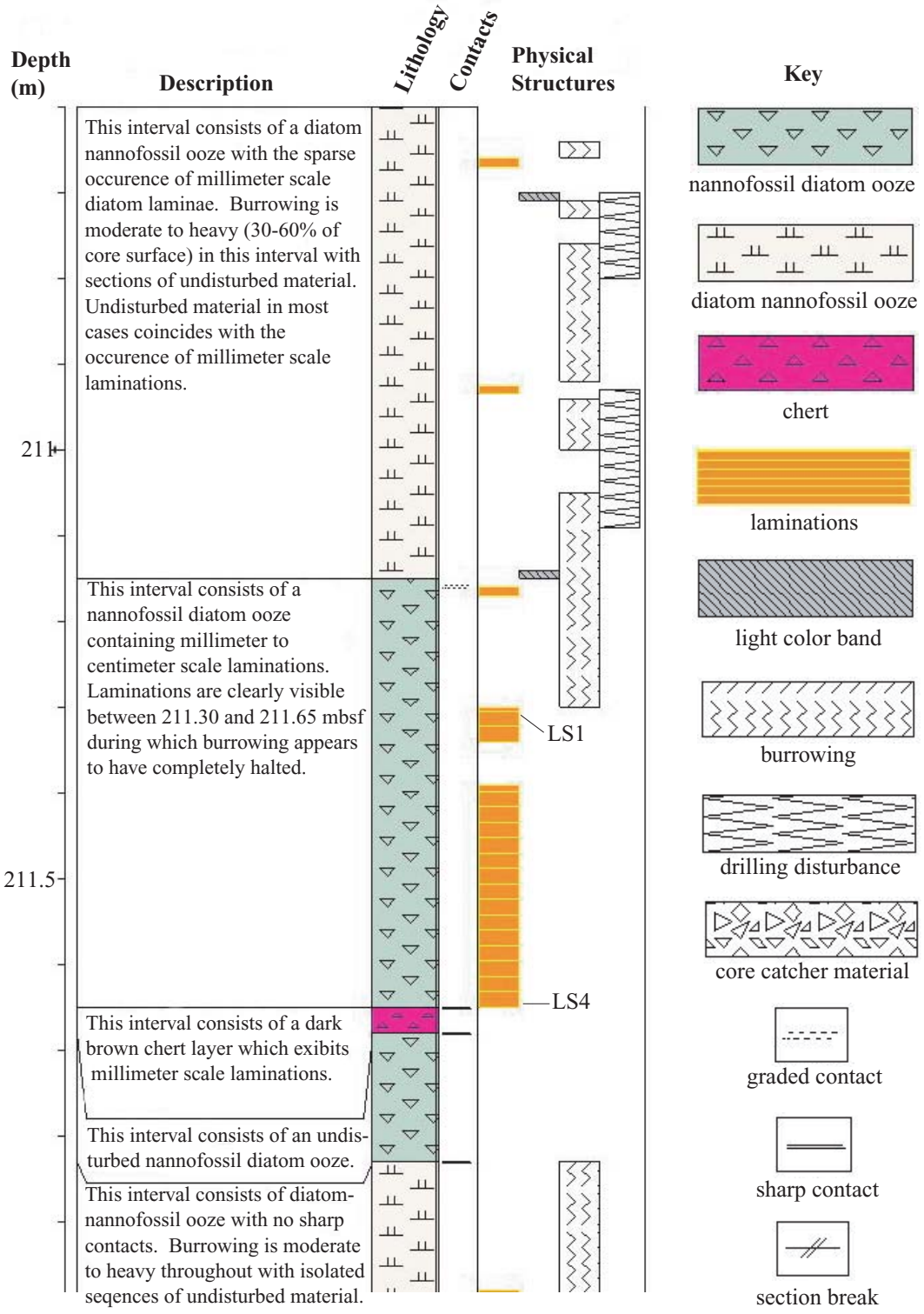

Figure 9 Description of 850B, 210.6 - 214.3 mbsf.

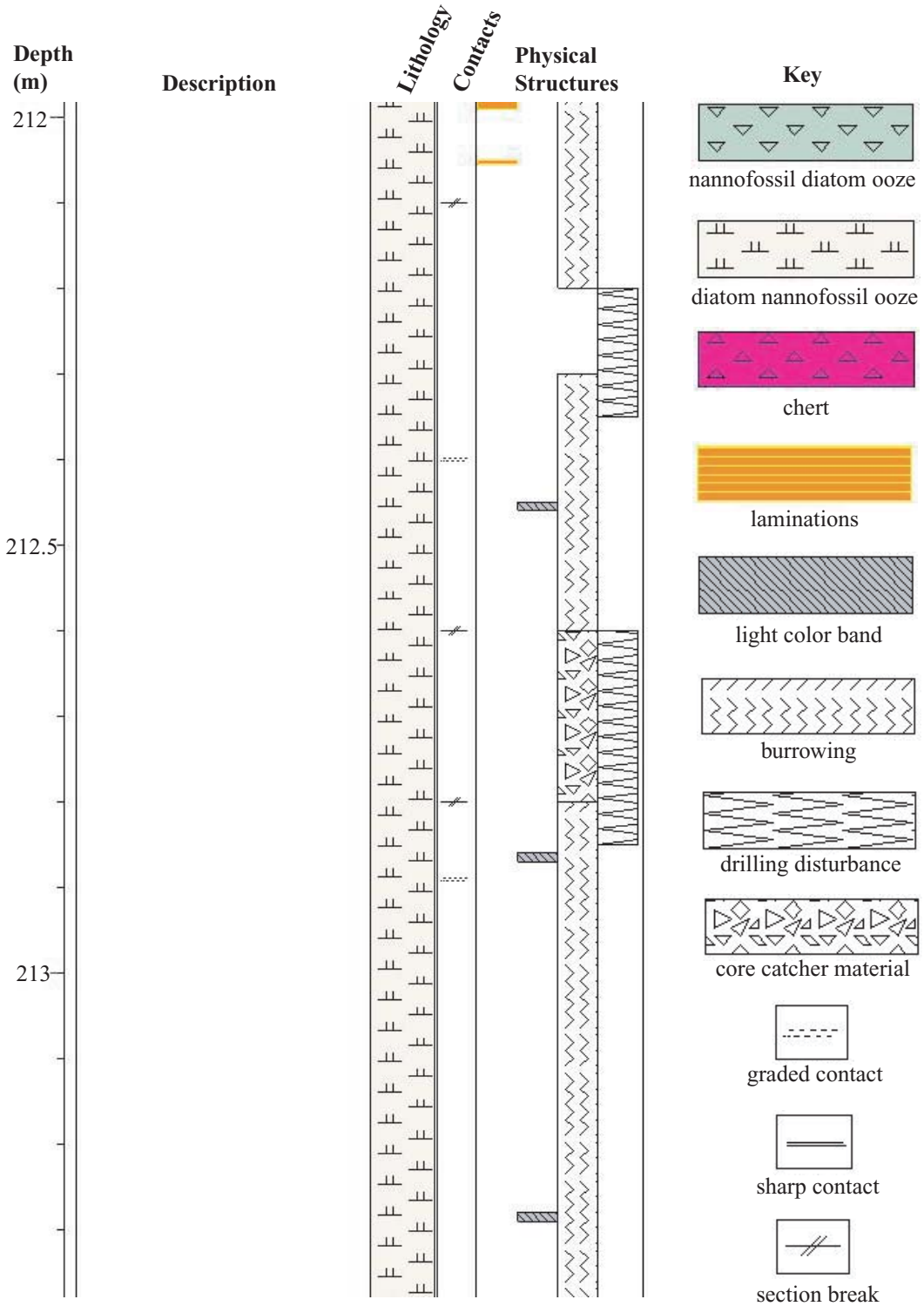

Figure 9 (continued).

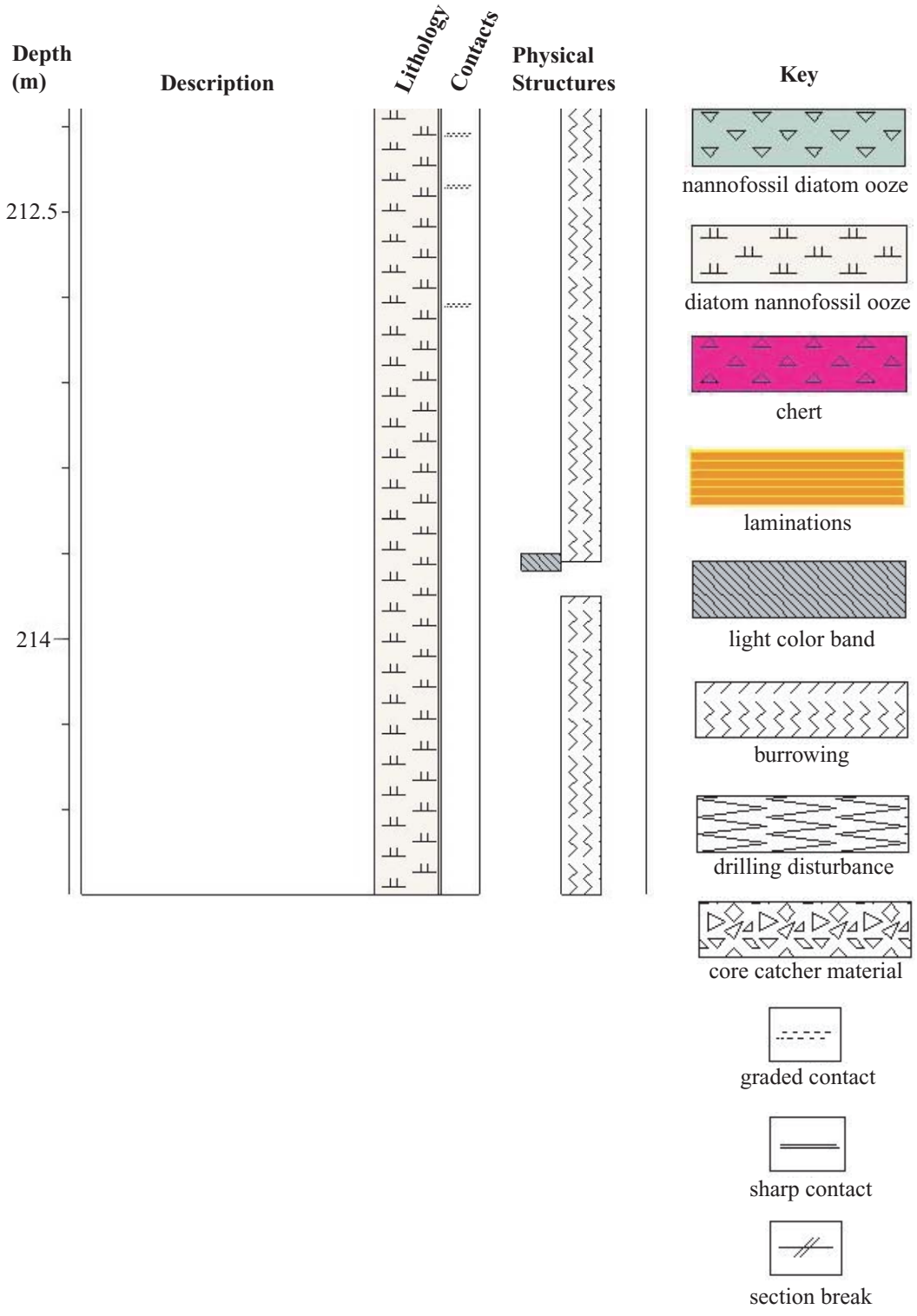

Figure 9 (continued).

(Figure 4) reveals the same layer. The chert layer found at Site 849 is much less disturbed and shows clear laminations. Sediments between 211.65 and 211.15 mbsf consist of a nannofossil diatom ooze. Close inspection confirmed the existence of a decimeter scale LDO packet beginning at approximately 211.65 mbsf and continuing to approximately 211.30 mbsf. The nannofossil diatom ooze was the same in color (5Y 7/2) as the material between 211.83 and 211.69 mbsf, however, individual millimeter to centimeter scale laminae packets appear as darker color bands (5Y 6/3). Burrowing was not apparent between 211.65 and 211.30 mbsf. Sediments between 211.15 and 210.60 mbsf consist of a diatom nannofossil ooze identical to that found below to 211.83 mbsf. Burrowing is moderate to heavy during most of this interval with undisturbed sections corresponding to millimeter to centimeter scale laminae packets at 210.93 mbsf and 210.67 mbsf.

X-rays were taken of the quarter round section from 211.65 to 211.31 mbsf in order to reveal millimeter to centimeter scale alterations within the larger packet (Figure 10). Centimeter scale packets were shown to occur between 211.65 and 211.42 mbsf at which point occurrence was reduced to sparse millimeter scale laminae at a frequency of every 2 to 3 cm. Visual observation of the core revealed that laminae occur at this frequency up to about 211.30 mbsf and potentially beyond.

Samples Processed/Counted

Samples were processed and counted at a frequency of every 5 cm between 215 and 214 mbsf. Following an initial survey of these counts, it was concluded that a

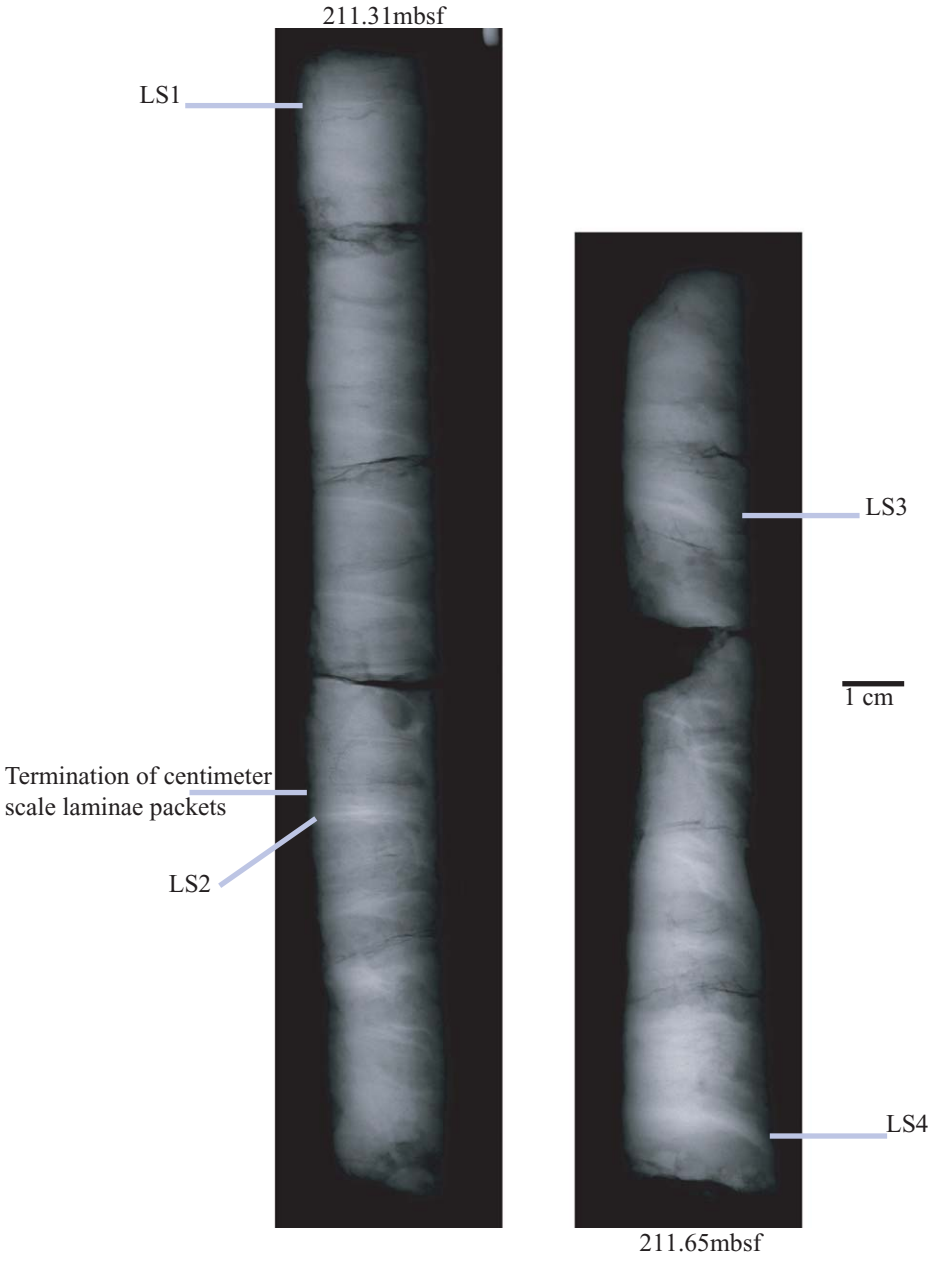

Figure 10 X-ray image of the quarter round section taken from the laminated sequence.

sampling interval of every 10 cm would be sufficient to characterize changes in abundance. Therefore, samples were processed and counted at 10 cm intervals between 214 and 211.69 mbsf. Samples were also counted at 10 cm intervals following the last observed laminae occurrence at approximately 211.30 mbsf up until 210.9 mbsf.

Due to the high frequency temporal variations of the LDO packet between 211.30 and 211.65 mbsf, the question of how to sample posed more of a problem. Four evenly spaced (as possible) laminae packets that exhibited a clear return on the x-ray were identified for sampling (LS4 – LS1) (Figure 10). However, in the process of sampling completely across each of these laminated sequences (encompassing intra-laminae sediments) at the millimeter level, 45 individual samples were collected. We, therefore, decided to concentrate on processing samples from LS4, the first laminae packet, and LS1, the last laminae packet observed in both the visual description and the x-ray. This was the most efficient means of characterizing overall change spanning the entire laminated sequence. A total of 11 samples taken at a millimeter to sub-millimeter frequency spanning the occurrence of the first laminated packet (LS4) at approximately 211.655 mbsf were processed and counted. A total of seven samples were processed and counted spanning the last observed laminae packet (LS1) at approximately 211.32 mbsf (Figure 10).

2. Absolute Abundance

Range charts for absolute abundance are provided in Appendix C. Figure 11 shows the total absolute abundance values for the entire data range including average values for LS4 (211.655 mbsf) and LS1 (211.320 mbsf). Figure 12 shows the total absolute abundance values for all samples processed from LS4 and LS1 (which were sampled at too high a frequency to be included in full in Figure 11 due to the large difference in scale). Values range from $5.0x10^7$ v/g at 214.95 mbsf to $4.8x10^8$ v/g at LS4-5 (approximately 211.655 mbsf). At final count, the observed assemblage consisted of 63 species and 13 groups. A detailed floral list is provided in Appendix B. Of these, 30 taxa and/or groups of taxa were chosen to be included in interpretive analysis based on the 95% confidence level for detection[79] (excluding *centric sp. indeterminate, Azpeitia sp. 1, and Stephanopyxis dimorpha* due to taxonomic uncertainty and very sparse occurrence). The absolute abundances of each of these species for the entire interval (including average values for LS4 and LS1) are provided in Appendix A, Figure 1. Absolute abundances for LS4 and LS1 are provided in Appendix A, Figure 3. The key taxa within the 95% confidence level are defined as those occurring in an absolute abundance of $1.0x10^7$ or greater. These taxa include *Nitzschia sp. indeterminate group*, *Nitzschia miocenica, Rhizosolenia spp., Synedra miocenica, Thalassionema hirosakiensis/schraderi group, Thalassionema nitzschioides, Thalassionema nitzschioides var. parva, Thalassionema group, Thalassiothrix longissima* , and *Thalassiosira praeconvexa* (Appendix A, Figures A-1 & A-3).

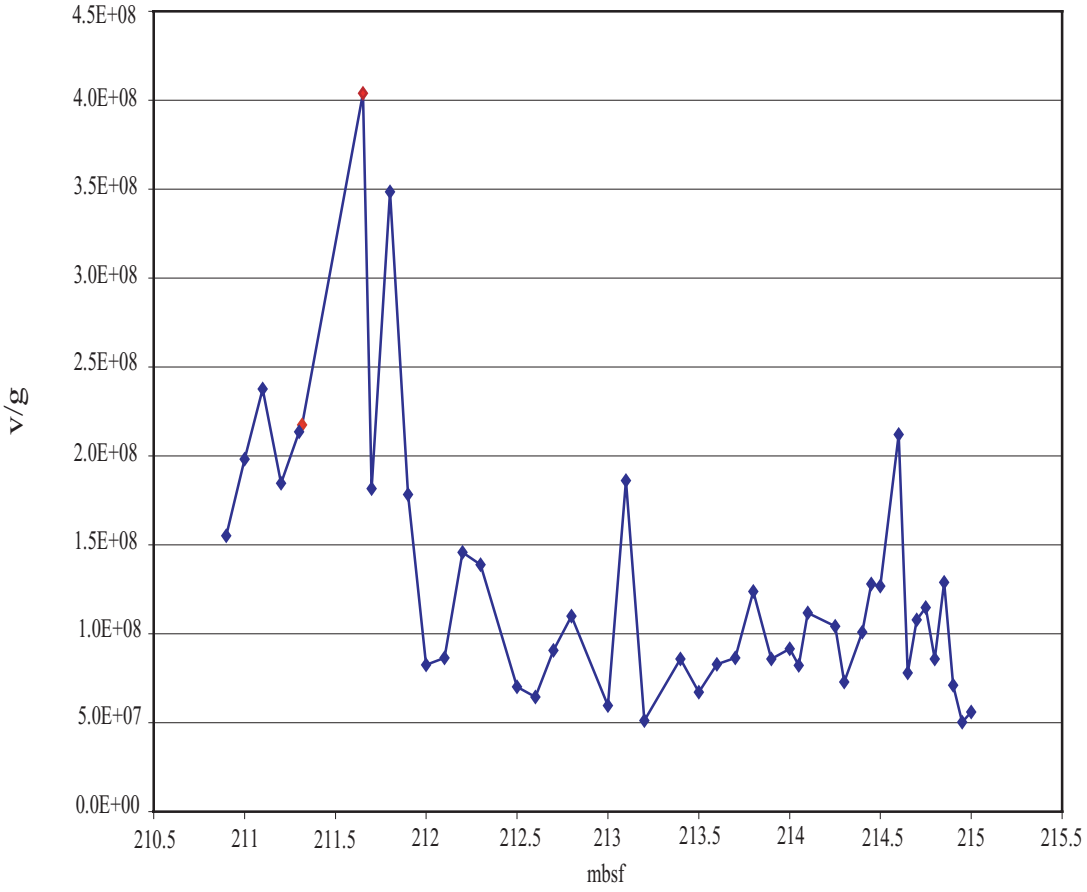

Figure 11 Total absolute abundance including laminae averages (red points).

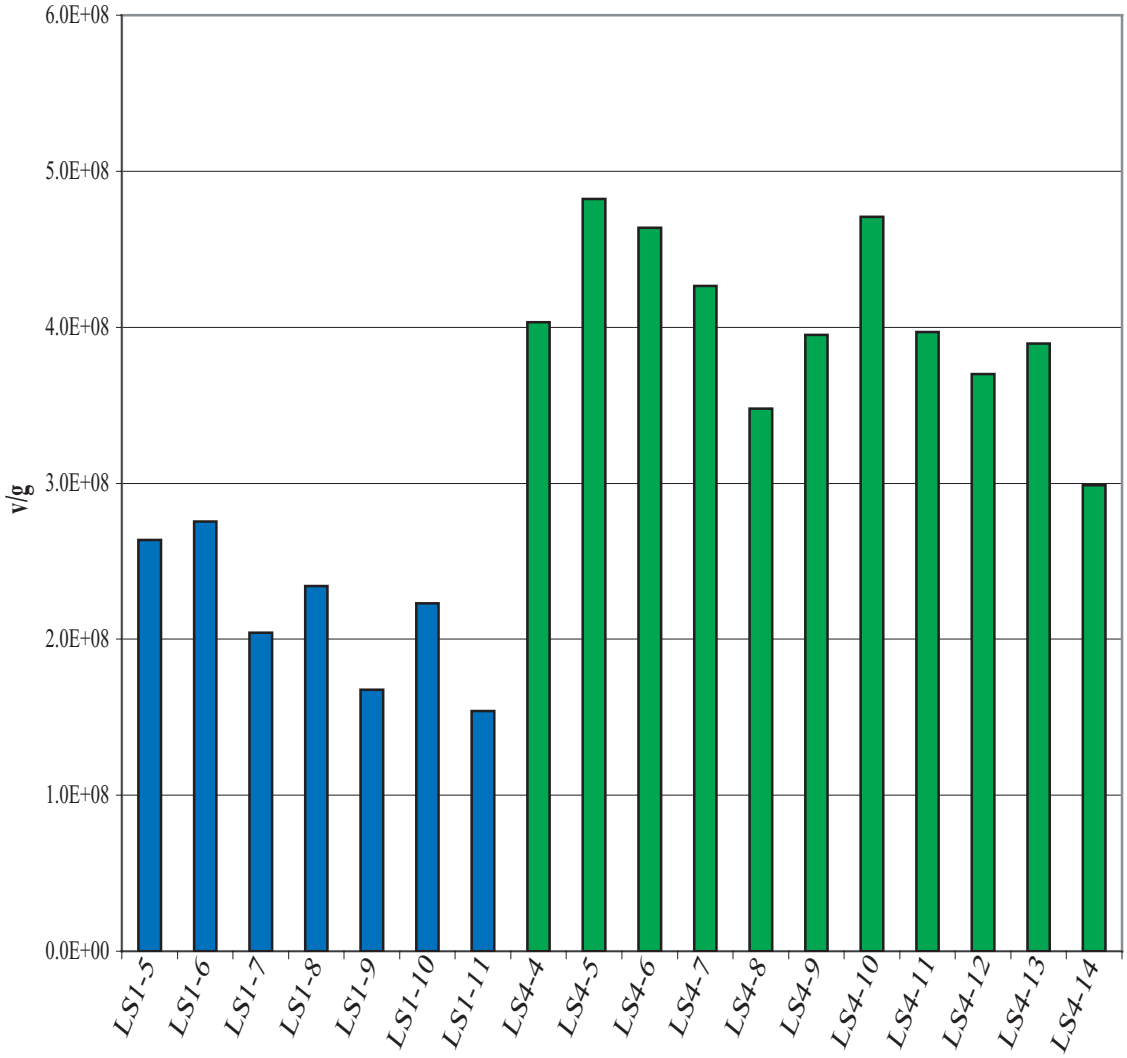

Figure 12 Total absolute abundance of LS4 (green) and LS1 (blue).

3. Relative Abundance

Range charts for relative abundance are provides in Appendix C. Individual graphs for the species that fall within the 95% confidence level are provided in Appendix A, Figures A-2(entire interval with LS4 and LS1 averages) and A-4 (LS4 and LS1).

4. Diversity

For the purpose of determining total diversity, counts were conducted to determine the total number of species present at each depth interval. This is considered here to be a first order approximation of species diversity. The results are presented in Figures 13 and 14. Counts were also conducted on just the taxa that fall within the 95% confidence level for detection. These results are presented in Figure 15 and 16. Excluded from these counts are *centric sp. indeterminate* and *Nitzschia sp. indeterminate group* due to their insignificance in terms of taxonomic distinction, and also *Azpeitia barroni* and *Stephanopyxis dimorpha* due to taxonomic uncertainty and very sparse occurrence.

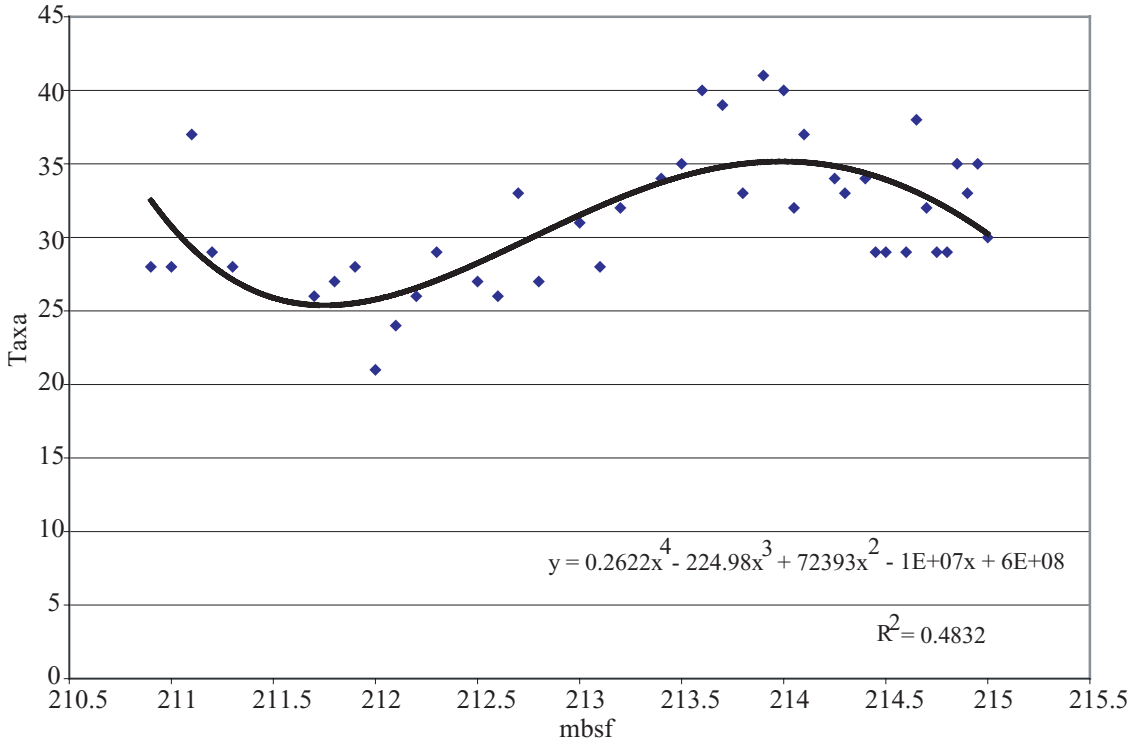

Figure 13 Total diversity excluding LS4 and LS1.

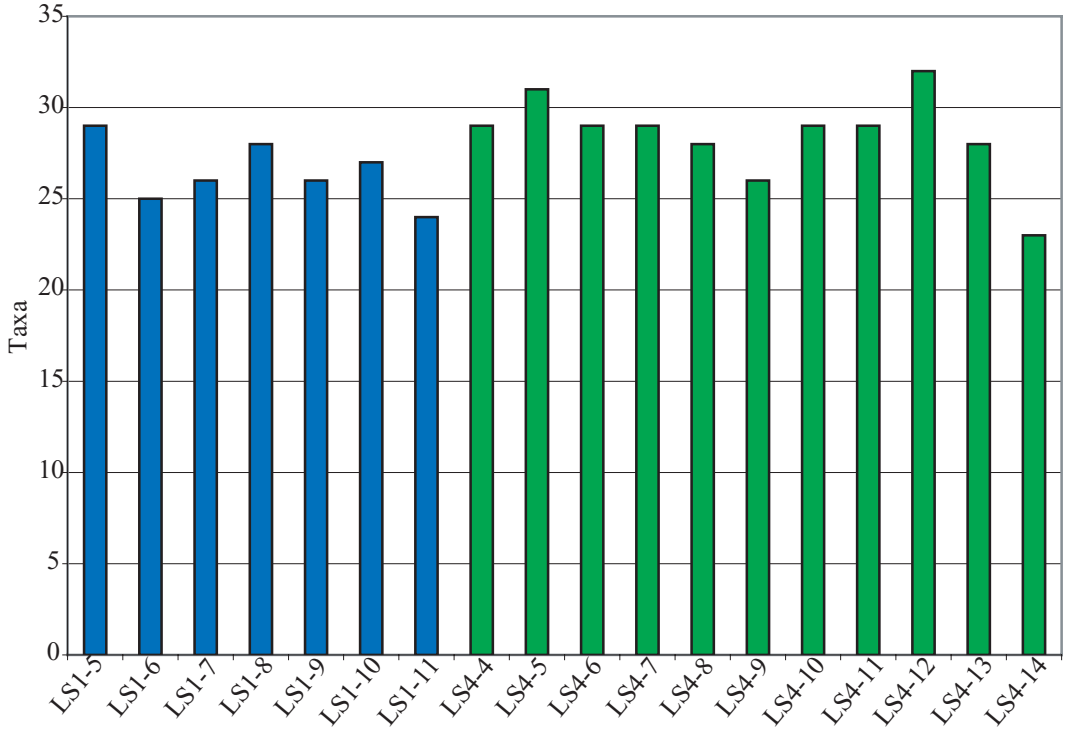

Figure 14 Total diversity for LS4 and LS1.

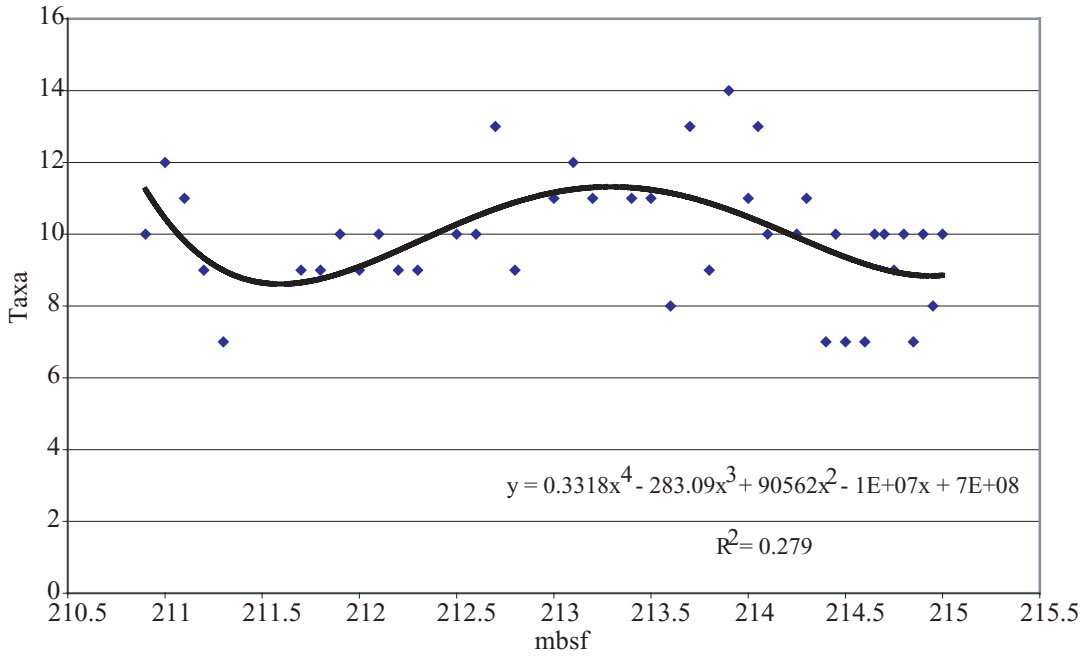

Figure 15 Diversity within the 95% confidence level for detection.

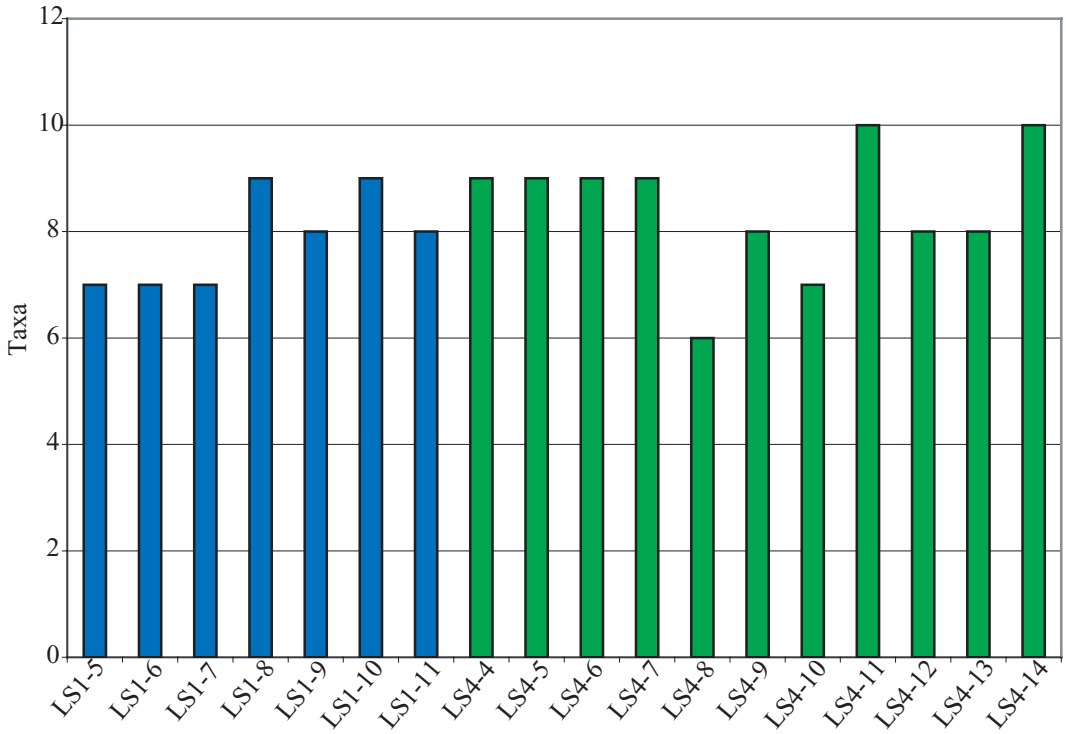

Figure 16 Diversity within the 95% confidence level for detection for LS4 and LS1.

DISCUSSION

1. Absolute abundance

215.0 – 210.9 mbsf

Between 210.9 and 215 mbsf three levels of total absolute abundance are apparent which indicate three modes of deposition (Figure 17). Mode one occurs between 215.0 and 212.0 mbsf where, with the exception of 214.6 mbsf and 213.1 mbsf, values range between $5.0x10^7$ v/g and $1.5x10^8$ v/g. Mode two occurs between 212.0 and 210.9 mbsf and is represented by values ranging between $1.5\ x10^8$ v/g and $3.0x10^8$ v/g. Mode three also occurs between 212.0 and 210.9 mbsf and is represented by values greater than $3.0x10^8$ v/g. Mode one represents pre-transitional deposition, mode two represents post-transitional deposition, and mode three is coincident with the deposition of LDO. LS4 at 211.655 falls within this final mode. LS1 at 211.32 mbsf, on the other hand, falls within mode two. The most likely reason that LS1 does not fall within the same mode is the failure to adequately sample across this millimeter scale laminae packet (Figure 10). LS4 was a centimeter scale laminae packet which allowed for at least partial isolation of the laminated sediments.

Cluster analysis based on a chi-square measure of between groups linkage was conducted (using ©SPSS) as a more objective means of characterizing depositional variation based on species absolute abundance (Figure 18). Each species was considered as a separate variable in relation to depth. Figure 18 shows each depth interval

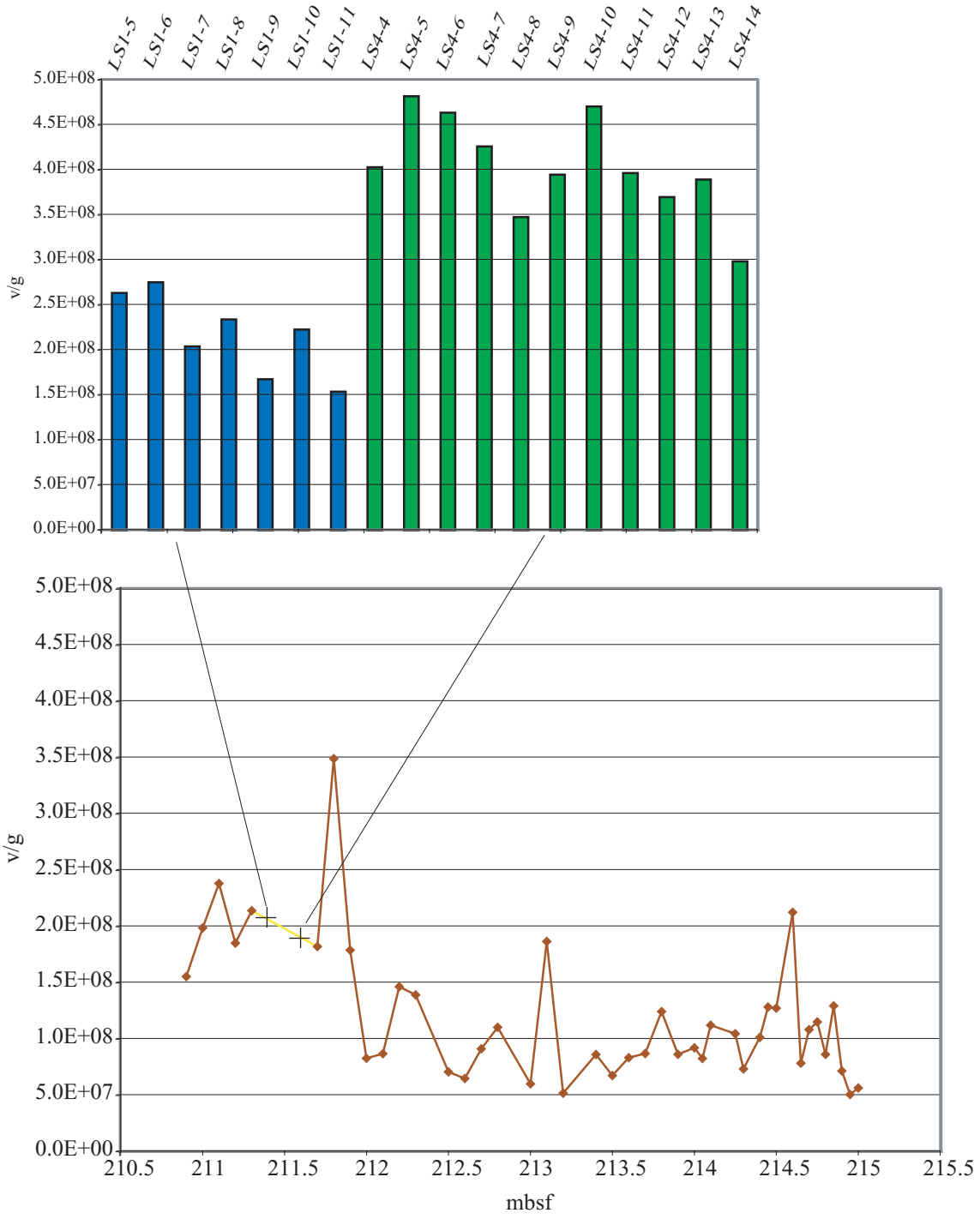

Figure 17 Absolute abundance for entire data set with a blow up of values from LS4 (green) and LS1 (blue) taken from the yellow portion of the line.

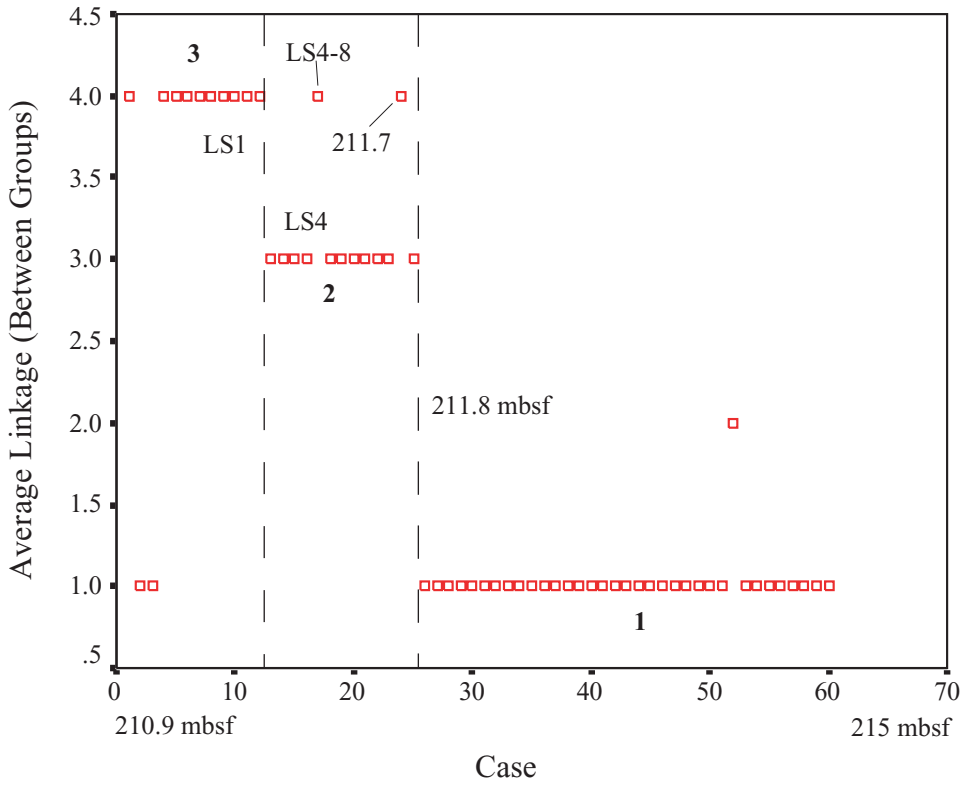

Figure 18 Absolute abundance cluster.

(clustered as a case due to variations in scale between laminae and non-laminae samples) consecutively plotted (from 215 – 211.8 mbsf) against average linkage between groups. The cluster analysis revealed three distinct groups. Cluster 1 includes nearly all samples between 215 and 211.9 mbsf. Cluster 2, separated from cluster 1 by two degrees of linkage, includes 211.8 mbsf and all samples from LS4 at 211.655 mbsf (with the exception of LS4-9). Cluster 3 includes 211.7 mbsf, LS4-9, all of LS1, and samples between 211.3 and 210.9 mbsf (with the exception of 211.1 mbsf and 211 mbsf which fall within cluster 1). Cluster 3, however, is only separated from cluster 2 by one degree of linkage. This analysis is in almost perfect agreement with the three depositional modes described above. There are three clusters with a more pronounced transition between clusters 1 and 2 than clusters 2 and 3.

Observation of the individual abundance of key species provides insight into what factors forced these three modes. Most apparent is the change in absolute abundance of *Thalassionema nitzschioides* (Appendix A, Figure A-1F), which due to its dominance of the assemblage, mirrors the change in total absolute abundance and displays clearly the three modes discussed above. Also *Thalassiothrix longissima* (Appendix A, Figure A-1G), and to a lesser degree *Rhizosolenia spp.* (Appendix A, Figure A-1D), display a similar trend in absolute abundance with a stepwise increase at approximately 212.0 mbsf.

LS4 and LS1

Clearly the driving force behind the formation of LS4 was the increase in the absolute abundance of *Thalassionema nitzschioides* to values as great as $3.3x10^8$ v/g (an approximate shift of $1.5x10^8$ v/g above post-transitional background) (Appendix A, Figure A-3F). Also, *Nitzschia miocenica* with an average increase of approximately $2.0x10^7$ v/g (Appendix A, Figure A-3C) and *Thalassiosira praeconvexa* with an average increase of approximately $1.0x10^7$ v/g (Appendix A, Figure A-3G) 3 occur in levels significantly greater than post-transitional (211.8 mbsf) background. No clearly definable trends occur within LS4 making it difficult to make assessments about the change in the assemblage spanning the actual laminae packet. However, this is most likely the result of time averaging due to the sampling constraints of approximately 1 millimeter.

LS1 appears at background levels in terms of individual species and total absolute abundance. The one exception is *Thalassionema group* which occurred in an abundance of $2.3x10^7$ v/g during LS1 as opposed to post-transitional (211.8 mbsf) background levels averaging around $5.0x10^6$ v/g (Appendix A, Figures A-2F and A-4F). As discussed above, inaccuracies in the sampling method most likely resulted in the failure to isolate the millimeter scale laminae packet.

2. Relative Abundance

215.0 – 210.9 mbsf

The relative abundance of key species reveals the near complete dominance of the assemblage by *Thalassionema nitzschioides* (Figure 19). Values range from 26.4 percent at 214.7 mbsf to 74.2 percent at 211.8 mbsf. The only other species to achieve dominance over *Thalassionema nitzschioides* is *Nitzschia miocenica* with a relative abundance of 36.5 percent at 214.7 mbsf (Figure 19).

As with absolute abundance, cluster analysis was conducted using a chi-square measure of between groups linkage. The results of this analysis revealed four distinct clusters (Figure 20). Cluster 1 is composed of all samples from between 215.0 and 214.85 mbsf. Cluster 2 is separated from cluster 1 by one degree of between groups linkage, and includes all samples from between 214.8 and 212.8 mbsf. Cluster 3 is separated from cluster 2 by one degree of between groups linkage and includes all samples between 212.7 and 210.9 mbsf with the exception of 212.6 mbsf, 212.5 mbsf, and 212.0 mbsf. These three later samples fall into cluster 4, and are separated from cluster 3 by one degree of between groups linkage. Individual species abundance again provides insights into the controlling mechanisms behind these groupings. Cluster 1 is only composed of the lowest four samples. These four points are separated from cluster 2 dominantly because of the peak in abundance of *Thalassionema nitzschioides var. parva* (Appendix A, Figure A-2F) between 215.0 and 214.85 mbsf. This peak in *Thalassionema nitzschioides var. parva* is unconstrained due to the lower sampling limit,

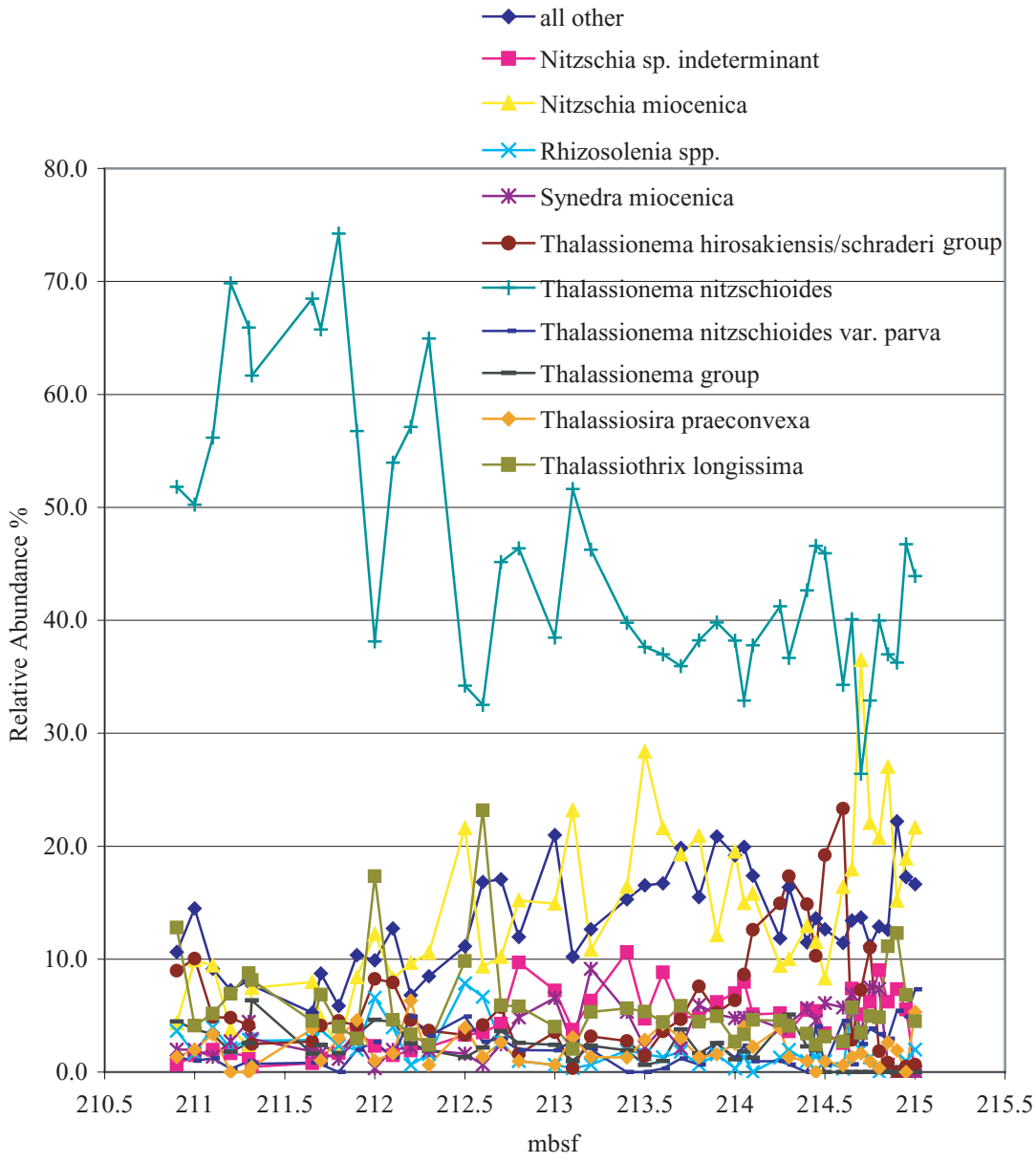

Figure 19 Relative abundance of key species against all other taxa including laminae averages.

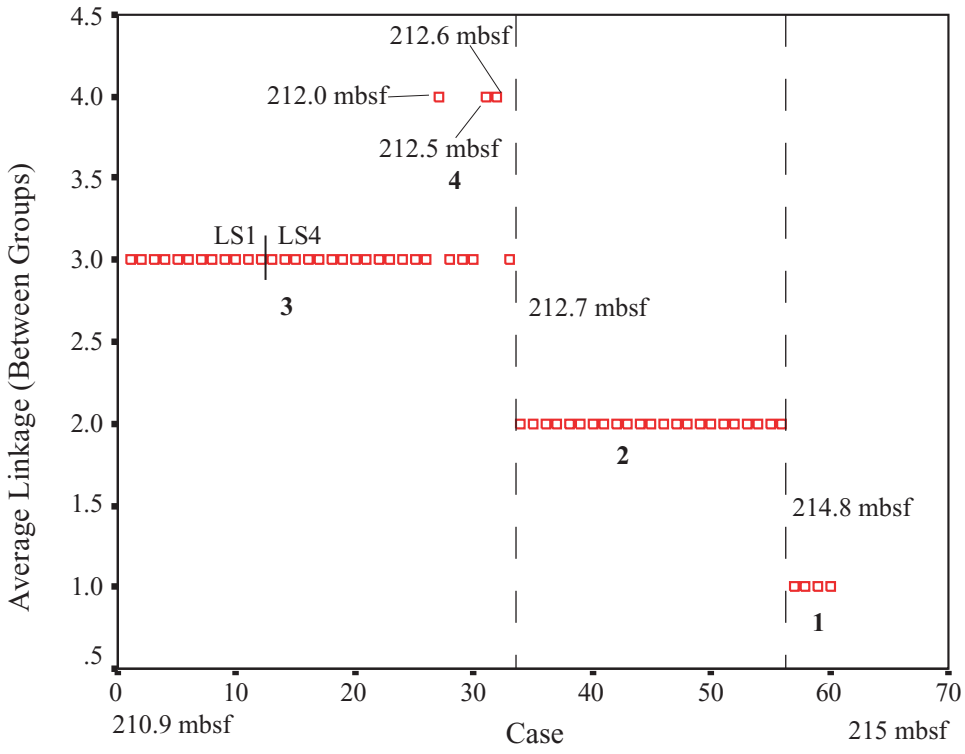

Figure 20 Relative abundance cluster.

and, coincidentally, the first observed occurrence of this species at approximately 215 mbsf. Therefore, its use as a definitive group is very questionable, and is henceforth not considered relevant. Clusters 2 and 3, and specifically the transition between the two, represent a transition in the overall balance of the assemblage. A closer look at individual species abundance reveals a stepwise increase in the relative abundance of *Thalassionema nitzschioides* (Appendix A, Figure A-2F) from values averaging around 40 percent to values averaging around 60 percent at approximately 212.3 mbsf. Associated with this, *Nitzschia sp. indeterminate group* (Appendix A, Figure A-2B), *Rhizosolenia barboi group* (Appendix A, Figure A-2D), and *Synedra miocenica* (Appendix A, Figure A-2E) each undergo stepwise decrease in relative abundance between 212.6 and 212.3 mbsf of approximately 4 percent. The gradual decrease in relative abundance of *Nitzschia miocenica* (Appendix A, Figure A-2C) between 215.0 and 210.9 mbsf makes it difficult to determine if it contributed to this transition. Cluster 4 represents a combination of the peaks in relative abundance of *Actinoptychus senarius* (1.3 percent at 212.6 mbsf) (Appendix A, Figure A-2A), *Rhizosolenia spp.* (6.7 percent at 212.6 mbsf, 7.9 percent at 212.5 mbsf, and 6.6 percent at 212.0 mbsf) (Appendix A, Figure A-2D), and *Thalassiothrix longissima* (23.2 percent at 212.6 mbsf and 17.3 percent at 212.0 mbsf) (Appendix A, Figure A-2G).

LS4 and LS1

In terms of relative abundance, there were no significant changes in relation to post-transitional (212.7 mbsf) background levels. Relative abundances remained

essentially constant through both LS1 and LS4. The one exception is the increase in relative abundance of *Thalassionema group* from averages around 3 percent to greater than 8 percent in LS1. There are no other clearly discernible trends in individual species abundance from LS4 and LS1.

3. Diversity

There appears to be a drop in species diversity, and 95% confidence level species diversity around and during LDO formation (Figures 13-16). However, the drop in species diversity may not be real due to the increase in absolute abundance of *Thalassionema nitzschioides* and other key species. The majority of rare species occur sporadically throughout the entire interval, and could have simply been diluted during the periods of LDO formation.

4. Environmental Interpretation

Considered as a whole, these results provide considerable insight into the ecological changes that occurred during the transition at 6.6 Ma. The abundance of diatom frustules of the sea floor is influenced dominantly by the number of diatom cells produced in the euphotic zone, and the dissolution of diatom frustules within the water column and on the sea floor. The total absolute abundance of diatom frustules determined for samples in this study are considered as a proxy indicator for productivity

in the surface waters with full knowledge of the limitations resulting from frustule dissolution.

Total absolute abundance (Figure 17) reveals three levels of productivity representing pre-transition, LDO formation, and post-transition. Cluster analysis of the absolute abundance data makes almost perfect agreement revealing three distinct groups corresponding to the levels observed in Figure 17. Both lines of evidence point to three distinct modes in biogenic sedimentation with a major transition occurring at approximately 211.8 mbsf. However, cluster analysis of relative abundance data reveals an overall transition in species relative abundances at 212.7 mbsf, approximately 1 meter below the transition in absolute abundance, indicating a shift in assemblage proportionality well before the increase in frustule deposition. The lag between shifts in relative and absolute abundance indicates a period of ecologic adjustment. Based on the precursory estimate of a linear sedimentation rate of 4.43 $cmky^{-1}$, this transitional period lasted roughly 20 ky. Due to the uncertainty of sedimentation rates, and the sparse number of age control points for the period of interest, this duration remains an estimate. Regardless of the estimated duration of the transition period, these results imply a gradual change in paleoceanographic parameters preceding a major increase in the number of diatom frustules deposited on the sea floor. After the depositional transition occurred at 211.8 mbsf, the preservation of LDO in the sedimentary sequence records an almost instantaneous change in deposition resulting from relatively sporadic paleoceanographic change.

Individual species abundances provide some insight into environmental changes during this transition. The most outstanding aspect of individual species abundance data is the persistent, and at some times, almost complete dominance of the assemblage by *Thalassionema nitzschioides* (Appendix A, Figures A-1F and A-3F). The ecological preference of this species towards areas of strong to marginal coastal upwelling, and its relative resistance to dissolution are well documented[64,66,80,81]. Kobayashi and Takahashi (2002)[82] have also associated this species with weak upwelling in the central and western pacific during times of increased nutrient availability (1999 La Nina event). Based on this information, the increase in the absolute abundance of this species at 212.0 mbsf, preceded by an increase in relative abundance at approximately 212.3 mbsf implies an overall increase in nutrient availability at this time. The only species to occur in higher abundance than *Thalassionema nitzschioides* is *Nitzschia miocenica* (Figure 19). Though this species is extinct, modern upwelling systems in the equatorial pacific are characterized by somewhat analogous small *Nitzschia* and *Pseudonitzschia* species[31,82].

Overall increase in nutrient availability is also supported by the increase in absolute abundance of *Rhizosolenia spp.* (Appendix A, Figures A-1D and A-3D) and *Thalassiothrix longissima* (Appendix A, Figures A-1G and A-3G). These species have been associated with high productivity in pelagic environments[18,64]. Both show a stepwise to sporadic increase, beginning at approximately 212.0 mbsf, very similar to that seen in *Thalassionema nitzschioides* (Appendix A, Figures A-1F and A-3F). Also interesting, is the acme in abundance of *Actinoptychus senarius* (Appendix A, Figures A-1A) between 213.0 mbsf and 212.3 mbsf. This is a neritic species which has been

associated with off-shore transport due to increased trade wind strength in the EEP[64]. The presence of LDO packets, specifically those such as LS4, indicate the sporadic nature of nutrient input at a centennial, to potentially even decadal scale following the overall increase in nutrient availability. This sporadic nature is supported by the lack of a clear species succession, and the drop in overall species diversity at and immediately preceding LDO formation. On example of a process influencing nutrient availability at a decadal scale is the El Nino/La Nina cycle, which greatly effects nutrient availability in the EEP today.

Based on this information, two possible explanations can be made concerning the depositional transition a 6.6 Ma in the EEP: (1) an upwelling cell was initiated at 110º W, or (2) there was an increase in the amount of nutrients an upwelling cell at, or adjacent to 110º W was bringing into the euphotic zone. The initiation or strengthening of an upwelling cell could have been the result of a strengthening of the trade winds in the EEP. A strengthening of the trade winds could have been associated with the commencement of the East Asian Paleomonsoons at approximately 7.2 Ma. Nutrients could have also been made more available via upwelling due to a shoaling of the thermocline in the EEP. A shoaling of the thermocline could have also been associated with an increase in trade wind strength, and/or the interruption of equatorial flow below 150 m as is associated with the shoaling of the Ismuth of Panama.

CONCLUSIONS

1. Three distinct modes of sedimentary deposition occurred representing a pre-transition lithology, a post-transition lithology, and LDO formation.
2. The overall transition in absolute abundance was preceeded by approximately 20 ky by a shift in relative abundance and overall assemblage proportionality. This indicates a more gradual change in oceanographic parameters prior to the shift in depositional mode.
3. Post-transitional LDO formation indicates sporadic deposition of diatomaceous material following the transition at 6.6 Ma.
4. A significant increase in the abundance of *Thalassionema nitzschioides* was the major contributor to the formation of LDO and post-transitional sediments. Its known ecological preferences indicate an overall increase in nutrient availability followed by sporadic changes in nutrient availability. This could be associated with the establishment or increase in the strength of an upwelling cell at 110º W in the EEP and/or the increase in nutrient availability via upwelling as a result of the shoaling of the thermocline.

REFERENCES

1. Chavez, F. P. & Barber, R. T. An estimate of new production in the Equatorial Pacific. *Deep-Sea Research* **34**, 1229-1243 (1987).

2. Takahashi, T. *et al*. Global air-sea flux of CO_2: an estimate based on measurements of sea-air pCO_2 difference. *Proceedings of the National Academy of Science* **94**, 8292-8299 (1997).

3. Maier-Reimer, E., Mikolajewicz, U. & Crowley, T. Ocean general circulation model sensitivity experiment with an open Central American Isthmus. *Paleoceanography* **5**, 349-366 (1990).

4. Lyle, M., Dadey, K. A. & Farrell, J. W. The Late Miocene (11-8 MA) Eastern Pacific carbonate crash: evidence for reorganization of deep-water circulation by the closure of the Panama Gateway. *Proceedings of the Ocean Drilling Program, Scientific Results* **138**, 821-838 (1995).

5. Farrell, J. W. *et al*. Late Neogene sedimentation patterns in the Eastern Equatorial Pacific Ocean. *Proceedings of the Ocean Drilling Program, Scientific Results* **138**, 717-755 (1995).

6. Zhisheng, A. The history and variability of the East Asian paleomonsoon climate. *Quaternary Science Reviews* **19**, 171-187 (2000).

7. Theyer, F., Mayer, L. A., Barron, J. A. & Thomas, E. The equatorial Pacific high-productivity belt: elements for a synthesis of Deep Sea Drilling Project Leg 85 results. *Initial Reports of the Deep Sea Drilling Project, Leg 85* **85**, 971-985 (1985).

8. Leinen, M. Biogenic silica accumulation in the central equatorial Pacific and its implications for Cenozoic paleoceanography. *Geological Society of America Bulletin* **90**, 1310-1376 (1979).

9. Kemp, A., Baldauf, J. G. & Pearce, R. Origins and paleoceanographic significance of laminated diatom ooze from the Eastern Equatorial Pacific Ocean. *Proceedings of the Ocean Drilling Program, Scientific Results* **138**, 641-645 (1995).

10. Pearce, R. B., Kemp, A. E. S., Baldauf, J. G. & King, S. C. High-resolution sedimentology and micropaleontology of laminated diatomaceous sediments

from the eastern equatorial Pacific Ocean. *Proceedings of the Ocean Drilling Program, Scientific Results* **138**, 647-663 (1995).

11. Cox, A. & Engebretson, D. Change in motion of the Pacific plate at 5 Myr BP. *Nature* **313**, 472-474 (1985).

12. Sykes, L. R., McCann, W. R. & Kafka, A. L. Motion of the Caribbean Plate during last 7 million years and implications for earlier Cenozoic movements. *Journal of Geophysical Research* **87**, 10,656-10,676 (1982).

13. Marshall, L. G., Webb, S. D., Sepkoski, J. J. & Raup, D. M. Mammalian evolution and the great American interchange. *Science* **215**, 1351-1357 (1982).

14. Keigwin, L. Isotopic paleoceanography of the Caribbean and East Pacific: role of Panama uplift in late Neogene time. *Science* **217**, 350-353 (1982).

15. Pond, S. & Pickard, G. L. *Introductory Dynamical Oceanography* (Butterworth-Heinemann, Oxford, 2000).

16. Wyrtki, K. & Kilonsky, B. Mean water and current structure during the Hawaii-to-Tahiti shuttle experiment. *Journal of Physical Oceanography* **14**, 242-254 (1984).

17. Pickard, G. L. & Emery, W. J. *Descriptive Physical Oceanography: an Introduction* (Butterworth-Heinemann, Oxford, 2000).

18. Yoder, J. A., Ackleson, S. G., Barber, R. T., Flament, P. & Balch, W. M. A line in the sea. *Nature* **371**, 689-692 (1994).

19. Schlitzer, R. Ocean Data View. *http:/www.awi-bremerhaven.de/GEO/ODV* (2000).

20. Fiedler, P. C., Philbrick, V. & Chavez, F. P. Oceanic upwelling and productivity in the Eastern Tropical Pacific. *Limnology and Oceanography* **36**, 1834-1850 (1991).

21. Landry, M. R. *et al*. Biological response to iron fertilization in the eastern equatorial Pacific (IronEx. II). III. Dynamics of phytoplankton growth and microzooplankton grazing. *Marine Ecology Progress Series* **201**, 57-72 (2000).

22. Lindley, S. T. & Barber, R. T. Phytoplankton response to natural and experimental iron addition. *Deep-Sea Research II* **45**, 1135-1150 (1998).

23. Martin, J. H. *et al*. Testing the iron hypothesis in ecosystems of the equatorial Pacific Ocean. *Nature* **371**, 123-129 (1994).

24. Raven, J. A. The iron and molybdenum use efficiencies of plant growth with different energy, carbon and nitrogen sources. *New Phytology* **109**, 279-287 (1988).

25. Hutchins, D. A. & Bruland, K. W. Iron-limited diatom growth and Si:N uptake ratios in a coastal upwelling regime. *Nature* **393**, 561-564 (1998).

26. Takeda, S. Influence of iron availability on nutirient consumption ratio of diatoms in oceanic waters. *Nature* **393**, 774-777 (1998).

27. Chavez, F. P., Buck, K. R., Service, S. K., Newton, J. & Barber, R. T. Phytoplankton variability in the central and eastern tropical Pacific. *Deep-Sea Research II* **43**, 835-870 (1996).

28. Jimenez, R. in *Coastal upwelling. Coastal Estuarine Science* (ed. Richards, F. A.) 327-338 (AGU, 1981).

29. Sancetta, C., Villareal, T. & Falkowski, P. Massive fluxes of rhizosolenid diatoms: a common occurence? *Limnology and Oceanography* **36**, 1452-1457 (1991).

30. Hasle, G. R. A quantitative study of phytoplankton from the equatorial Pacific. *Deep-Sea Research* **6**, 38-59 (1959).

31. Chavez, F. P., Buck, K. R. & Barber, R. T. Phytoplankton taxa in relation to primary production in the Equatorial Pacific. *Deep-Sea Research* **37**, 1733-1752 (1990).

32. Burckle, L. H. Late Cenozoic planktonic diatoms from the eastern equatorial Pacific. *Nova Hedwigia Beih.* **39**, 217-246 (1972).

33. Burckle, L. H. Pliocene and Pleistocene datum levels from the equatorial Pacific. *Quaternary Research* **7**, 330-340 (1977).

34. Burckle, L. H. & Trainer, J. Middle Miocene and Late Pliocene datum levels for the central Pacific. *Micropaleontology* **25**, 281-293 (1979).

35. Barron, J. A. Late Eocene to Holocene diatom biostratigrapy of the Equatorial Pacific Ocean, Deep Sea Drilling Project Leg 85. *Initial Reports of the Deep Sea Drilling Project* **85**, 413-456 (1985).

36. Baldauf, J. G. & Iwai, M. Neogene diatom biostratigraphy for the Eastern Equatorial Pacific Ocean, Leg 138. *Proceedings of the Ocean Drilling Program, Scientific Results* **138**, 105-128 (1995).

37. Barron, J. A. in *Plankton Stratigraphy* (eds. Bolli, H. M., Saunders, J. B. & Perch-Nielsen, K.) 1006 (Cambridge University Press, Cambridge, 1985).

38. Schrader, J. J. Cenozoic diatoms from the Northeast Pacific. *Initial Reports of the Deep Sea Drilling Project* **18**, 673-797 (1973).

39. Schrader, H. J. Cenozoic marine planktonic diatom stratigraphy of the tropical Indial Ocean. *Initial Reports of the Deep Sea Drilling Project* **24**, 887-967 (1974).

40. Sancetta, C. Biostratigraphic and paleoceanographic events in the eastern equatorial Pacific: results of Deep Sea Drilling Project Leg 69. *Initial Reports of the Deep Sea Drilling Project Leg 69* **69**, 311-320 (1979).

41. Sancetta, C. Diatom biostratigraphy and paleoceanography, Deep Sea Drilling Project Leg 68. *Initial Reports of the Deep Sea Drilling Porject Leg 68* **68**, 301-309 (1979).

42. Baldauf, J. G. A high resolution Late Miocene-Pliocene diatom biostratigraphy for the Eastern Equatorial Pacific. *Initial Reports of the Deep Sea Drilling Project* **85**, 457-475 (1985).

43. Barron, J. A. Diatom paleoceanography and paleoclimatology of the central and eastern equatorial Pacific between 18 and 6.2 Ma. *Initial Reports of the Deep Sea Drilling Project* **85**, 935-945 (1985).

44. Barron, J. A. & Baldauf, J. G. in *Productivity of the Ocean: Present and Past* (eds. Berger, W. H., Smetacek, V. S. & Wefer, G.) 341-354 (John Wiley & Sons Limited, New York, 1989).

45. King, S. C., Murray, J. W. & Kemp, A. E. S. Paleoenvironments of deposition of Neogene laminated diatom mat depostits from the Eastern Equatorial Pacific from studies of benthic foraminifera. *Marine Micropaleontology* **35**, 161-177 (1998).

46. Duque-Caro, H. Neogene stratigraphy, paleoceanography and paleobiogeography in northwest South America and the evolution of the Panama Seaway. *Paleogeography, Paleoclimatology, Paleoecology* **77**, 203-234 (1990).

47. Hagelberg, T. K., Pisias, N. G., Shackleton, N. J., Mix, A. C. & Harris, S. Refinement of a high-resolution, continuous sedimentary section for studying equatorial Pacific Ocean paleoceanography, Leg 138. *Proceedings of the Ocean Drilling Program, Scientific Results* **138**, 31-46 (1995).

48. Heinze, C. & Crowley, T. J. Sedimentary response to ocean gateway circulation changes. *Paleoceanography* **12**, 742-754 (1997).

49. Kemp, A. E. S. & Baldauf, J. G. Vast Neogene laminated diatom mat deposits from the Eastern Equatorial Pacific Ocean. *Nature* **362**, 141-144 (1993).

50. Pisias, N. G. & Moore, T., Jr. Radiolarian response to oceanographic changes in the eastern equatorial pacific at 2.3 and 4.8 MA: relationship between changing carbonate deposition and surface oceanography. *Proceedings of the Ocean Drilling Program, Scientific Results* **138**, 461-478 (1995).

51. Shackleton, N. J. *et al*. Biostratigraphic summary for Leg 138. *Proceedings of the Ocean Drilling Program, Scientific Results* **138**, 517-536 (1995).

52. Shackleton, N. J. & Hall, M. A. Stable isotope records in bulk sediments (Leg 138). *Proceedings of the Ocean Drilling Program, Scientific Results* **138**, 797-805 (1995).

53. Schneider, D. A. Paleomagnetism of some Leg 138 sediments: detailing Miocene magnetostratigraphy. *Proceedings of the Ocean Drilling Program, Scientific Results* **138**, 59-72 (1995).

54. Moore, T. C., Jr. Radiolarian stratigraphy, Leg 138. *Proceedings of the Ocean Drilling Program, Scientific Results* **138**, 191-232 (1995).

55. Raffi, I. & Flores, J.-A. Pleistocene through Miocene calcareous nannofossils from the eastern equatorial Pacific Ocean (Leg 138). *Proceedings of the Ocean Drilling Program, Scientific Results* **138**, 233-286 (1995).

56. van Andel, T. H., Heath, G. R. & T. C. Moore, J. Cenozoic history and paleoceanography of the central equatorial Pacific Ocean: a regional synthesis of Deep Sea Drilling Project data. *Memoirs - Geological Society of America* **143**, 143 (1975).

57. Vincent, E. Neogene carbonate stratigraphy of Hess Rise (central North Pacific) and paleoceanographic implications. *Initial Reports of the Deep Sea Drilling Project* **85**, 571-606 (1981).

58. Hayes, D. E. *et al*. Introduction. *Initial Reports of the Deep Sea Drilling Project* **28**, 5-18 (1973).

59. Berger, W. H., Lange, C. B. & Perez, M. E. The early Matuyama Diatom Maximum off SW Africa: a conceptual model. *Marine Geology* **180**, 105-116 (2002).

60. Berger, W. H. & Wefer, G. On the reconstruction of upwelling history: Namibia upwelling in context. *Marine Geology* **180**, 3-28 (2002).

61. Boden, P. A laminated sediment sequence from the northern North Atlantic Ocean and its climatic record. *Geology* **24**, 507-510 (1996).

62. Chang, A. S., Grimm, K. A. & White, L. D. Diatomaceous sediments from the Miocene Monterey Formation, California: a laminae-scale investigation of biological, ecological, and sedimentary processes. *Palaios* **13**, 439-458 (1998).

63. Diester-Haass, L., Meyers, P. A. & Vidal, L. The late Miocene onset of high productivity in the Benguela Current upwelling system as part of a global pattern. *Marine Geology* **180**, 87-103 (2002).

64. Kennington, K., Haslett, S. K. & Funnell, B. M. Offshore transport of nertic diatoms as indicators of surface current and trade wind strength in the Plio-Pleistocene eastern equatorial Pacific. *Paleogeography, Paleoclimatology, Paleoecology* **149**, 171-181 (1999).

65. Pike, J. & Kemp, A. E. S. Diatom mats in Gulf of California sediments: implications for the paleoenvironmental interpretation of laminated sediments and silica burial. *Geology* **27**, 311-314 (1999).

66. Koning, E. *et al*. Selective preservation of upwelling-indicating diatoms in sediments off Somalia, NW Indian Ocean. *Deep-Sea Research I* **48**, 2473-2495 (2001).

67. Dugdale, R. C., Barber, R. T., F., C., Peng, T.-H. & Wilkerson, F. P. One-dimensional ecosystem model of the equatorial Pacific upwelling system. Part II: sensitivity analysis and comparison with JGOFS EqPac data. *Deep-Sea Research II* **49**, 2747-2768 (2002).

68. Iriarte, J. L. & Fryxell, G. A. Micro-phytoplankton at the equatorial Pacific (140^{o} W) during the JGOFS EqPac Time Series studies: March to April and October 1992. *Deep-Sea Research II* **42**, 559-583 (1995).

69. Mayer, L. A. *et al*. (eds.) *Proceedings of the Ocean Drilling Program, Initial Reports, Leg 138* (College Station, TX (ODP), 1992).

70. Mayer, L. A. Extraction of high-resolution carbonate data for paleoclimatic reconstruction. *Nature* **352**, 148-150 (1991).

71. Shackleton, N. J., Crowhurst, S., Hagelberg, T., Pisias, N. G. & Schneider, D. A. A new late Neogene time scale: application to Leg 138 sites. *Proceedings of the Ocean Drilling Program, Scientific Results* **138**, 73-101 (1995).

72. Kemp, A. E. S., Pike, J., Pearce, R. B. & Lange, C. B. The "Fall dump" - a new perspective on the role of a "shade flora" in the annual cycle of diatom production and export flux. *Deep-Sea Research II* **47**, 2129-2154 (2000).

73. Scherer, R. P. A new method for the determination of absolute abundance of diatoms and other silt-sized sedimentary particles. *Journal of Paleoliminology* **12**, 171-179 (1994).

74. Schrader, H.-J. & Gersonde, R. Diatoms and Silicoflagellates. *Utrecht Micropaleontological Bulletin* **17**, 129-176 (1978).

75. Boden, P. Reproducibility in the random settling method for quantitative diatom analysis. *Micropaleontology* **37**, 313-319 (1991).

76. Moore, T. C. Method of randomly distributing grains for microscopic examination. *Journal of Sedimentary Petrology* **43**, 904-906 (1973).

77. Battarbee, R. W. A new method for the estimation of absolute microfossil numbers, with reference especially to diatoms. *Limnology and Oceanography* **18**, 647-652 (1973).

78. Battarbee, R. W. & Kneen, M. J. The use of electronically counted microspheres in absolute diatom analysis. *Limnology and Oceanography* **27**, 184-188 (1982).

79. Shaw, A. B. *Time in Stratigraphy* (ed. Shrock, R. R.) (McGraw - Hill Book Company, New York, 1964).

80. Barcena, M. A. & Abrantes, F. Evidence of a high-productivity area off the coast of Malaga from studies of diatoms in surface sediments. *Marine Micropaleontology* **35**, 91-103 (1998).

81. Romero, O. E., Hebbeln, D. & Wefer, G. Temporal and spatial variability in export production in the SE Pacific Ocean: evidence from siliceous plankton fluxes and surface sediment assemblages. *Deep-Sea Research I* **48**, 2673-2697 (2001).

82. Kobayashi, F. & Takahashi, K. Distribution of diatoms along the equatorial transect in the western and central Pacific during the 1999 La Nina conditions. *Deep-Sea Research II* **49**, 2801-2821 (2002).

APPENDIX A

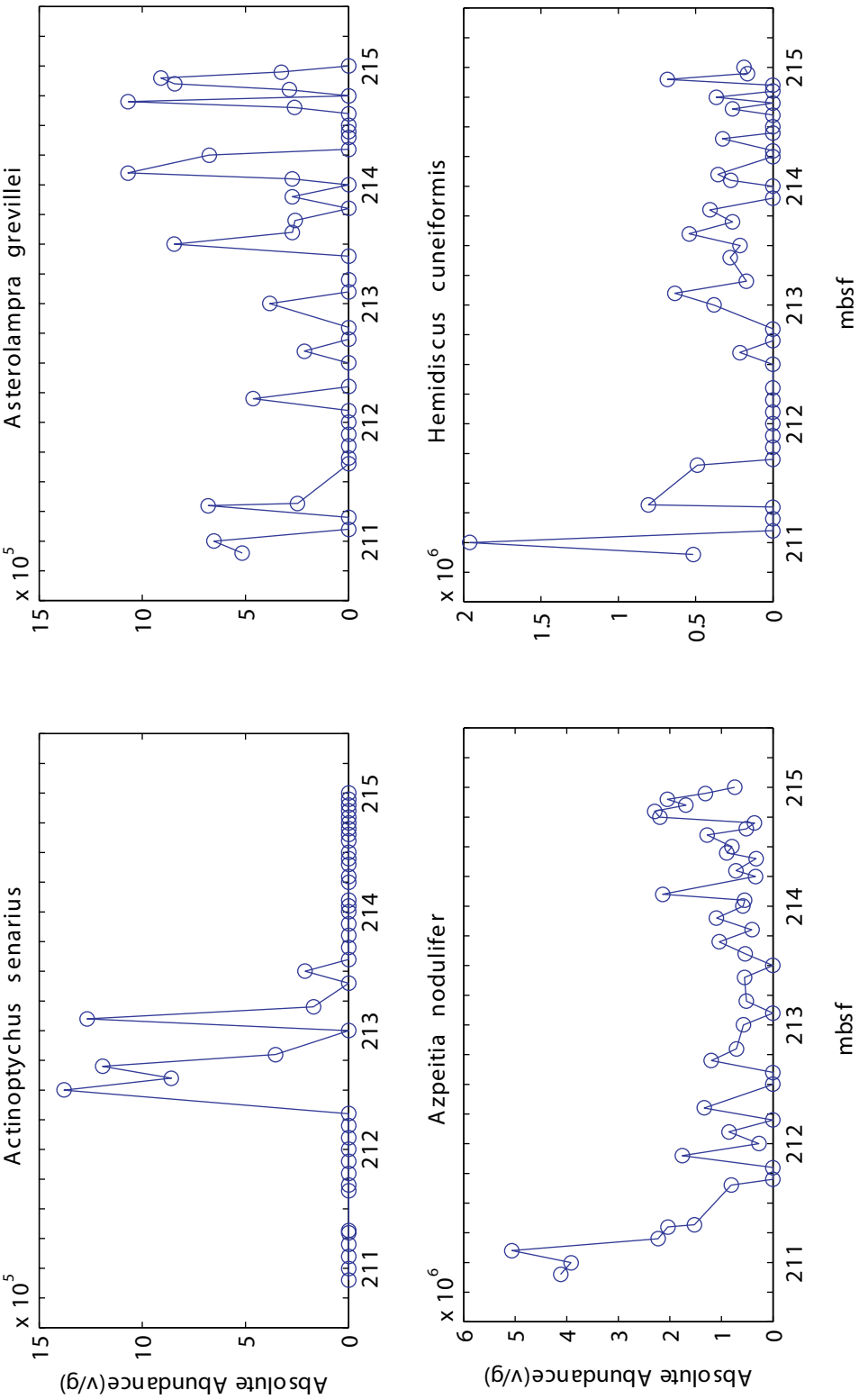

Figure A-1A Individual species absolute abundance with laminae averages.

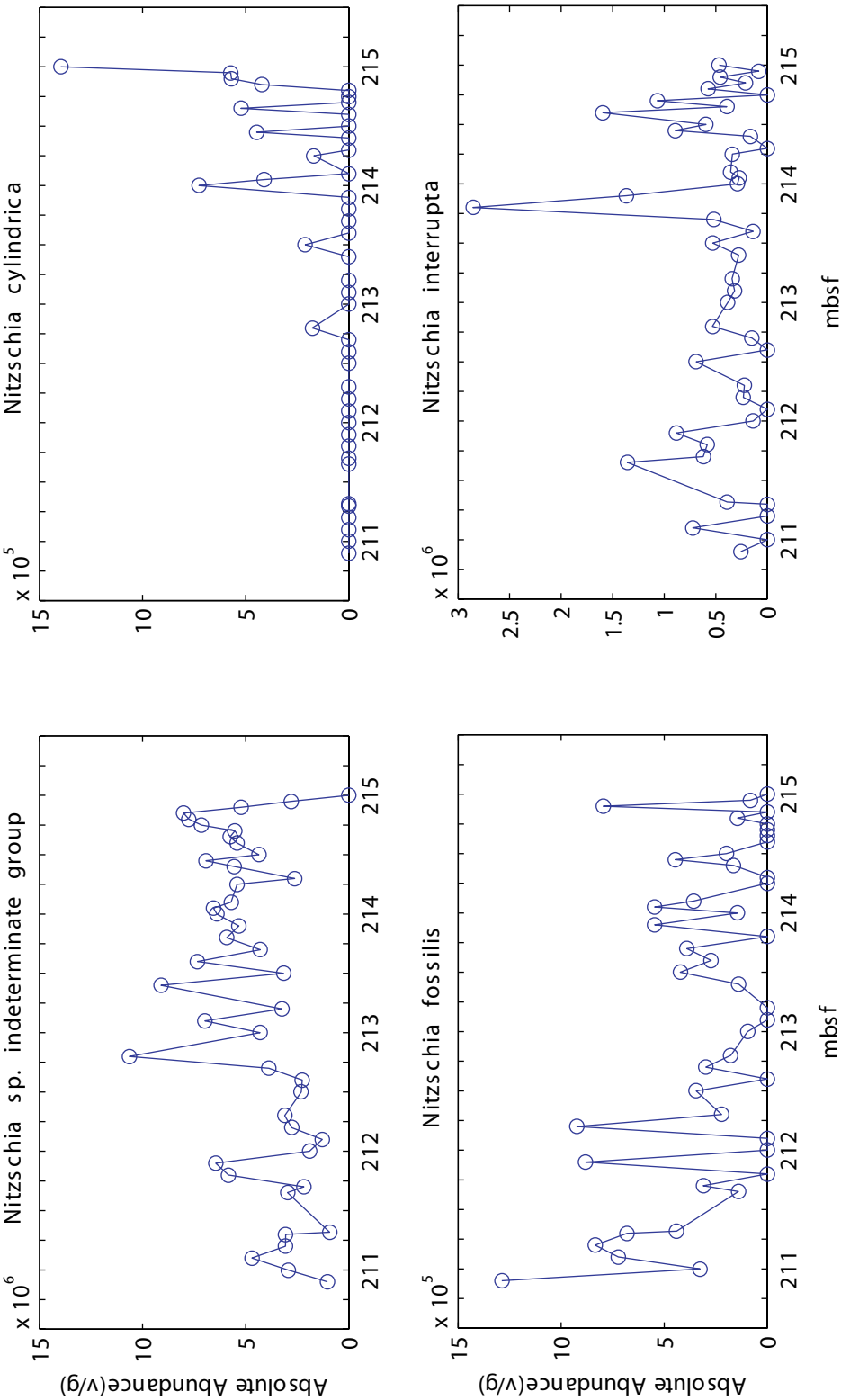

Figure A-1B Individual species absolute abundance with laminae averages (continued).

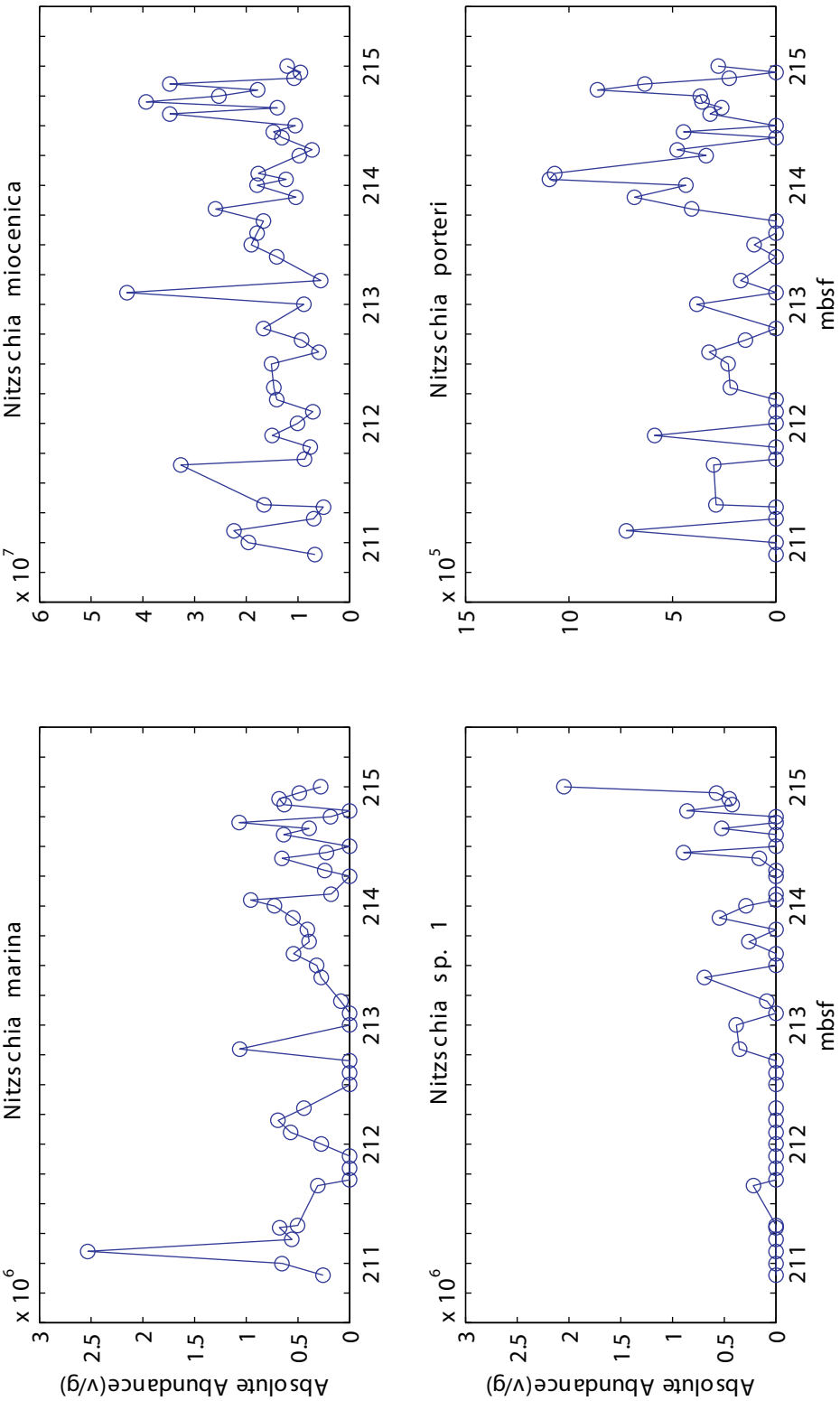

Figure A-1C Individual species absolute abundance with laminae averages (continued).

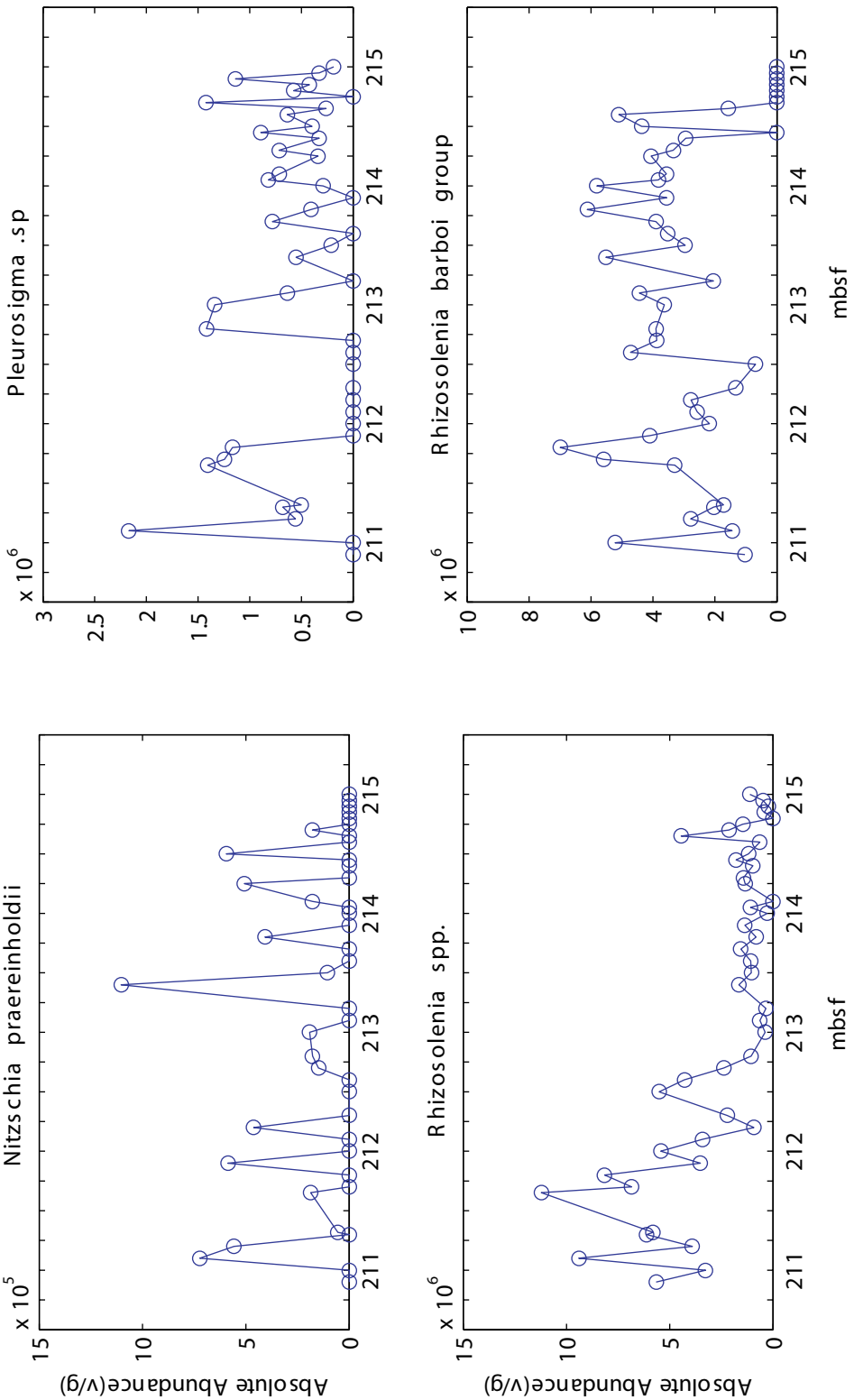

Figure A-1D Individual species absolute abundance with laminae averages (continued).

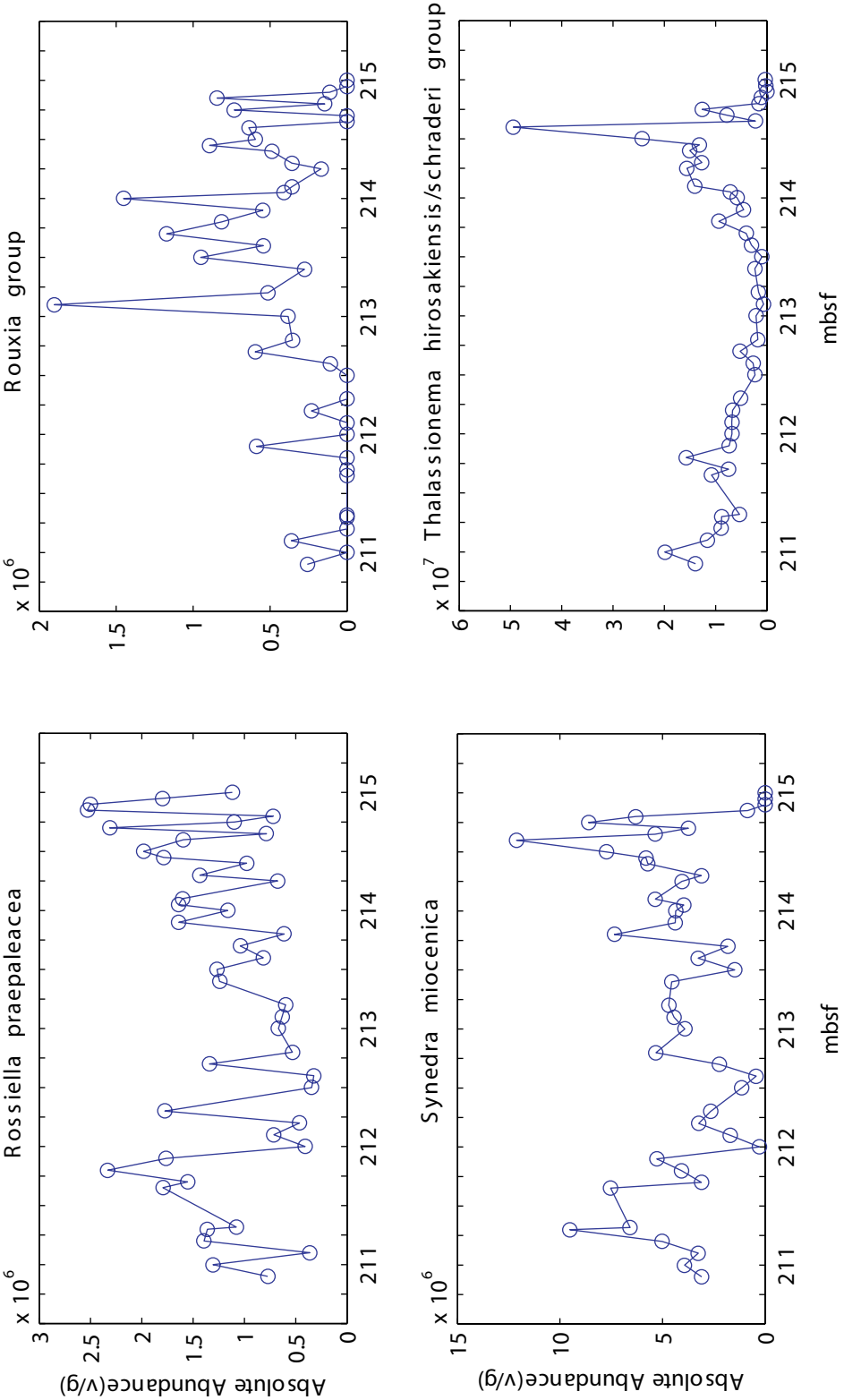

Figure A-1E Individual species absolute abundance with laminae averages (continued).

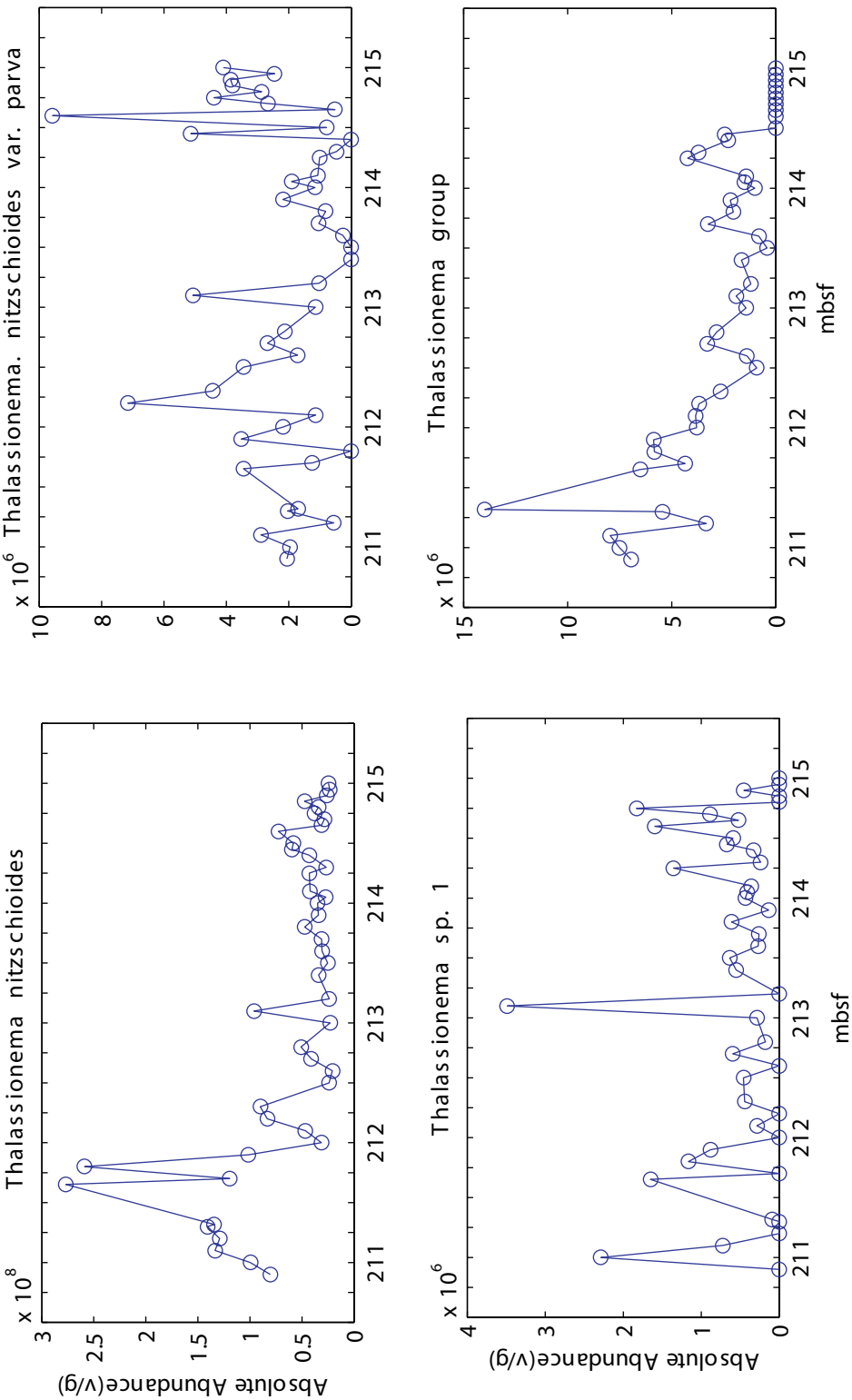

Figure A-1F Individual species absolute abundance with laminae averages (continued).

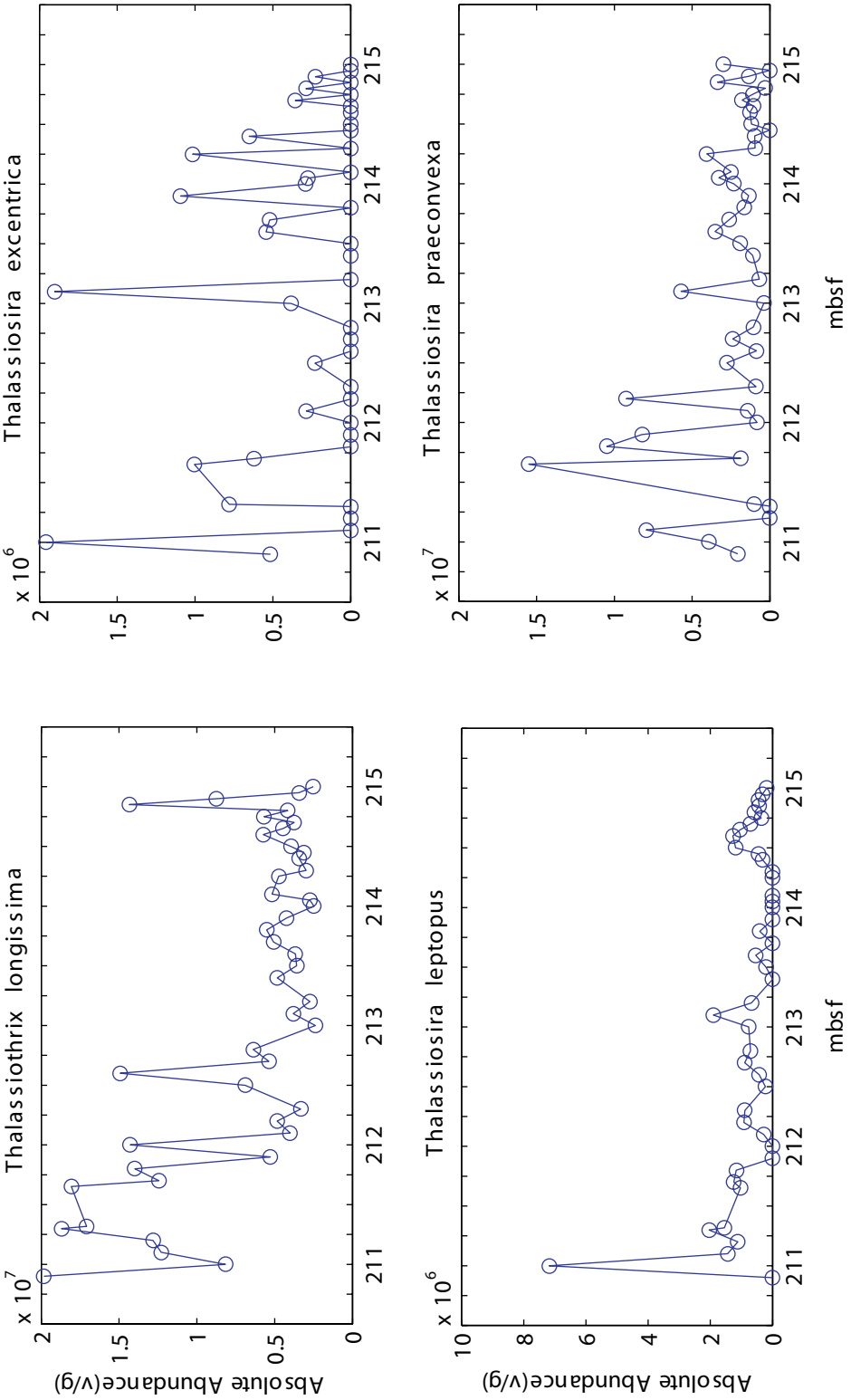

Figure A-1G Individual species absolute abundance with laminae averages (continued).

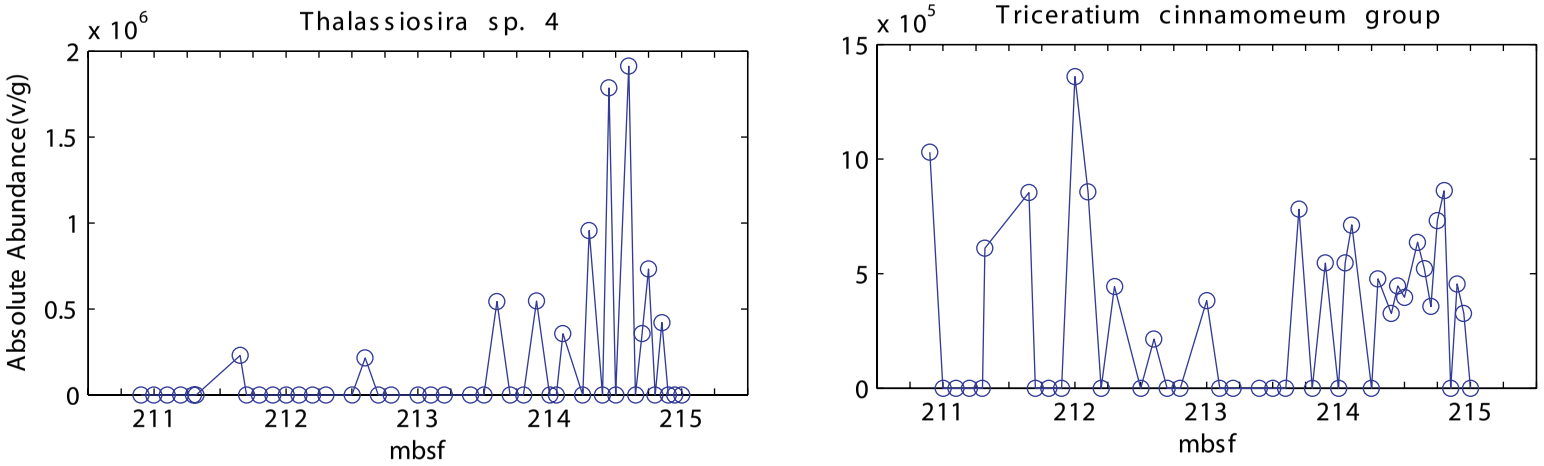

Figure A-1H Individual species absolute abundance with laminae averages (continued).

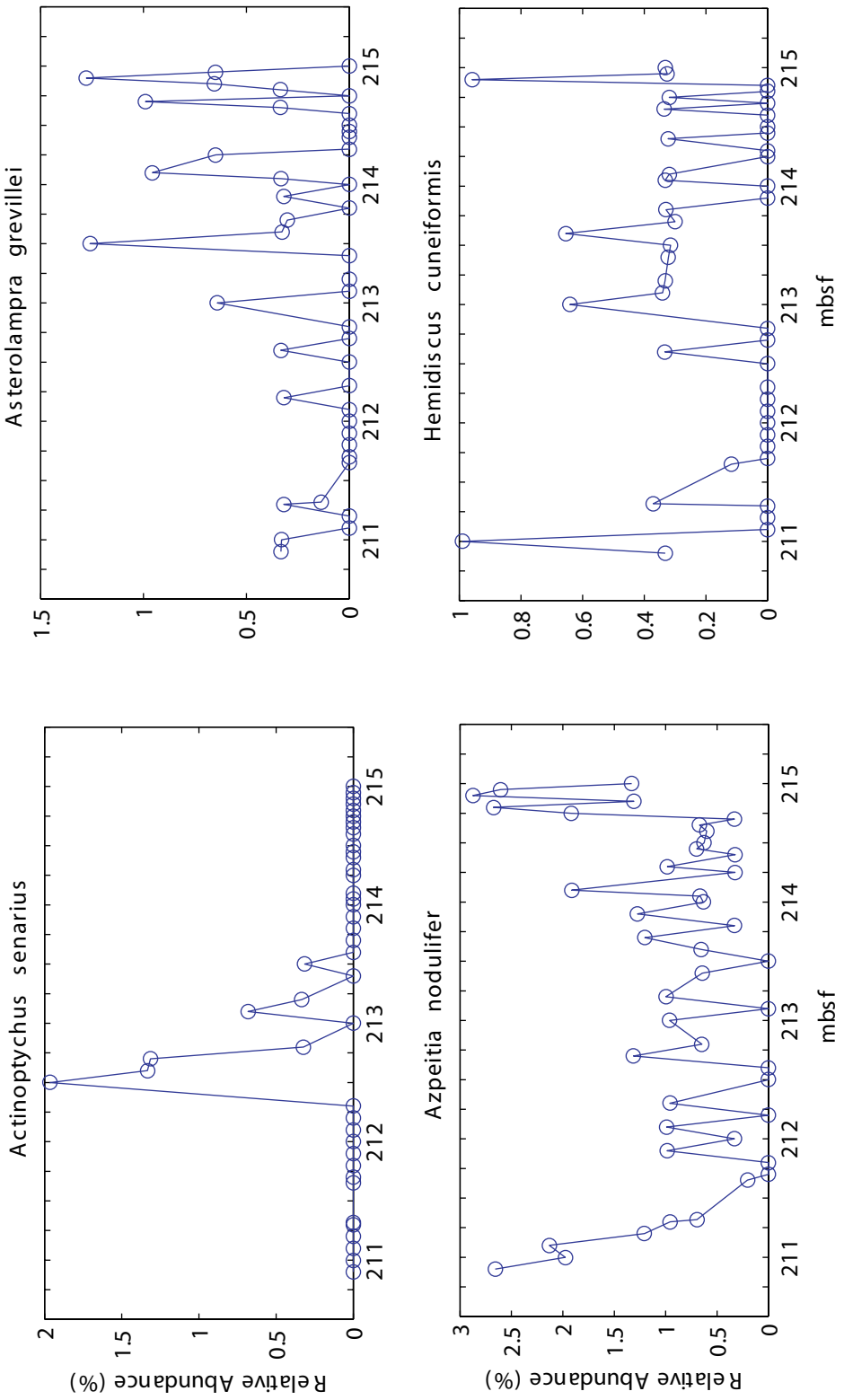

Figure A-2A Individual species relative abundance with laminae averages.

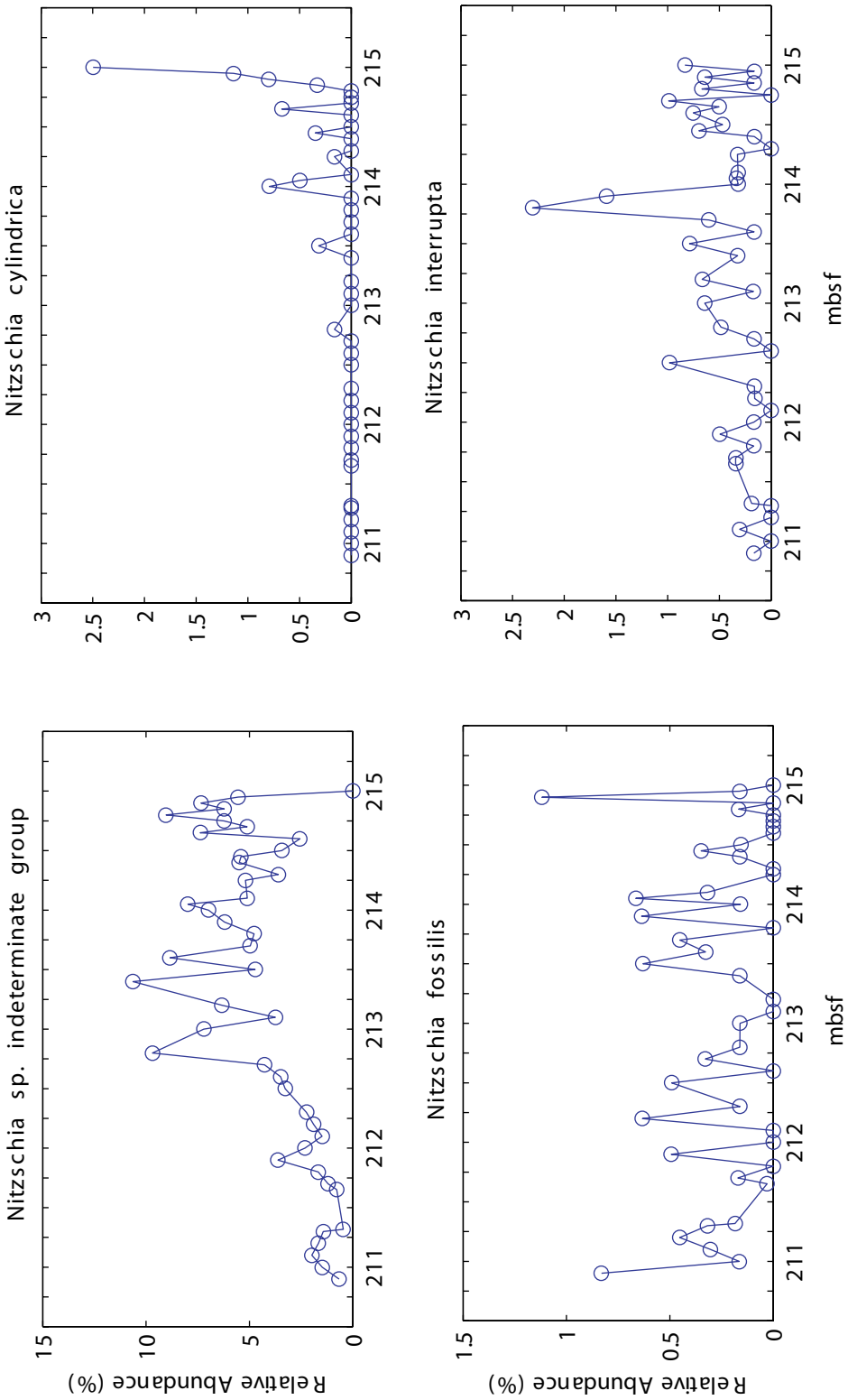

Figure A-2B Individual species relative abundance with laminae averages (continued).

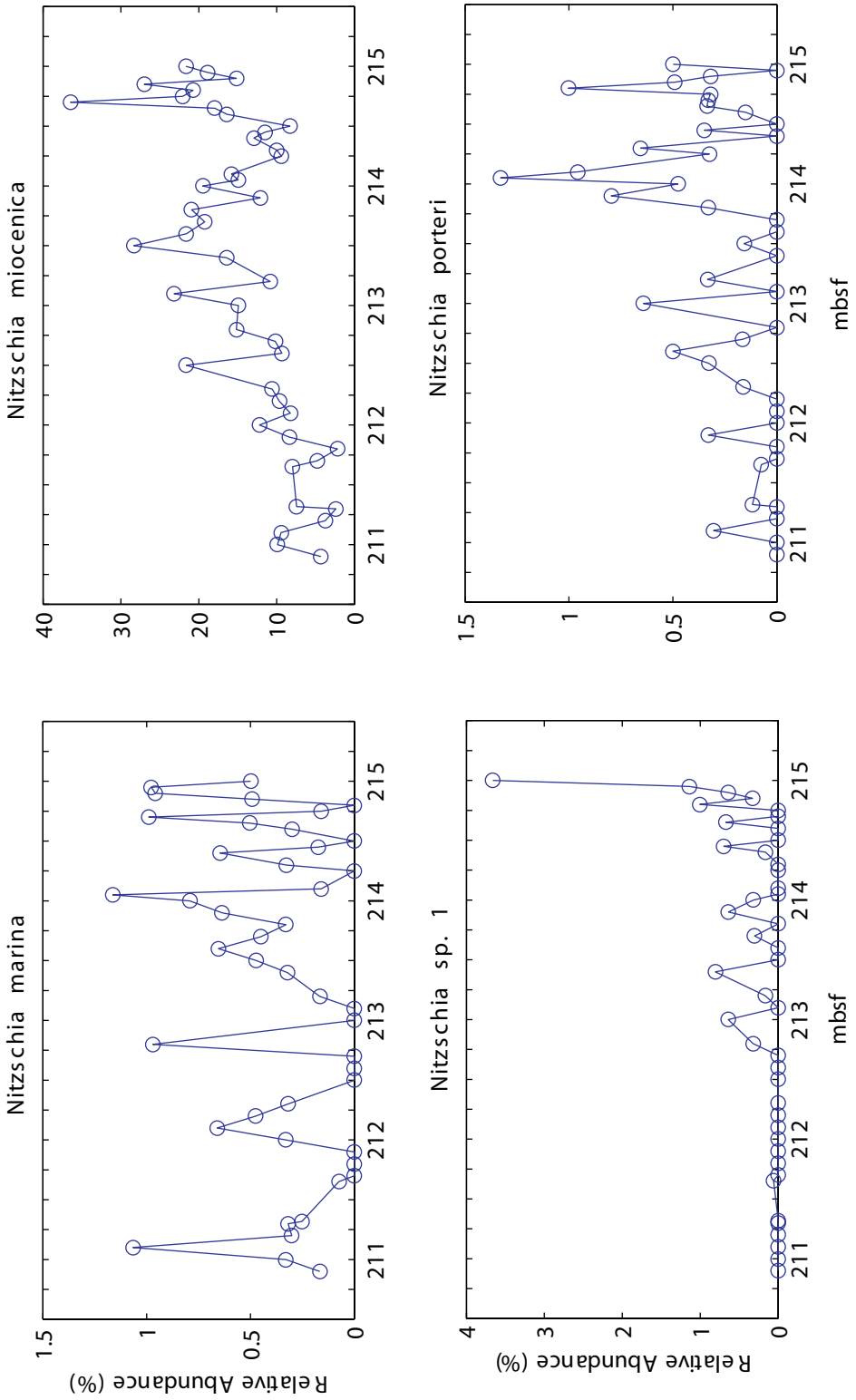

Figure A-2C Individual species relative abundance with laminae averages (continued).

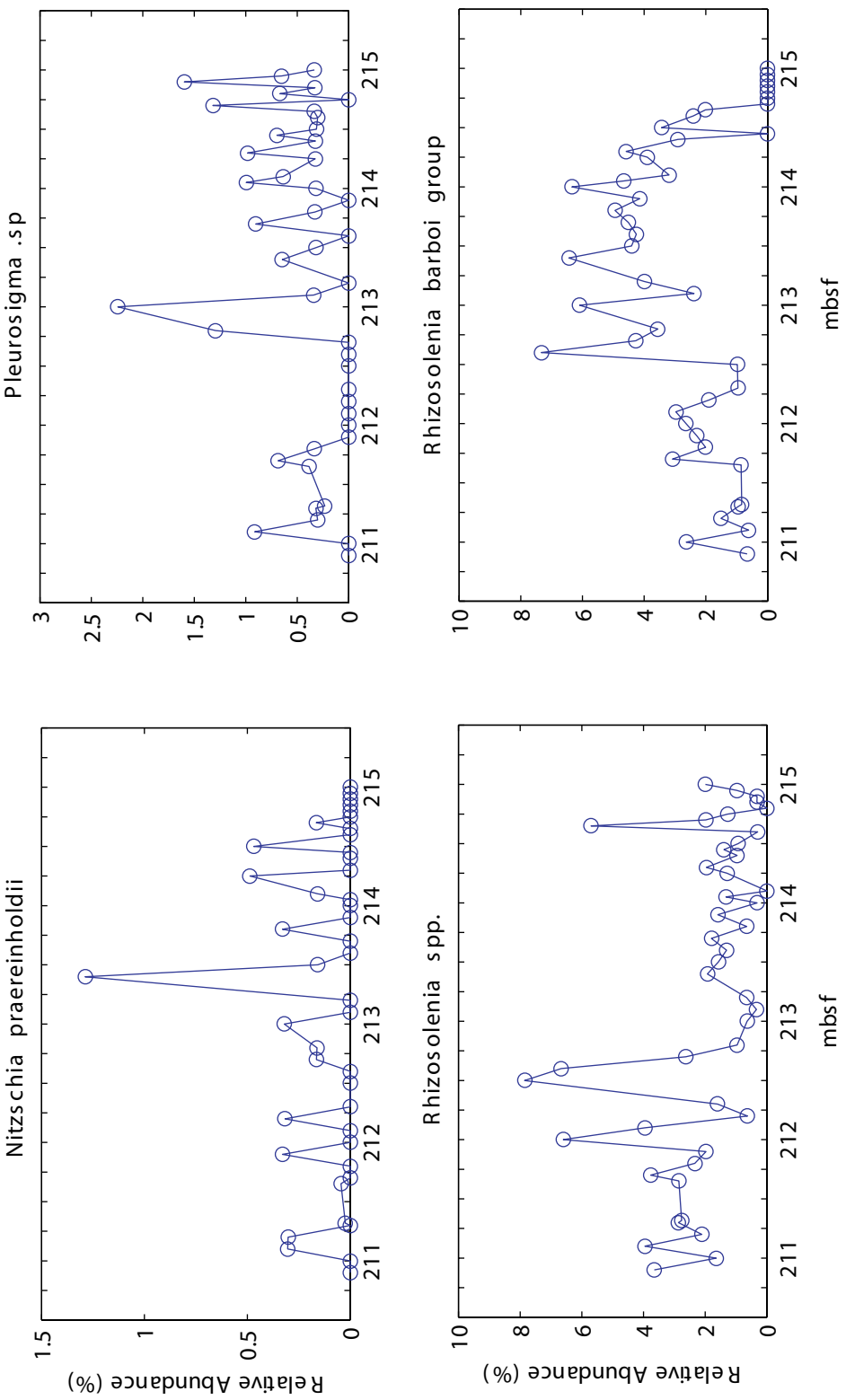

Figure A-2D Individual species relative abundance with laminae averages (continued).

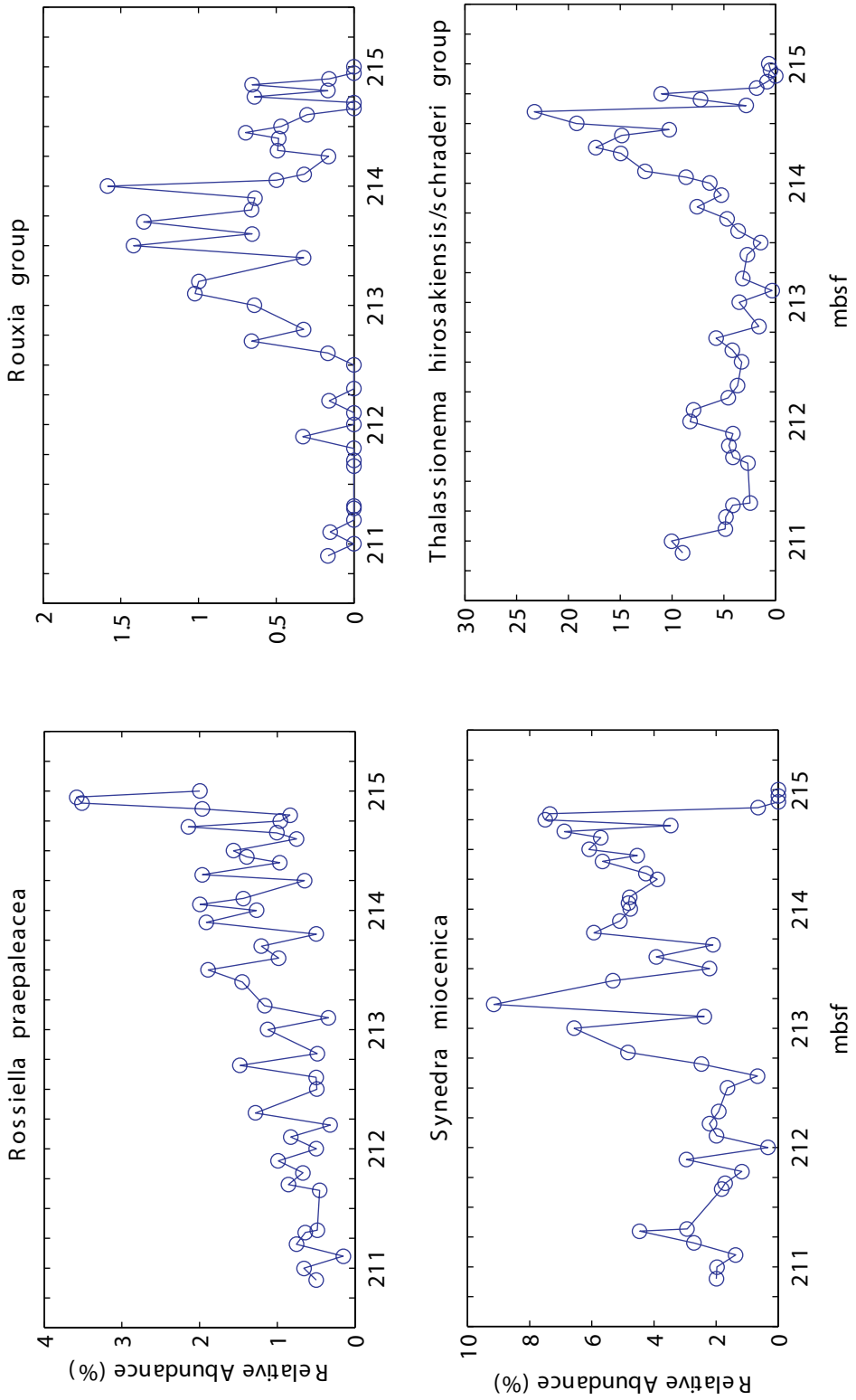

Figure A-2E Individual species relative abundance with laminae averages (continued).

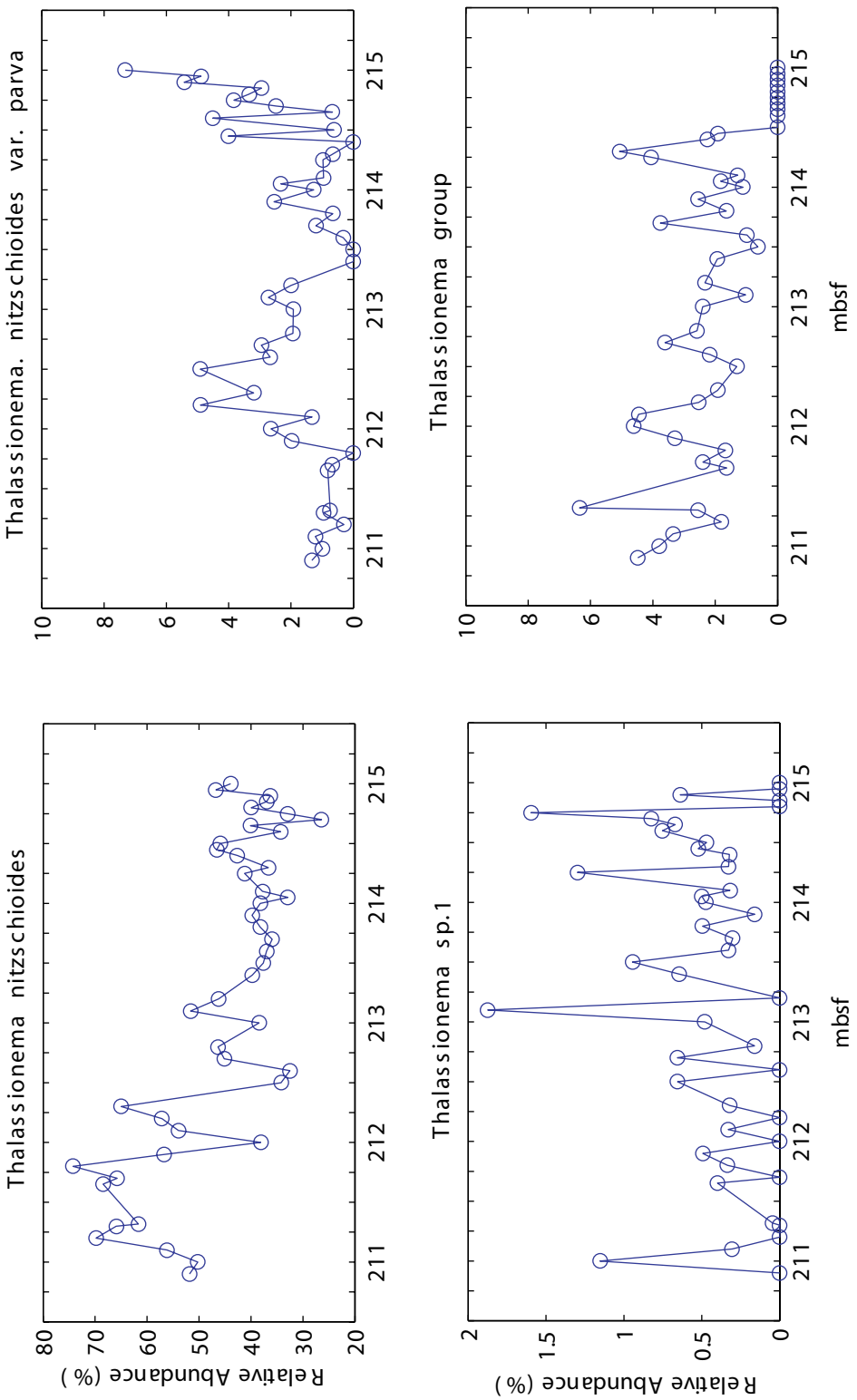

Figure A-2F Individual species relative abundance with laminae averages (continued).

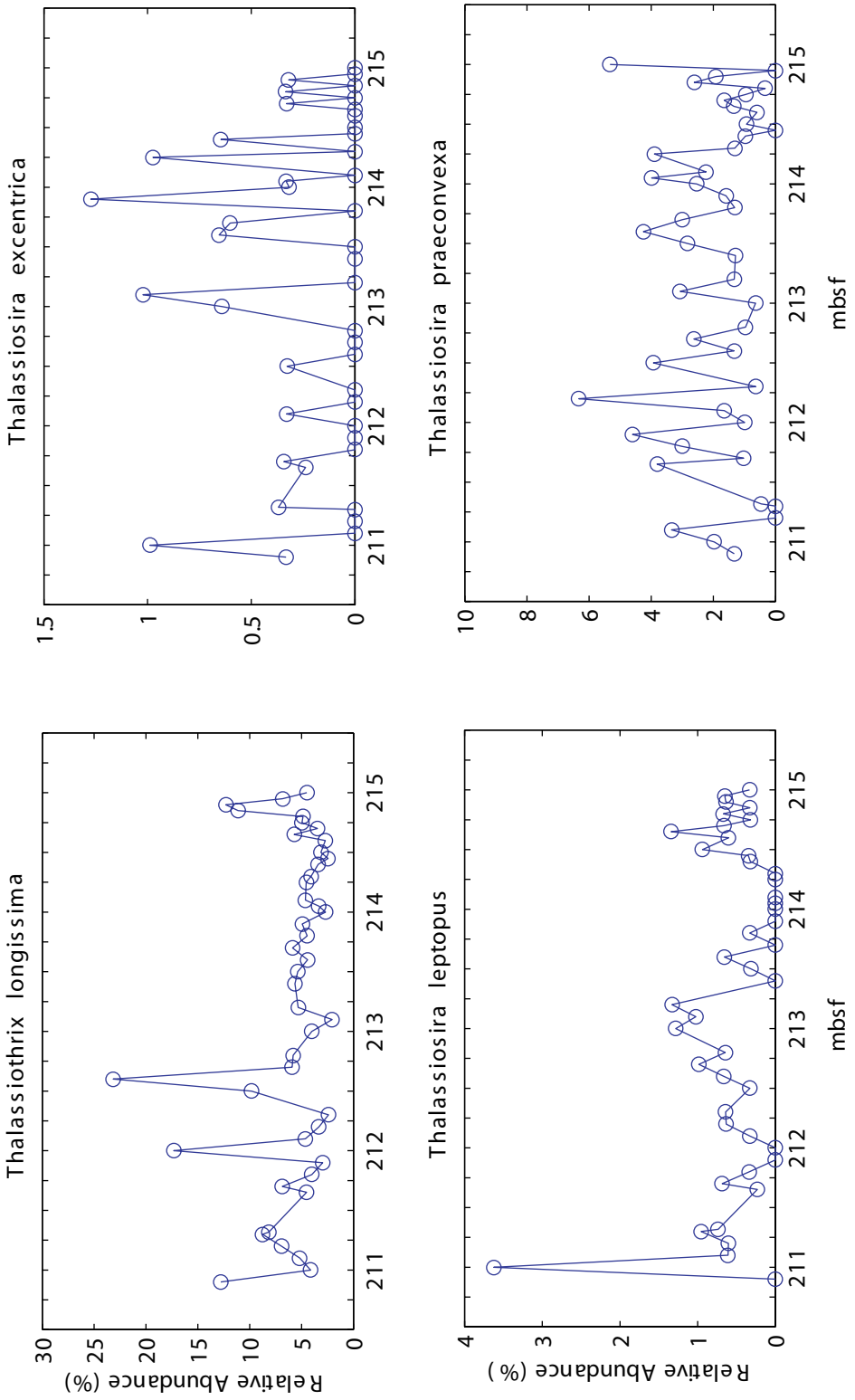

Figure A-2G Individual species relative abundance with laminae averages (continued).

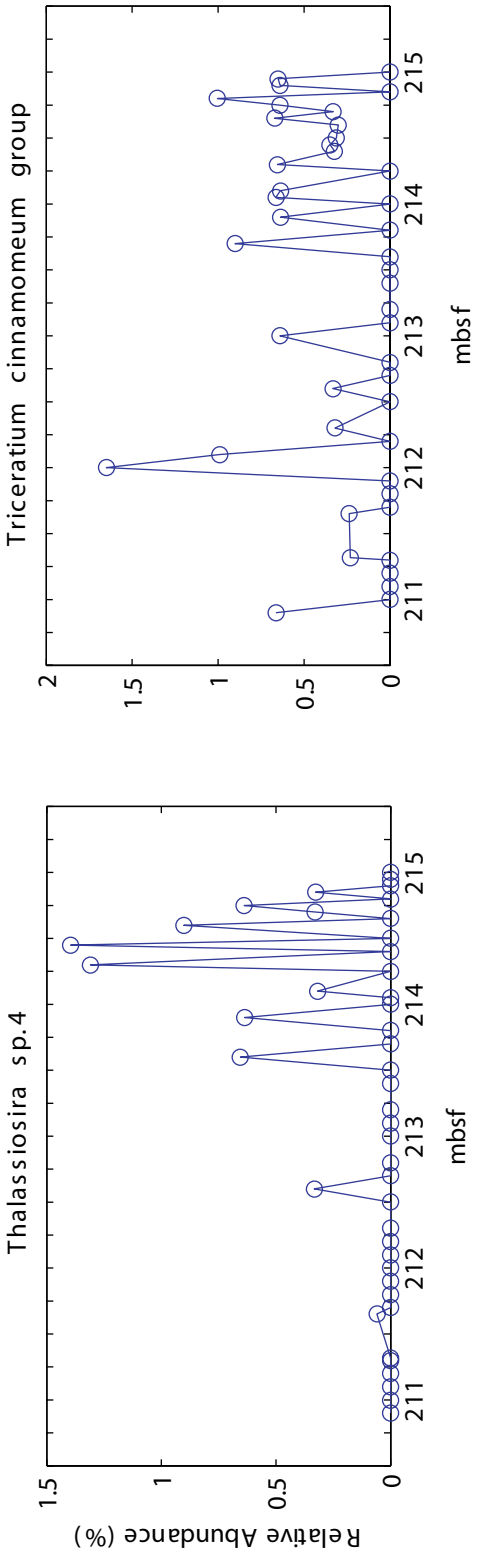

Figure A-2H Individual species relative abundance with laminae averages (continued).

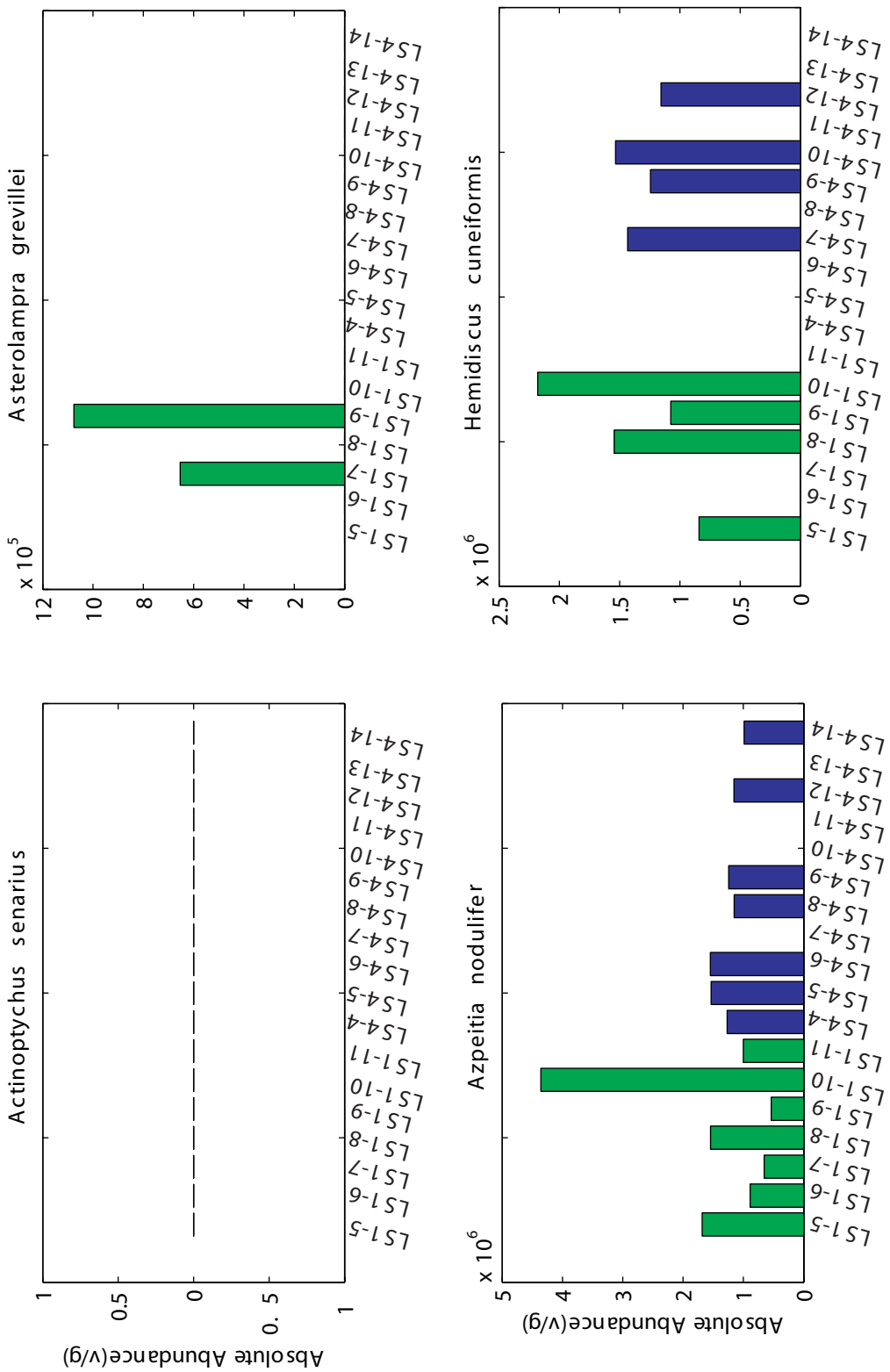

Figure A-3A Individual species absolute abundance for LS4 (blue) and LS1 (green).

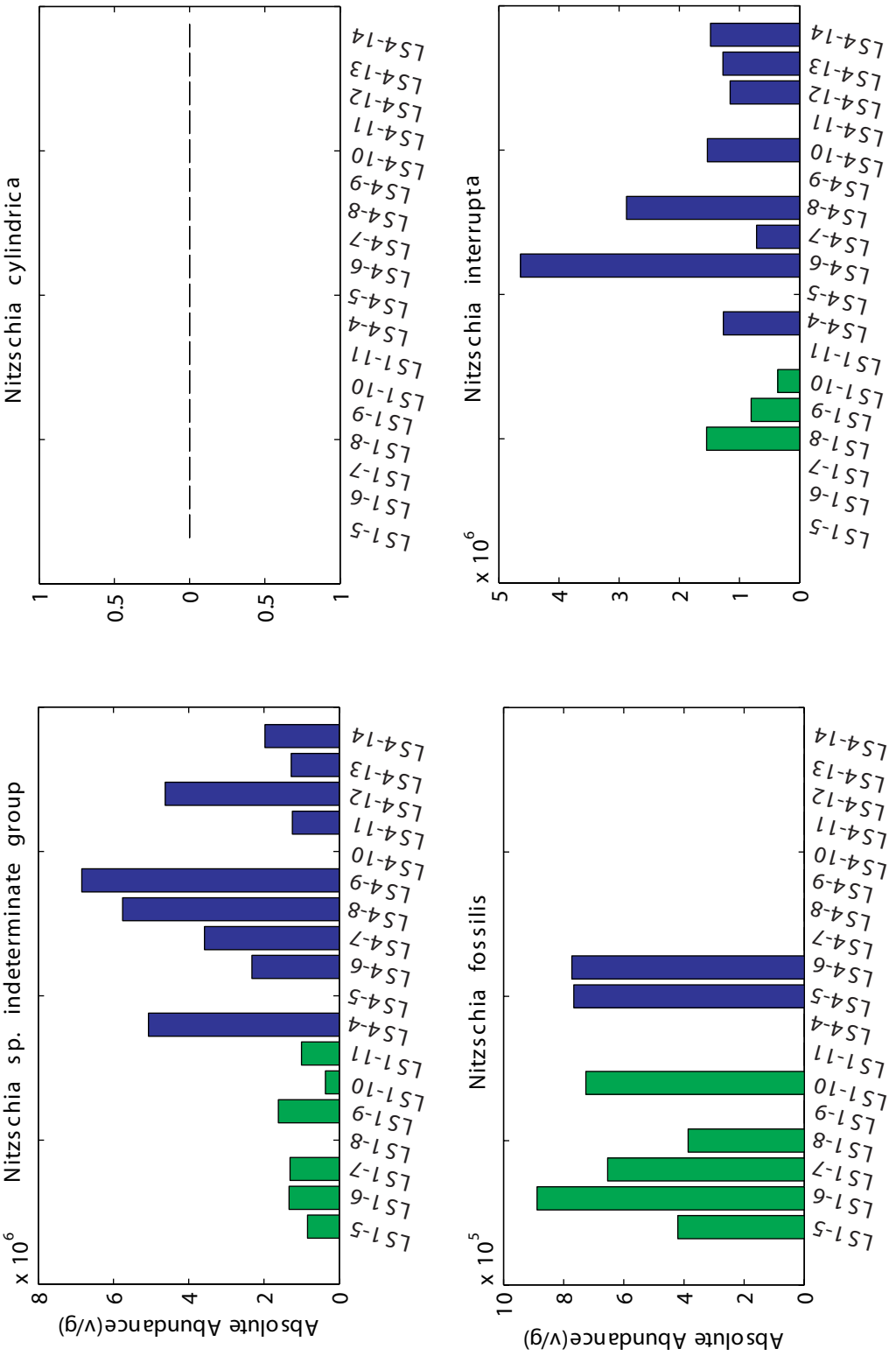

Figure A-3B Individual species absolute abundance for LS4 (blue) and LS1 (green)(continued).

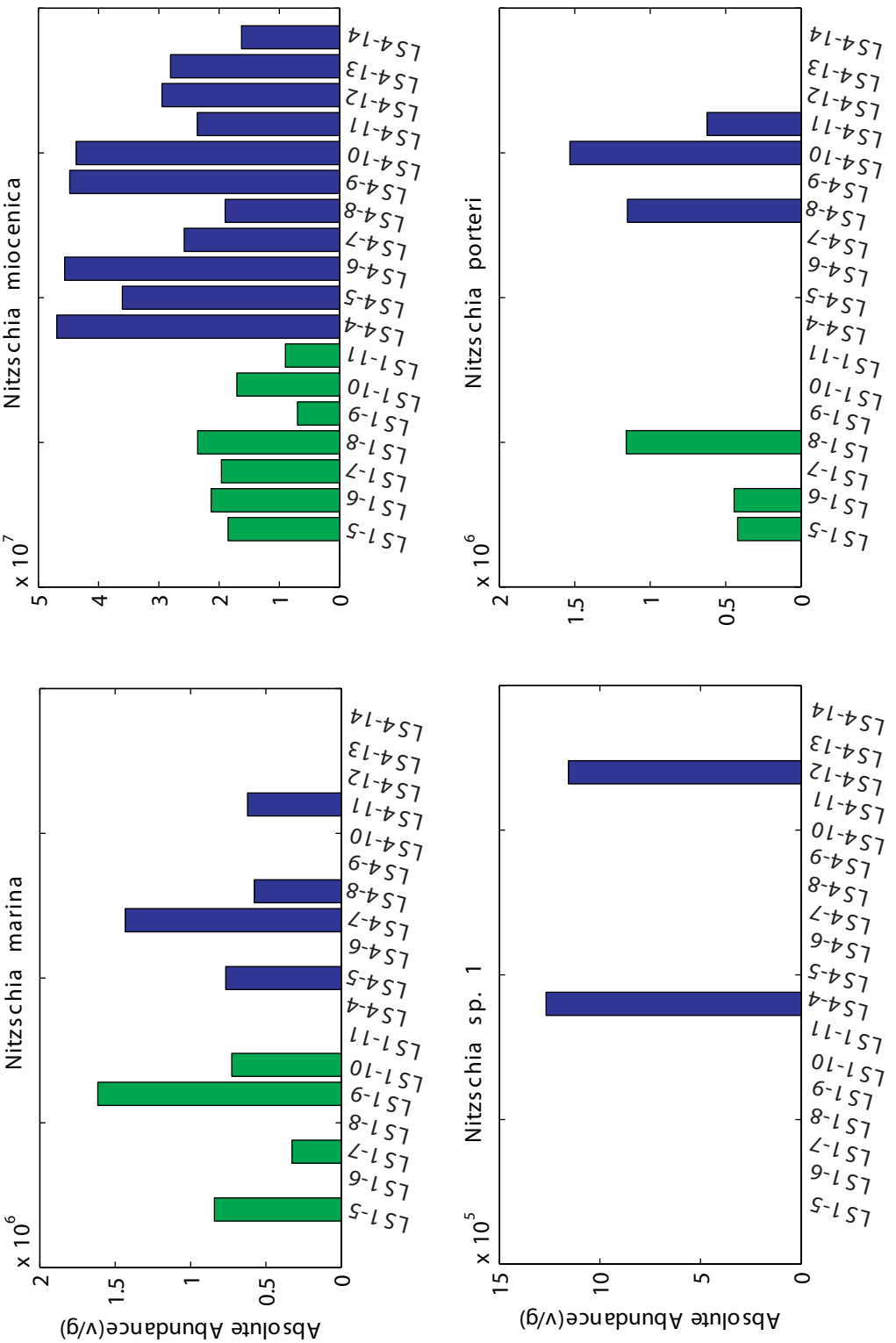

Figure A-3C Individual species absolute abundance for LS4 (blue) and LS1 (green)(continued).

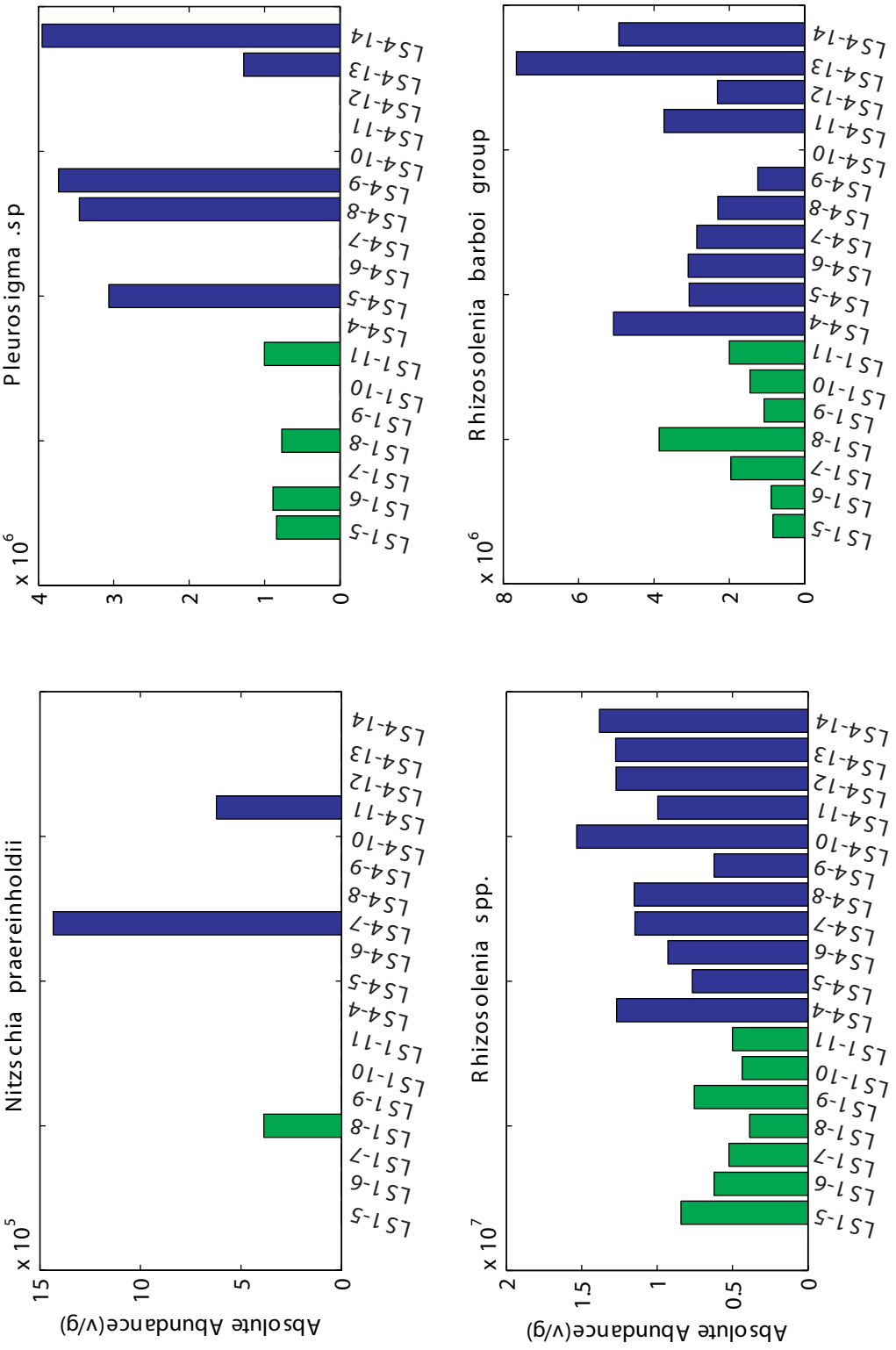

Figure A-3D Individual species absolute abundance for LS4 (blue) and LS1 (green)(continued).

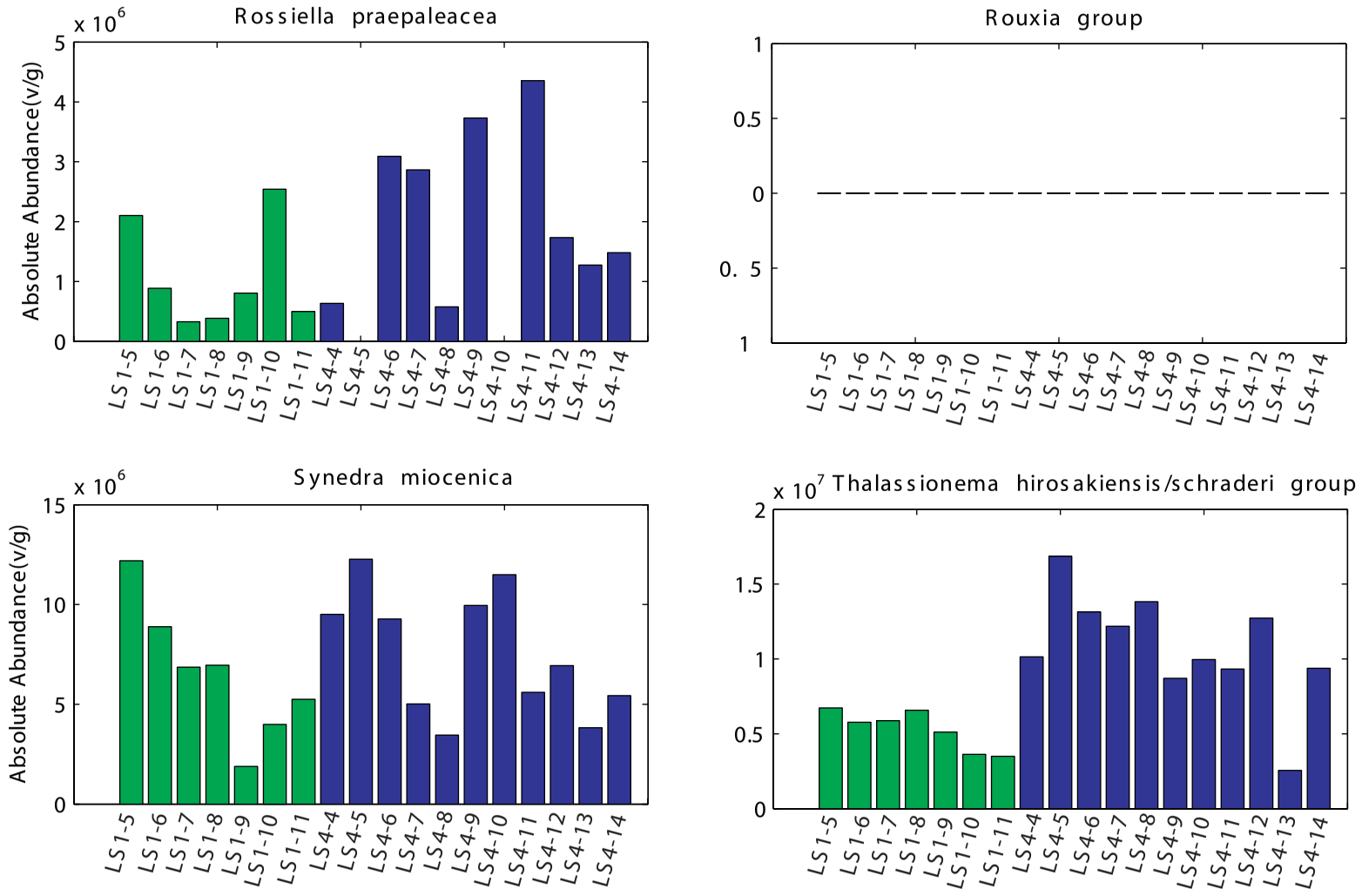

Figure A-3E Individual species absolute abundance for LS4 (blue) and LS1 (green)(continued).

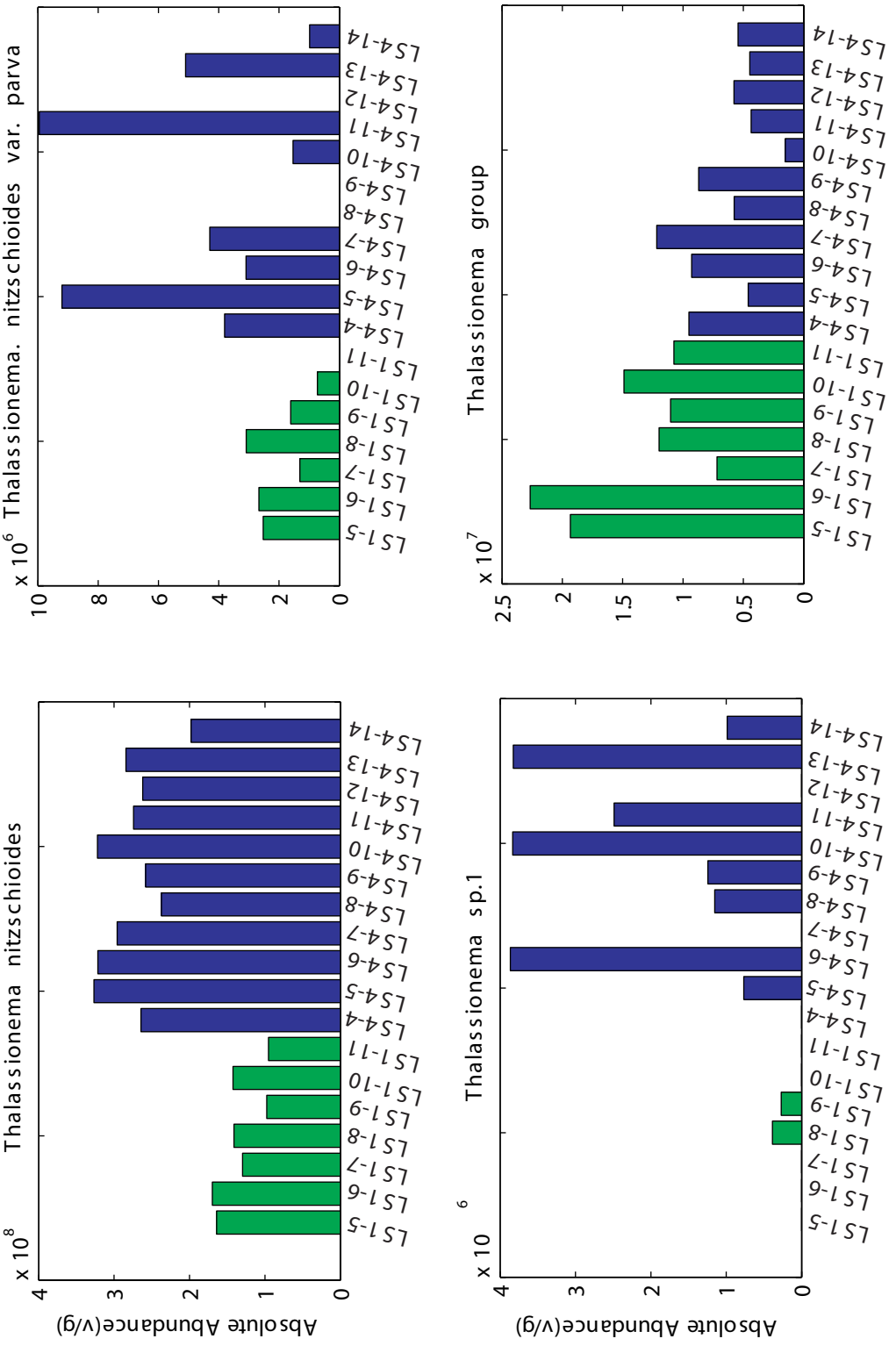

Figure A-3F Individual species absolute abundance for LS4 (blue) and LS1 (green)(continued).

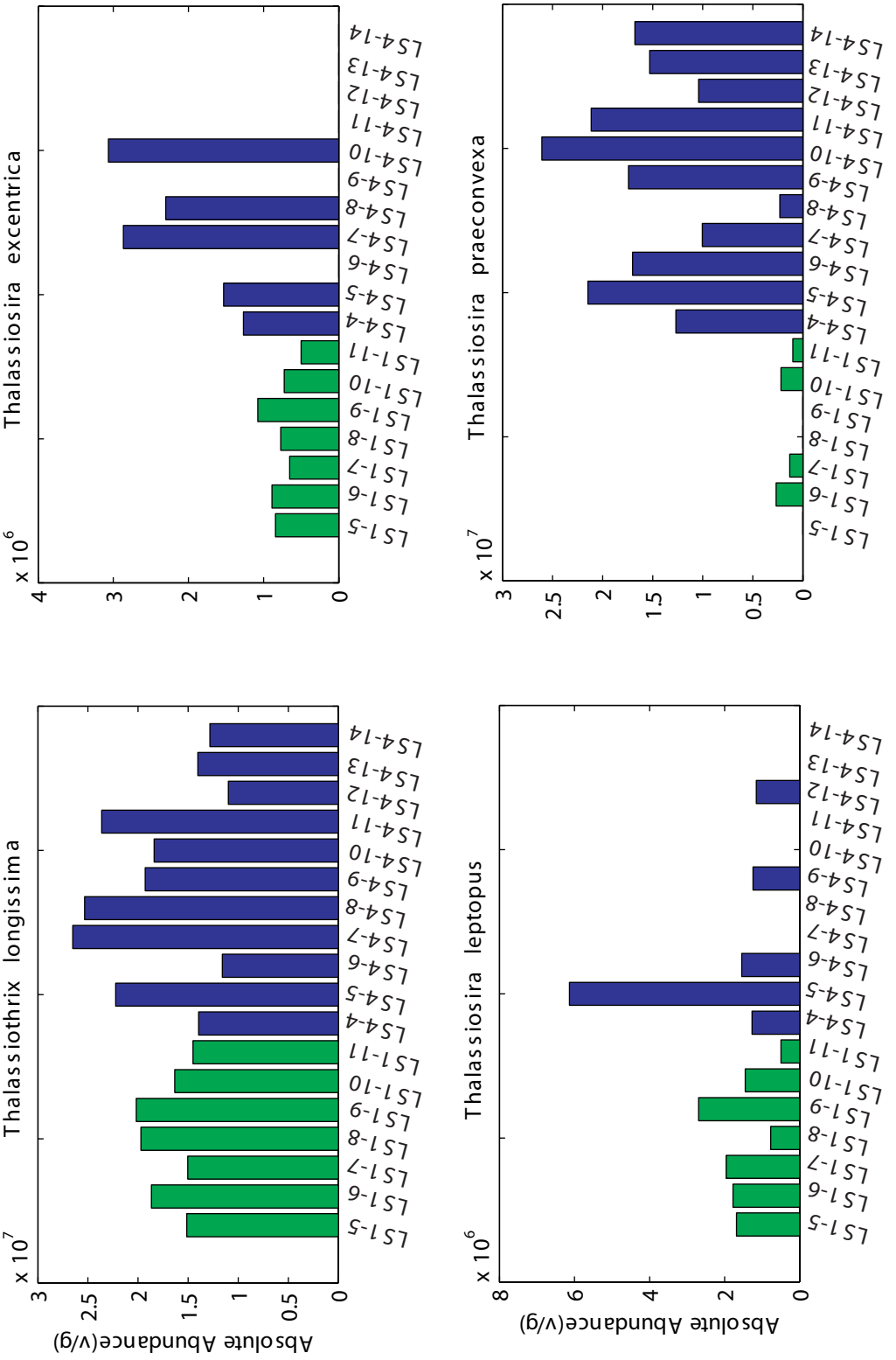

Figure A-3G Individual species absolute abundance for LS4 (blue) and LS1 (green)(continued).

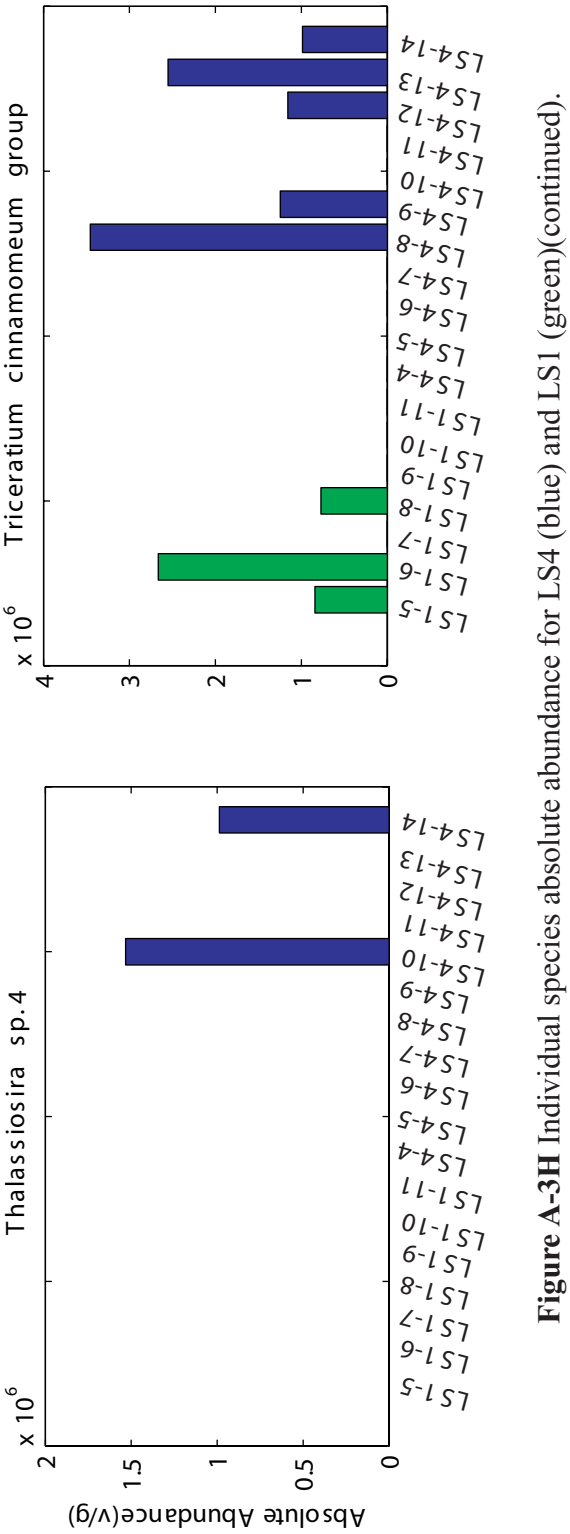

Figure A-3H Individual species absolute abundance for LS4 (blue) and LS1 (green)(continued).

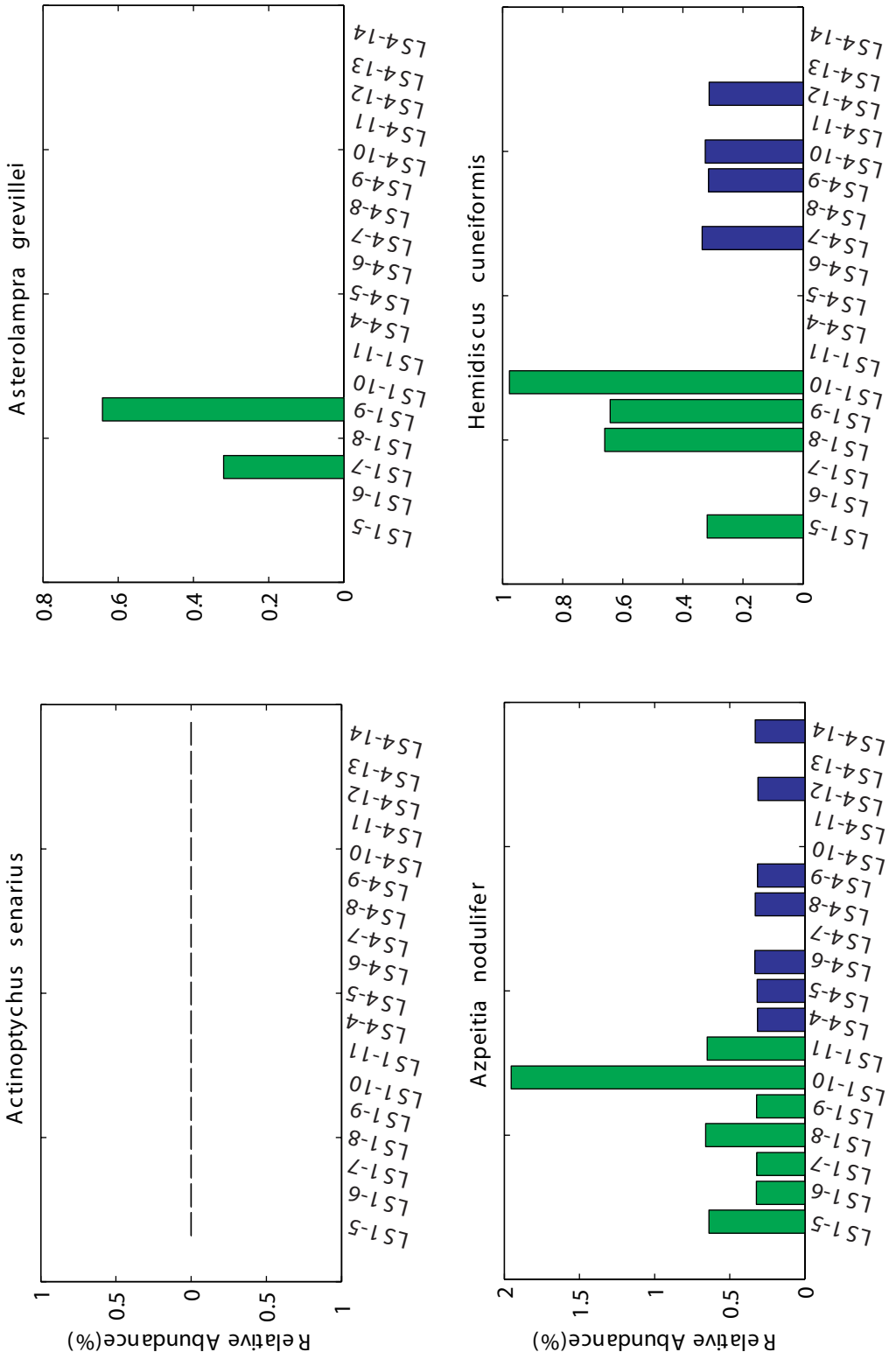

Figure A-4A Individual species relative abundance for LS4 (blue) and LS1 (green).

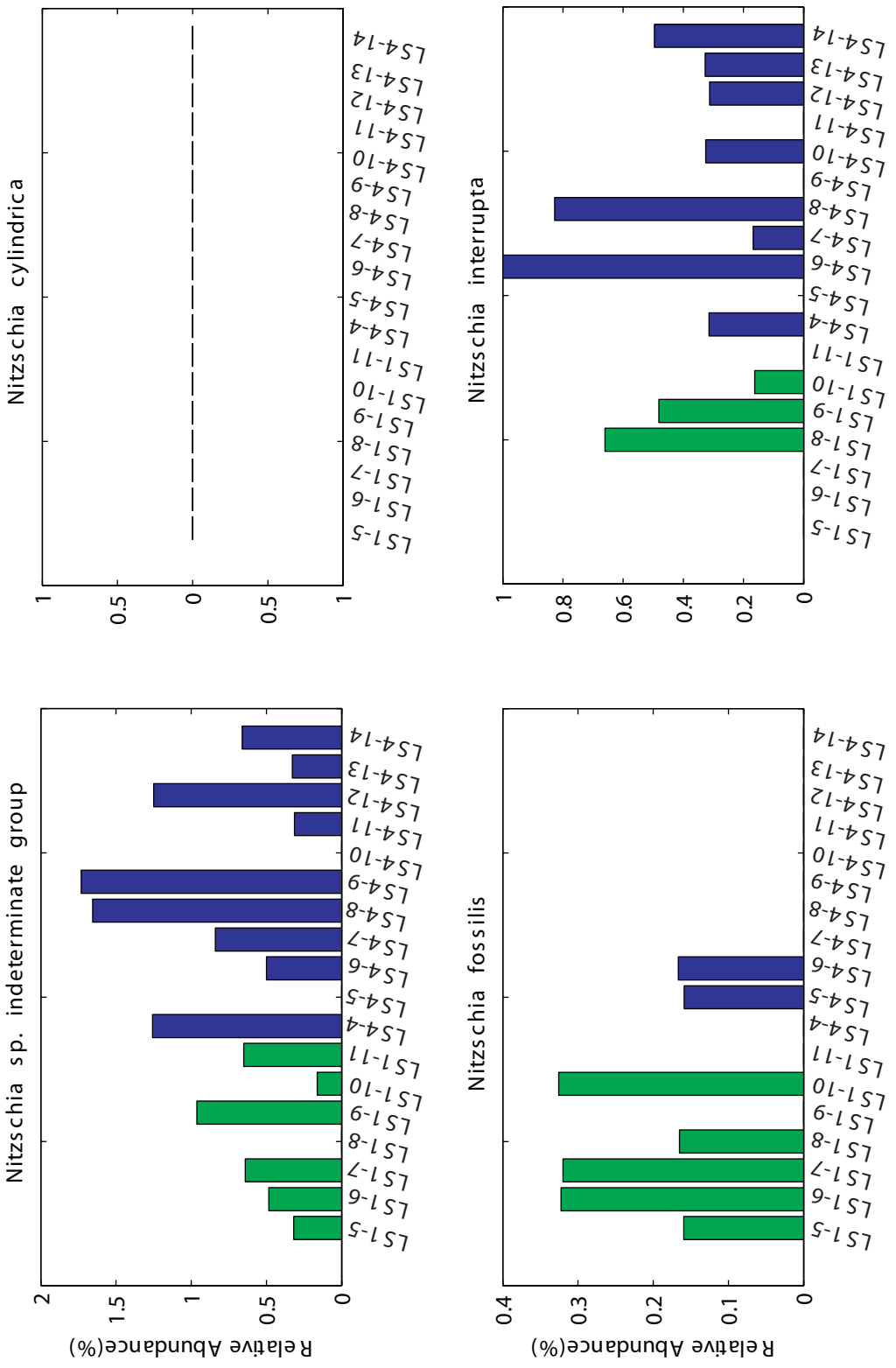

Figure A-4B Individual species relative abundance for LS4 (blue) and LS1 (green) (continued).

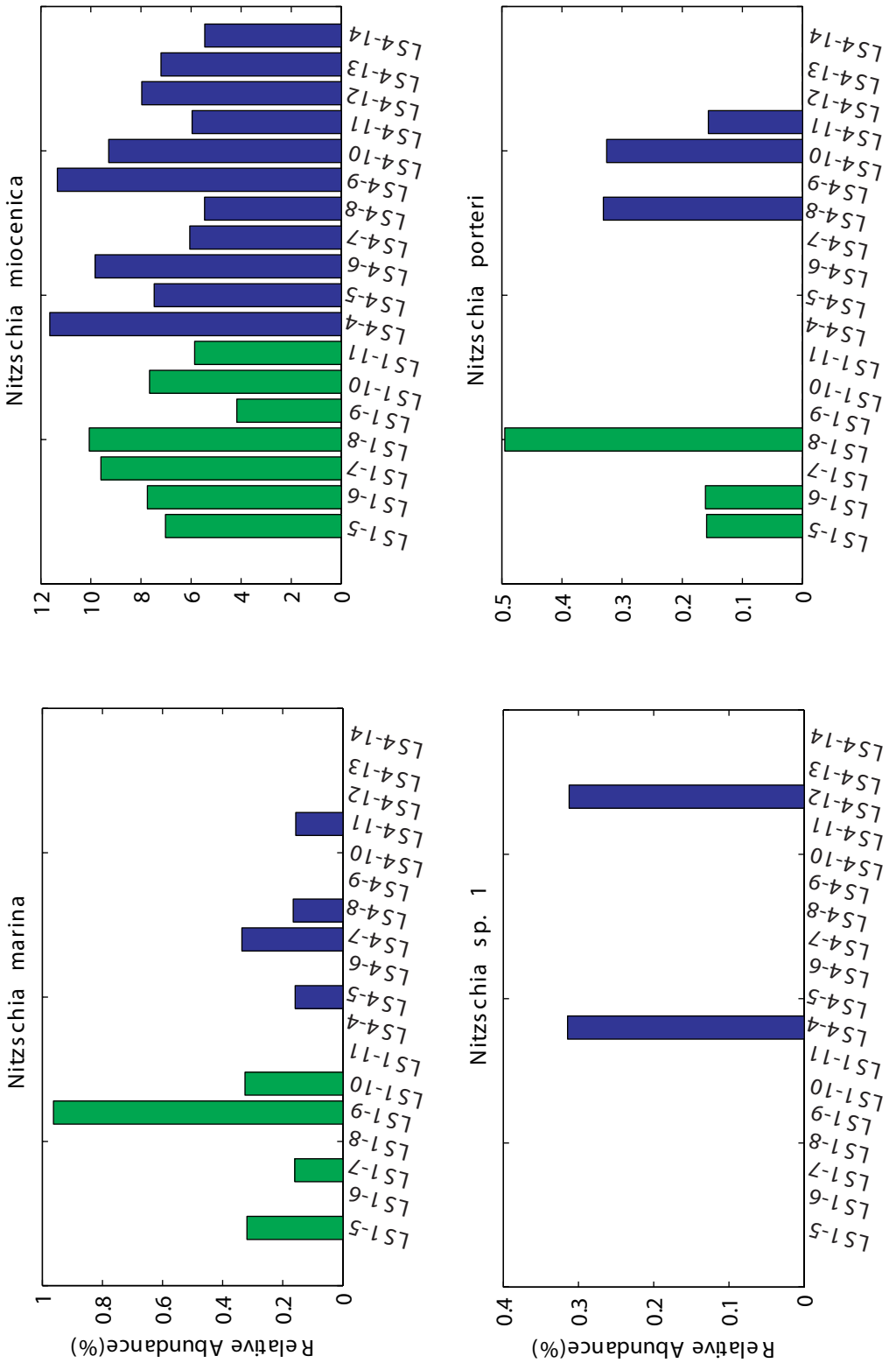

Figure A-4C Individual species relative abundance for LS4 (blue) and LS1 (green) (continued).

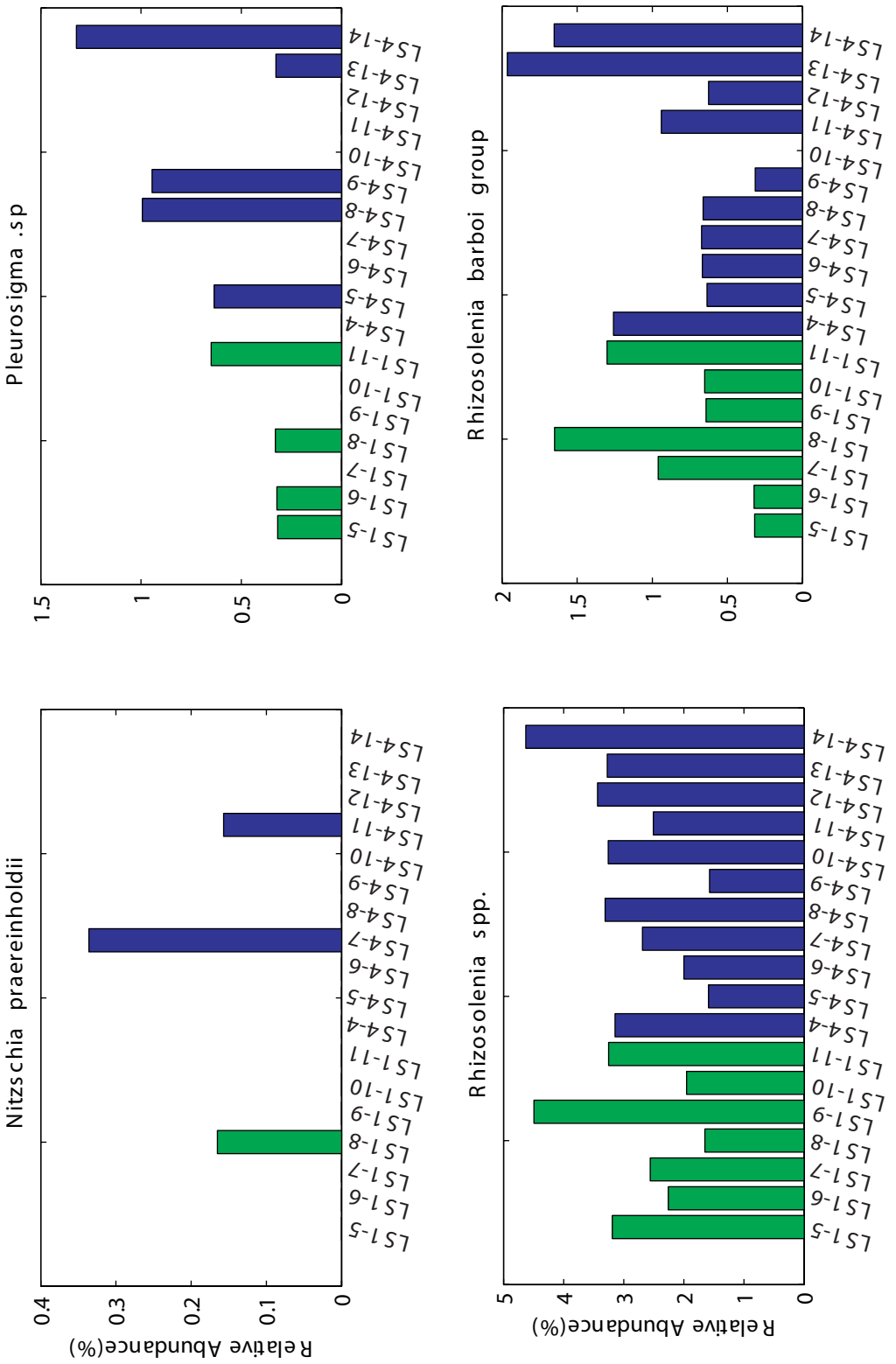

Figure A-4D Individual species relative abundance for LS4 (blue) and LS1 (green) (continued).

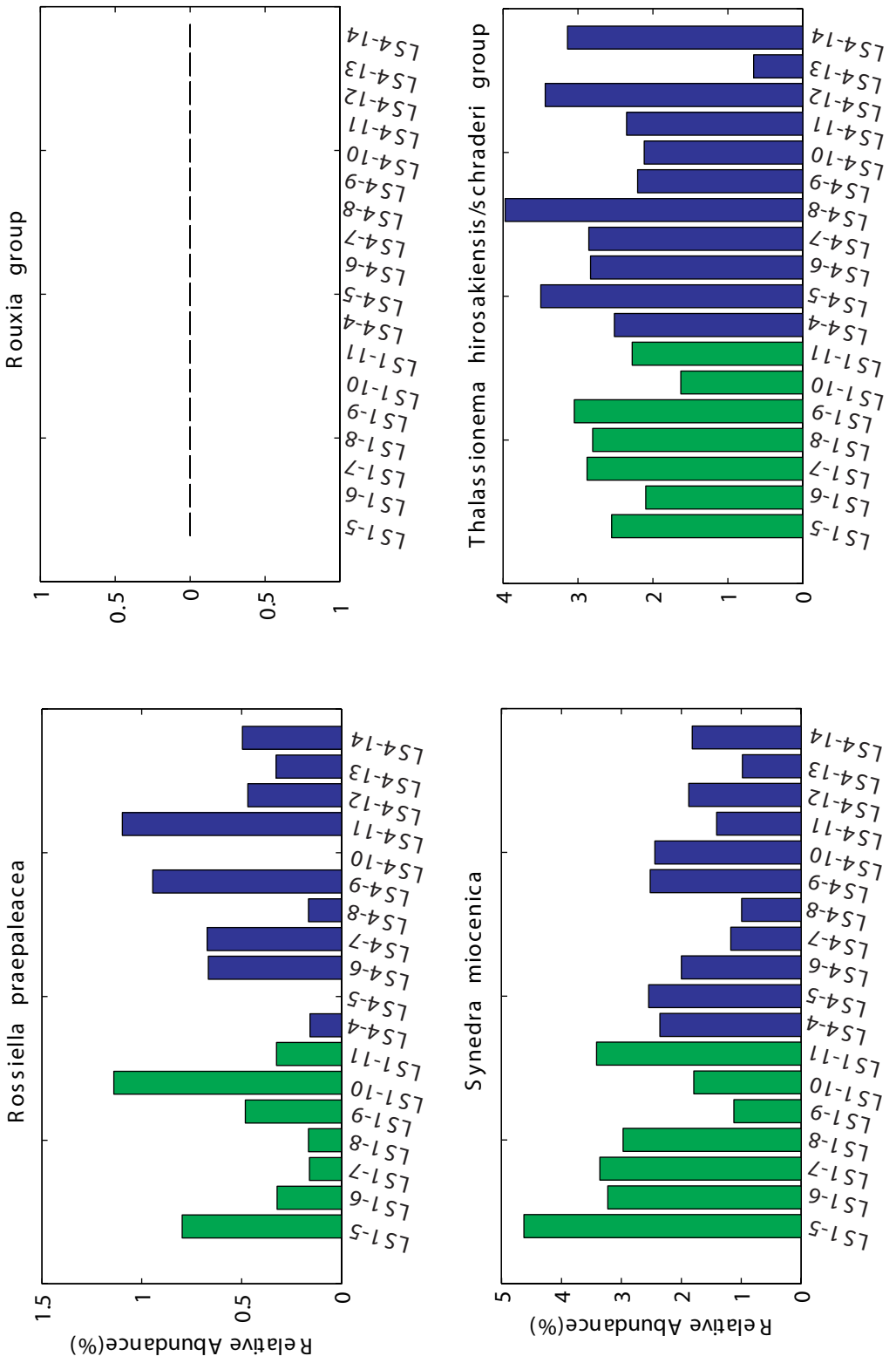

Figure A-4E Individual species relative abundance for LS4 (blue) and LS1 (green) (continued).

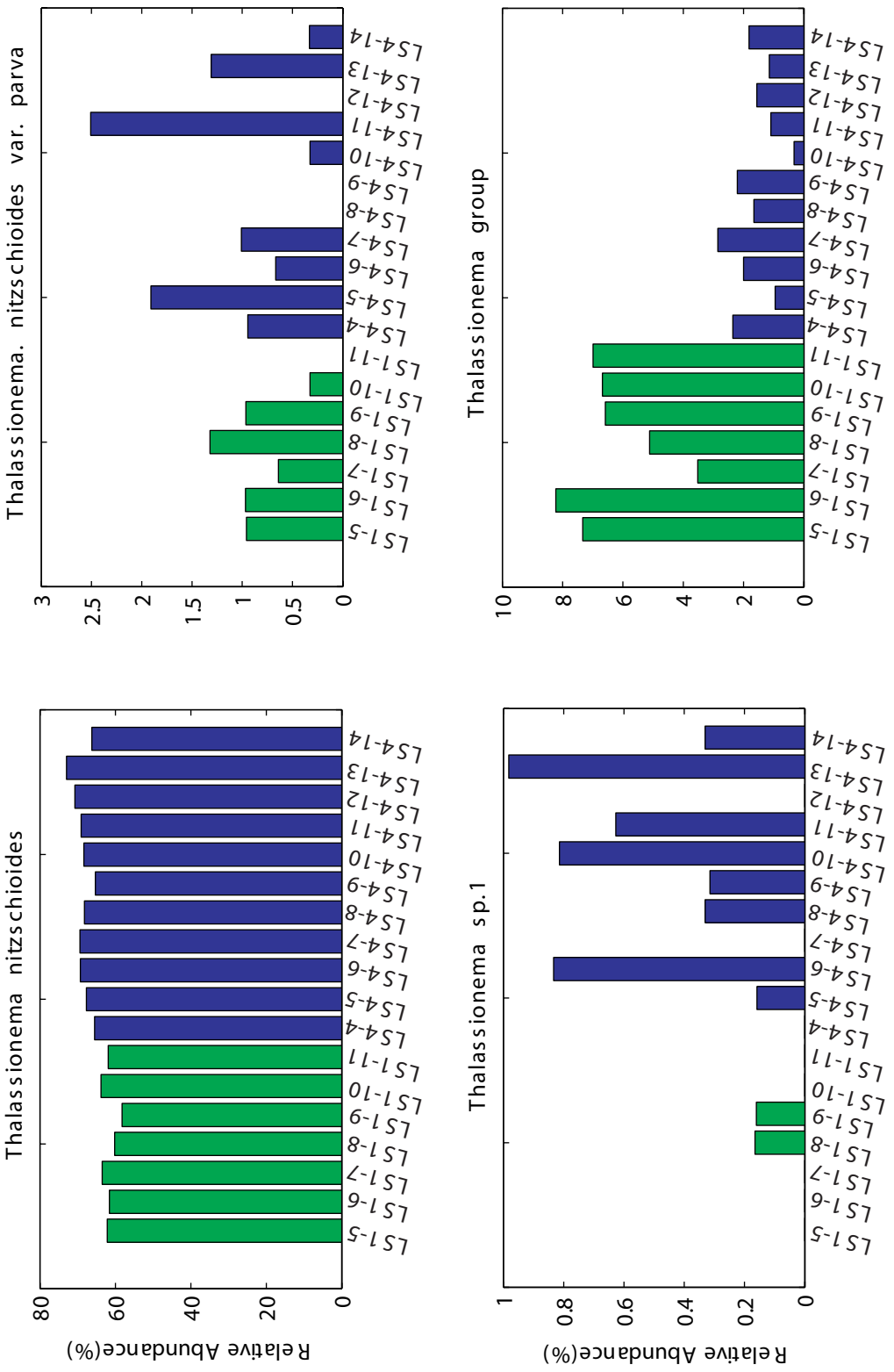

Figure A-4F Individual species relative abundance for LS4 (blue) and LS1 (green) (continued).

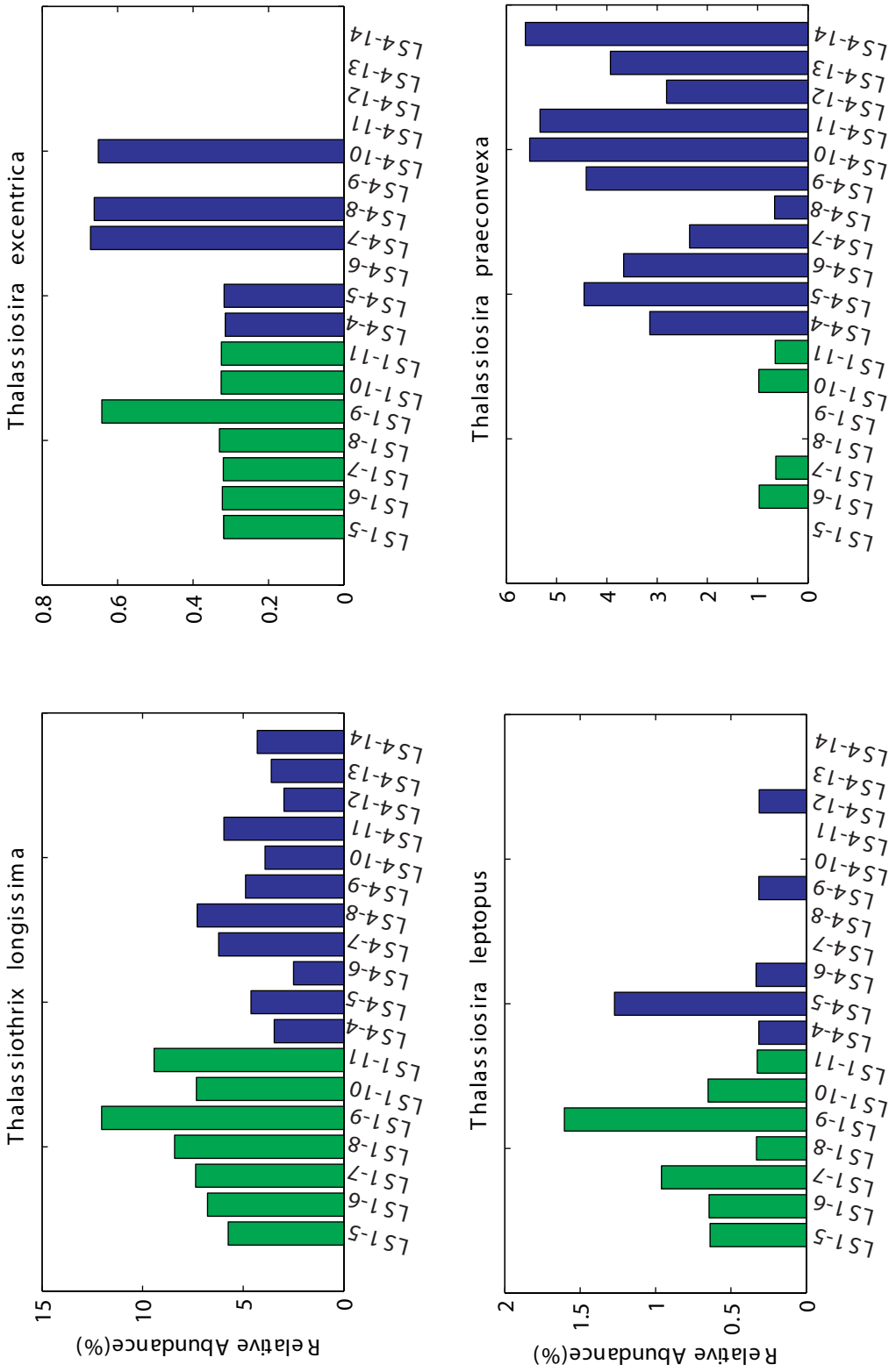

Figure A-4G Individual species relative abundance for LS4 (blue) and LS1 (green) (continued).

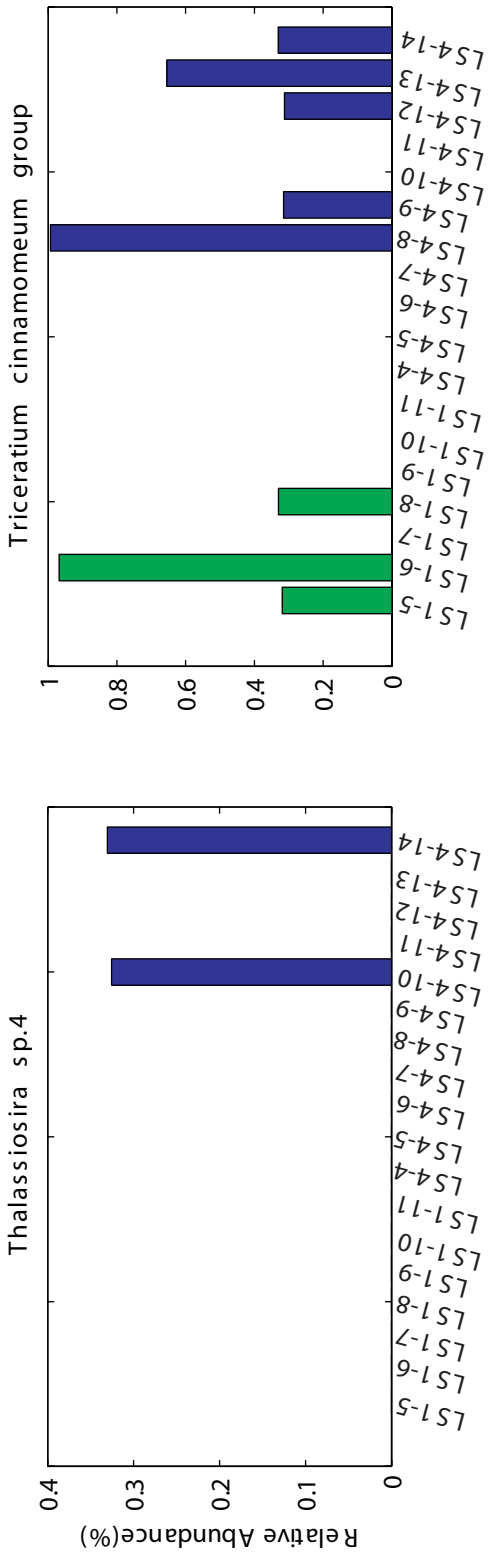

Figure A-4H Individual species relative abundance for LS4 (blue) and LS1 (green) (continued).

APPENDIX B

Floral Reference

Actinocyclus curvatulus Janisch, 1878 *in* Schmidt et al. (1874-1959)
Illustrations: Baldauf (1986) pl. 2, figs. 2, 14; Schrader (1973) pl. 19, fig. 2.

Actinocyclus ehrenbergii Ralfs *in* Pritchard (1861)
Illustrations: Shrader (1973) pg. 783, pl. 19, fig. 1; Schrader (1974) pl. 20 figs. 1,2, pl. 21, fig. 16-17.

Actinocyclus ellipticus Grunow *in* Van Heurck (1883)
Illustrations: Schrader (1973) pl. 8, figs. 7-9, 11-14, 16, 17; Schrader (1974) pl. 17, figs. 4-8, 16.

Actinocyclus ellipticus var. elongatus Grunow *in* Kolbe (1954)
Illustrations: Schrader (1974) pl. 17, figs. 1, 3.

Actinocyclus ellipticus f. lanceolata Kolbe (1954)
Illustrations: Schrader (1974) pl. 17, fig. 2. Barron (1985a) pl. 9, fig. 15.

Actinocyclus moronesis Deby *in* Rattray (1890a)
Illustrations: Schrader (1974) pl. 17, figs. 9-12; Barron (1985b) pl. 7, fig. 5.
Remarks: This species was only observed once, and is assumed to be reworked.

Actinocyclus spp.
Remarks: Consists of three rarely observed forms.

Actinoptychus senarius (Ehrenberg) Ehrenberg
Synonym: *Actinoptychus undulates* (Bailey) Ralfs *in* Prichard (1861)
Illustrations: Schrader (1973) pl. 22, figs. 4, 5, 12, 15.
APPENDIX B, FIGURES B-1 & B-2

Asterolampra acutiloba Frenguelli (1949)
Illustrations: Barron (1985b) pl. 6, fig. 6.

Asterolampra affinis Greville (1862)
Illustrations: Schrader (1974) pl. 9, fig. 10.

Asterolampra grevillei (Wallich) Greville (1860)
Illustrations: Schrader (1973) pl. 21, fig. 3; Schrader (1974) pl. 8, fig. 5.
APPENDIX B, FIGURE B-3

Asterolampra marylandica Ehrenberg (1844b)
Illustrations: Schrader (1974) pl. 8, fig. 2.

Asteromphalus arachne (Brebisson) Ralfs *in* Pritchard (1861)
Illustrations: Shrader (1974) pl. 9, fig. 11.

Asteromphalus sp.1
Remarks: Rarely observed form similar in appearance to *Asteromphalus heptactis* (Brebisson) Ralfs in Pritchard (1861). Illustrations in Gombos (1975) pl. 7, figs. 3, 5; Schrader (1974) pl. 8 fig. 1.

Asteromphalus hookerii Ehrenberg (1844b)
Illustrations: Schrader (1974) pl. 8, fig. 7.

Asteromphalus sp. 2
Remarks: Rarely observed form similar in appearance to *Asteromphalus oligocenicus* Schrader and Fenner (1976) pl. 21, figs. 8, 13, 14, pl. 28, fig. 1.

Asteromphalus robustus Castracane (1875)
Illustrations: Schrader and Fenner (1976) pl. 21, fig. 9.

Asteromphalus symmetricus Schrader and Fenner (1976) pl. 21, figs. 7, 10-12.

Azpeitia biradiata (Greville) Sims *in* Fryxell et. al (1986); figs. IV, V, XXVII – 1-3.

Azpeitia elegantula (Greville) Sims *in* Fryxell et. al (1986); figs. VI, XXVII – 4-5.

Azpeitia nodulifer (Schmidt) Fryxell and Sims *in* Fryxell et. al (1986); figs. XVII, XVIII – 1, 2, 4, 5, XXX – 3, 4.
APPENDIX B, FIGURES B-4 & B-5

Azpietia tabularis (Grunow) Fryxell and Sims in Fryxell et. al (1986); figs. XIV, XV, XXX – 1.

Azpeitia vetustissima (Pantocsek) Sims *in* Fryxell et. al (1986)

Synonym: *Coscinodiscus vetustissimus* Pantocsek (1886)
Illustrations: Schrader (1973) pl. 22, fig. 2; Barron and Baldauf (1986) pl. 2, fig. 6.

Azpeitia voluta (Baldauf) Sims in Fryxell et. al (1986); figs. XII, XXIX – 1.
Azpeitia sp. 1
Remarks: Rarely observed form similar in appearance to *Azpeitia barronii* Fryxell and Watkins *in* Fryxell et. al (1986); figs. XVII – 3, 5, XIX, XX, XXI, XXXI.

Azpeitia sp. 2
Remarks: Rarely observed form similar in appearance to *Azpeitia tuberculata* (Greville) Sims *in* Fryxell et. al (1986); figs. VII, VIII, XXVIII – 1-2.

Azpeitia spp.
Remarks: Consists of two rarely observed forms.

Coscinodiscus radiatus Ehrenberg (1839)
Illustrations: Barron (1985b) pl. 3, fig. 7.

Hemidiscus cuneiformis Wallich (1860)
Illustrations: Schrader (1974) pl. 19, figs. 20-25.
APPENDIX B, FIGURE B-6

Hemialus spp.
Remarks: Consists of two rarely observed fragmented forms.

Mediaria splendida Sheshukova-Poretzkaya (1962)
Illustrations: Schrader (1973) pl. figs. 14, 15; Barron (1985a) pl. 12, fig. 1.

Nitzschia indeterminate group
Remarks: This group consists of poorly preserved fragments with the occasional occurrence of an entire specimen. The species that constitute this group are assumed to be: *Nitzschia cylindrica, Nitzschia marina, Nitzschia miocenica,* and *Nitzschia praereinholdii* with the probable occurrence of intermediate forms such as *Nitzschia sp. 1*.

Nitzschia cylindrica Burckle (1972)
Illustrations: Schrader (1974) pl. 6, 26-34, 36-38.
APPENDIX B, FIGURE B-7

Nitzschia fossilis (Frenguelli) Kanaya *in* Kanaya and Koizumi (1970)
Illustrations: Schrader (1973) pl. 4, figs. 9-11; Schrader (1974) pl. 6, figs. 8-22.
APPENDIX B, FIGURE B-8

Nitzschia fossilis var. 1
Remarks: This form differs from Nitzschia fossilis due to a slight curvature of one margin giving the frustule a semi-crescent shape.

Nitzschia interrupta (Reichelt *in* Kuntze) Hustedt (1927)
Illustrations: Schrader (1974) pl. 15, figs. 1-11.
APPENDIX B, FIGURE B-9

Nitzschia interrupta var. 1
Remarks: Appears to be similar to *Nitzschia sp. 2* Baldauf (1984) pl. 6, fig. 12. Also pictured in Baldauf (1986) pl. 5, fig. 20.

Nitzschia marina Grunow in Cleve and Grunow (1880)
Illustrations: Schrader (1974) pl. 5, figs. 1, 2, 5.
APPPENDIX B, FIGURE B-10

Nitzschia miocenica Burckle (1972)
Illustrations: Akiba and Yanagisawa (1985) pl. 39, figs. 7-15; pl. 41, figs. 1-2.
Remarks: There is a range of morphological variation in this species. Sizes range from 12-60 μm in length and 6-15 μm in width. Also, the specimens observed here have a coarser structure with around 8-10 costae per 10 μm rather than 10-12 costae per 10 μm as reported by previous authors (Burckle 1972; Barron 1985a). Variations such as *Nitzschia miocenica var.elongata* were not counted separately due to the number of incomplete specimens which often made it impossible to differentiate.
APPPENDIX B, FIGURE B-11 – B-15

Nitzschia sp. 1
Remarks: This appears to be an intermediate form between *Nitzschia miocenica* and *Nitzschia cylindrical.* This form differs from *Nitzschia miocenica* due to coarser nature of costae (6-8 in 10 μm), the width between transapical processes (~4 μm apart), and more bluntly rounded apices. However, this species does not have parallel margins like *Nitzschia cylindrica*.
APPPENDIX B, FIGURE B-16 & B-17

Nitzschia sp. 2
Remarks: This appears to be an intermediate form between *Nitzschia miocenica* and *Nitzschia fossilis*. This form differs from *Nitzschia miocenica* due to greater separation between transapical processes (4-5 μm) and a more lanceolate shape with bluntly rounded apices. However, it has coarser costae than *Nitzschia fossilis*.

Nitzschia reinholdii Kanaya and Koizumi (1970)
Illustrations: Barron (1985b) pl. 8, fig. 22; Bauldauf (1984) pl. 4, figs. 5-7; Schrader (1974) pl.

Nitzschia porteri Frenguelli (1949)
Illustrations: Schrader (1973) pl. 5, figs. 35, 36, 39-41, 43, 44.
APPPENDIX B, FIGURE B-18

Nitzschia praereinholdii Schrader (1973) pl. 5, figs. 20, 23-25; Schrader (1974) pl. 7, figs. 24-26; Barron (1985b) pl. 8, fig. 20.
APPPENDIX B, FIGURE B-19

Nitzschia sp. 3
Remarks: This form was only observed once.

Nitzschia sp. 4
Remarks: This form was only observed once.

Pleurosigma sp.
Remarks: Typically, the only portion of the valve observed was the was the central area containing the characteristically large raphe bisecting pore.
APPPENDIX B, FIGURE B-20

Rhizosolenia spp.
Remarks: Included here are various unidentified forms possessing the long apical spine. In most cases, the spine, and the junction between spine and valve were the only parts of the valve observed.
APPPENDIX B, FIGURE B-21

Rhizosolenia barboi group
Remarks: This group consists of *Rhizosolenia barboi* (Brun) Tempere and Peragallo (1908), *Rhizosolenia praebarboi* Schrader (1973) and possibly a few specimens of *Rhizosolenia curvirostris* Jouse (1959).
Illustrations: Schrader (1973) pl. 24, figs. 1-9; Akiba and Yanagasawa (1985) pl. 42-44; Baldauf (1984) pl. 1, figs. 10-12.
APPPENDIX B, FIGURE B-22

Rossiella palecea (Grunow) Desikachary and Maheshwari
Illustrations: Barron (1985b) pl. 8, fig. 2.

Rossiella praepalecea (Schrader) Gersonde
Illustrations: Barron (1985b) pl. 8, fig. 1.
APPPENDIX B, FIGURE B-23 – B-25

Rouxia group
Remarks: This group consists *of Rouxia californica* M. Peragallo in Tempere and Peragallo (1910), *Rouxia diploneides* Schrader (1973) and *Rouxia naviculoides* Schrader (1973). It was rare that anything other than apices were observed for this group. Other species could potentially be included due to the difficulties of identification.
Illustrations: Schrader (1973) pl. 3, figs. 18-32.

Sceptroneis sp.
Remarks: Rare species only observed a few times.

Stephanopyxis dimorpha Schrader (1973) ??
Illustrations: Schrader (1973) pl. 15 figs. 9-11, 19, 20; pl. 16, figs. 1-3, 8-11; pl. 24, fig. 10.

Synedra miocenica Schrader (1976a)
Illustrations: Schrader (1976a) pl. 1, fig. 1; Schrader (1976b) pl. 45, figs. 19-21.
APPPENDIX B, FIGURE B-26

Synedra spp.
Remarks: Rare species only observed a few times.

Thalassionema hirosakiensis/schraderi group
Remarks: This group consists of *Thalassionema hirosakiensis* Schrader (1973) and *Thalassionema schraderi* Akiba in Akiba et al. (1982). These two species were grouped due to difficulty in differentiation especially during the first slides counted.
Illustrations: Akiba and Yanagisawa (1985) pl. 48, 49, 50.
APPPENDIX B, FIGURE B-27 – B-29

Thalassionema nitzschioides (Grunow) Van Heurck (1896)
Illustrations: Akiba and Yanagisawa (1985) pl. 48, figs. 15, 16; Hallegraeff (1986) figs. 1-4.

Thalassionema nitzschioides var. *parva* Heiden and Kolbe
Illustration: Barron (1985a) pl. 8, fig. 10.
APPPENDIX B, FIGURE B-30 – B-32

Thalassionema sp. 1
Remarks: Thinly silicified asymmetrical form.
APPPENDIX B, FIGURE B-34

Thalassionema group
Remarks: This group consists of large heavily silicified forms. Most likely included are *Thalassionema robusta* Schrader (1973), *Thalassionema bacillaris* (Heiden) Kolbe (1955), and *Thalassionema frauenfeldii* (Grunow) Hallegraeff (1986)
Illustrations: Barron (1985b) pl. 8, fig. 14; Hallegraeff (1986) figs. 5a-i, 6-14.
APPPENDIX B, FIGURE B-35 – B-37

Thalassiothrix longissima Cleve and Grunow *in* Cleve and Moller (1878)
Illustrations: Schrader (1974) pl. 19, figs. 6a, 7; Hasle and Semina (1987) figs. 1-25.
APPPENDIX B, FIGURE B-38 – B-40

Thalassiosira antiqua (Grunow) Cleve-Euler (1951) ??
Illustrations: Akiba and Yanagisawa (1985) Pl. 51, figs. 1, 2, 4.

Thalassiosira convexa var. aspinosa Schrader (1974)
Illustrations: Barron (1985a) pl. 11, figs. 8, 12.

Thalassiosira excentrica (Ehrenberg) Cleve (1904)
Synonym: *Coscinodiscus essentricus* Ehrenberg (1839)
Illustrations: Baldauf (1986) pl. 4, fig. 3; Schrader (1974) pl. 11, figs. 5, 7-11.
APPPENDIX B, FIGURE B-41 & B-42

Thalassiosira lepotus (Grunow) Hasle and Fryxell (1977)
Illustrations: Barron (1985b) pl. 5, fig. 5; Barron and Baldauf (1986) pl. 3, figs. 2, 4; Baldauf (1984) pl. 1, fig. 8; pl. 9, fig. 5.
Remarks: There is a great deal of variation in this species which is apparent from illustrations in the lititerature. Two forms were observed during this study: *T. lepotus* sensu Barron (1985b) and *T. lepotus* sensu Barron and Baldauf (1986).
APPPENDIX B, FIGURE B-43 – B-46

Thalassiosira nativa Sheshukova-Poretzkaya (1959)
Illustrations: Schrader (1974) pl. 1, figs. 1, 2, 12, 17, 18.

Thalassiosira praeconvexa Burckle (1972)
Illustrations: Schrader (1974) pl. 2, figs. 6, 7; Barron (1985a) pl. 11, fig 7.
APPPENDIX B, FIGURE B-47

Thalassiosira sp. 1A
Remarks: Similar to *Thalassiosira praeoestrupii* Dumont, Baldauf and Barron (1986) pl. 1, fig. 1.

Thalassiosira sp. 4
Remarks: This species is typically between 10 and 20µm, with a flat valve that slopes sharply at the margin. There are ~10 areolae in 10µm in the center of the valve with a decrease in areolar size towards the margin. This species resembles *Thalassiosira praeconvexa* except is not as convex.
APPPENDIX B, FIGURE B-48

Thalassiosira sp. 7
Remarks: Similar to *Thalassiosira convexa* var. *aspinosa*, however, differs due to linear areolar arrangement and reduction in areolar size towards margin.

Thalassiosira sp. 10
Remaks: This species has a radial, slightly fasciculate areolar arrangement with no apparent reductions in areolar size towards the margin. There are ~6 areolae in 10µm and ~10 marginal striae in 10µm. The most distinguishing characteristic of this form is the irregular appearance of the marginal striae in regard to their orientation to the valve face.

Thalassiosira spp.
Remaks: Consists of approximately 13 forms that were observed rarely, and in some cases only once.

Triceratium cinnamomeum group
Remarks: This group consists of two variations of the species *Triceratium cinnamomeum* Greville (1863) noted in this study (var. 1 & 2), and *Triceratuim cinnamomeum* Greville var. *minor* Grunow *in* Van Heurck (1880)
Illustrations: Schrader (1974) pl. 19, figs. 11-13; pl. 20, figs. 5-11.
APPPENDIX B, FIGURE B-49

Triceratium sp. 1
Remarks: This rare form has a triangular shape with rounded apices and inflections along each margin. Areaolae were large and irregular in orientation. The center of the valve is marked by a very heavily silicified pore.

PLATE 1

Figure B-1 *Actinoptychus senarius* in high plane focus, 35µm (diameter).
Figure B-2 *Actinoptychus senarius* in low plane focus.
Figure B-3 *Asterolampra grevillei*, 50 µm (central area diameter).
Figure B-4 *Azpeitia nodulifer*, 44 µm (diameter).
Figure B-5 *Azpeitia nodulifer*, 157 µm (diameter).
Figure B-6 *Hemidiscus cuneiformis* with focus on margin, 50 µm (long axis).

B-1

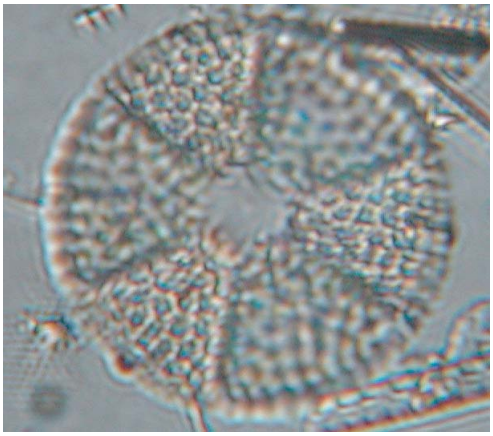

B-2

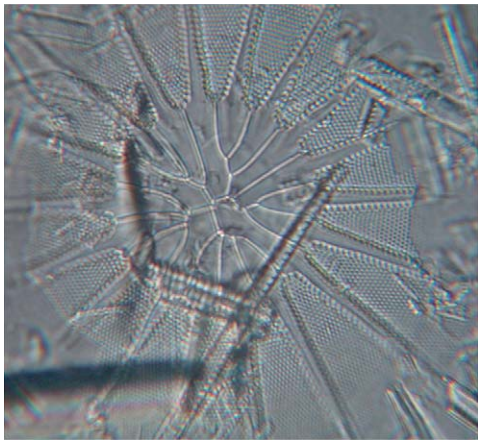

B-3

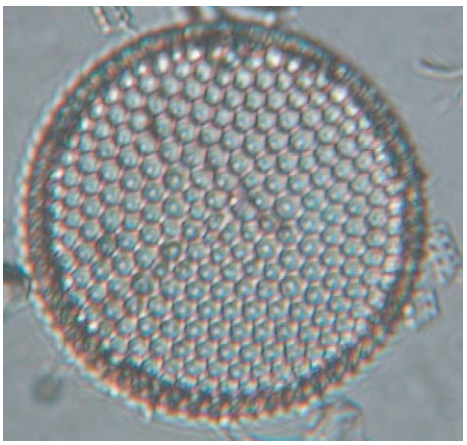

B-4

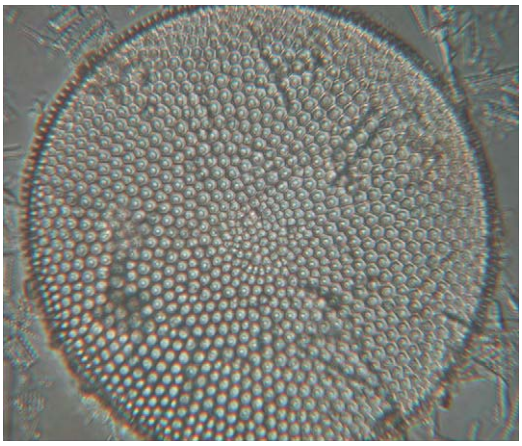

B-5

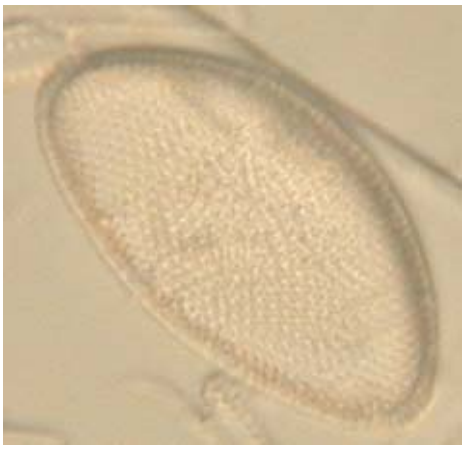

B-6

PLATE 2

Figure B-7 *Nitzschia cylindrica*, 29 µm (apical axis).
Figure B-8 *Nitzschia fossilis*, 42 µm (apical axis).
Figure B-9 *Nitzschia interrupta*, 63 µm (apical axis).
Figure B-10 *Nitzschia marina*, 133 µm (apical axis).
Figure B-11 *Nitzschia miocenica*, 36 µm (apical axis).
Figure B-12 *Nitzschia miocenica*, 64 µm (apical axis).
Figure B-13 *Nitzschia miocenica*, 41 µm (apical axis).
Figure B-14 *Nitzschia miocenica*, 70 µm (apical axis).

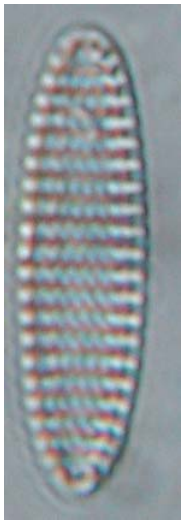

B-7

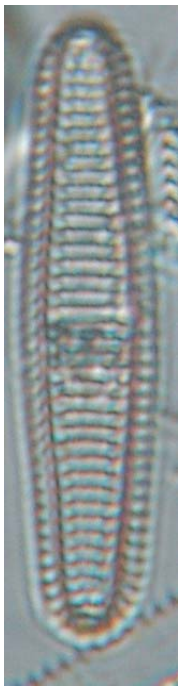

B-8

B-9

B-10

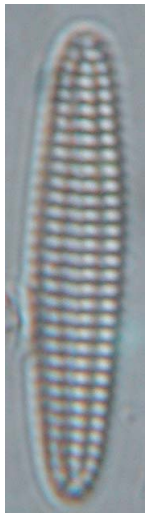

B-11

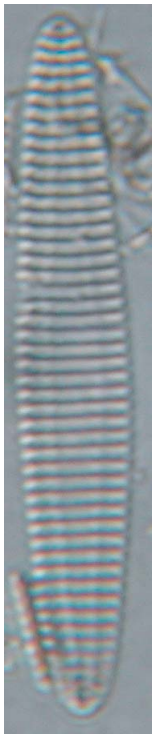

B-12

B-13

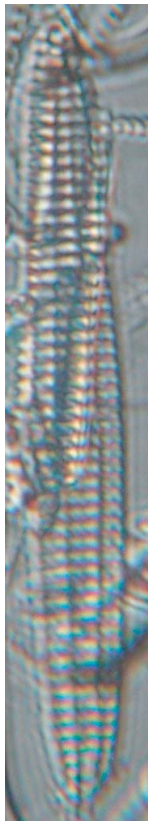

B-14

PLATE 3

Figure B-15 *Nitzschia miocenica*, 13 µm (apical axis).
Figure B-16 *Nitzschia sp. 1,* 25 µm (apical axis).
Figure B-17 *Nitzschia sp. 1,* 23 µm (apical axis).
Figure B-18 *Nitzschia porteri*, 24 µm (apical axis).
Figure B-19 *Nitzschia praerheinholdii*, 83 µm (apical axis).
Figure B-20 *Pleurosigma sp.*, 121 µm (apical axis).
Figure B-21 *Rhizosolenia spp.*, 25 µm (spine length).
Figure B-22 *Rhizosolenia barboi group*, 114 µm (apical axis).
Figure B-23 *Rossiella praepalecea*, 75 µm (apical axis).

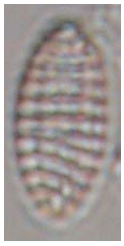

B-15

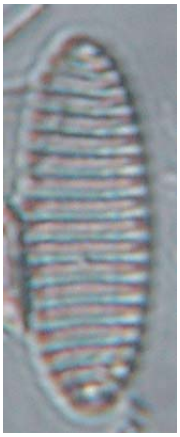

B-16

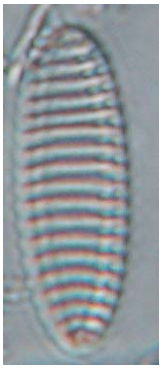

B-17

B-18

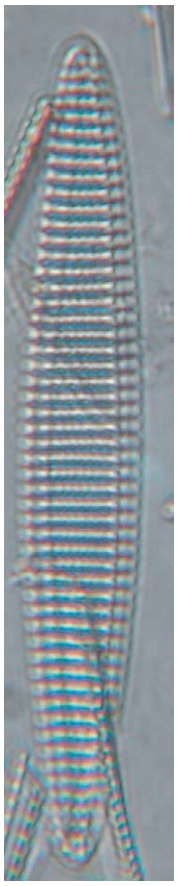

B-19

B-20

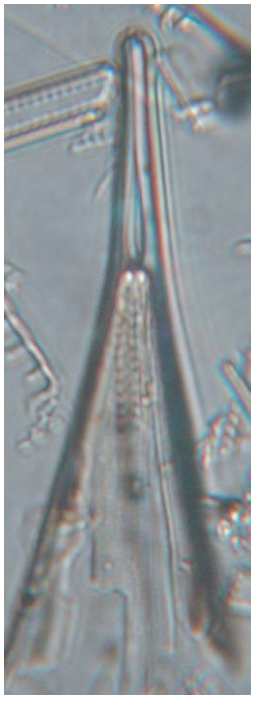

B-21

B-22

B-23

PLATE 4

Figure B-24 *Rossiella praepalecea*, 154 µm (apical axis).
Figure B-25 *Rossiella praepalecea*, 37 µm (apical axis).
Figure B-26 *Synedra miocenica*, 185 µm (apical axis).
Figure B-27 *Thalassionema hirosakiensis/schraderi group*, 43 µm (apical axis).
Figure B-28 *Thalassionema hirosakiensis/schraderi group*, 23 µm (apical axis).
Figure B-29 *Thalassionema hirosakiensis/schraderi group*, 25 µm (apical axis).
Figure B-30 *Thalassionema nitzschioides*, 56 µm (apical axis).
Figure B-31 *Thalassionema nitzschioides*, 88 µm (apical axis).
Figure B-32 *Thalassionema nitzschioides*, 69 µm (apical axis).
Figure B-33 *Thalassionema nitzschioides var. parva*, 8 µm (apical axis).
Figure B-34 *Thalassionema sp. 1*, 39 µm (apical axis).
Figure B-35 *Thalassionema group*, 5.5 µm (tip width).
Figure B-36 *Thalassionema group*, 4.5 µm (tip width).
Figure B-37 *Thalassionema group*, 6.5 µm (tip width).

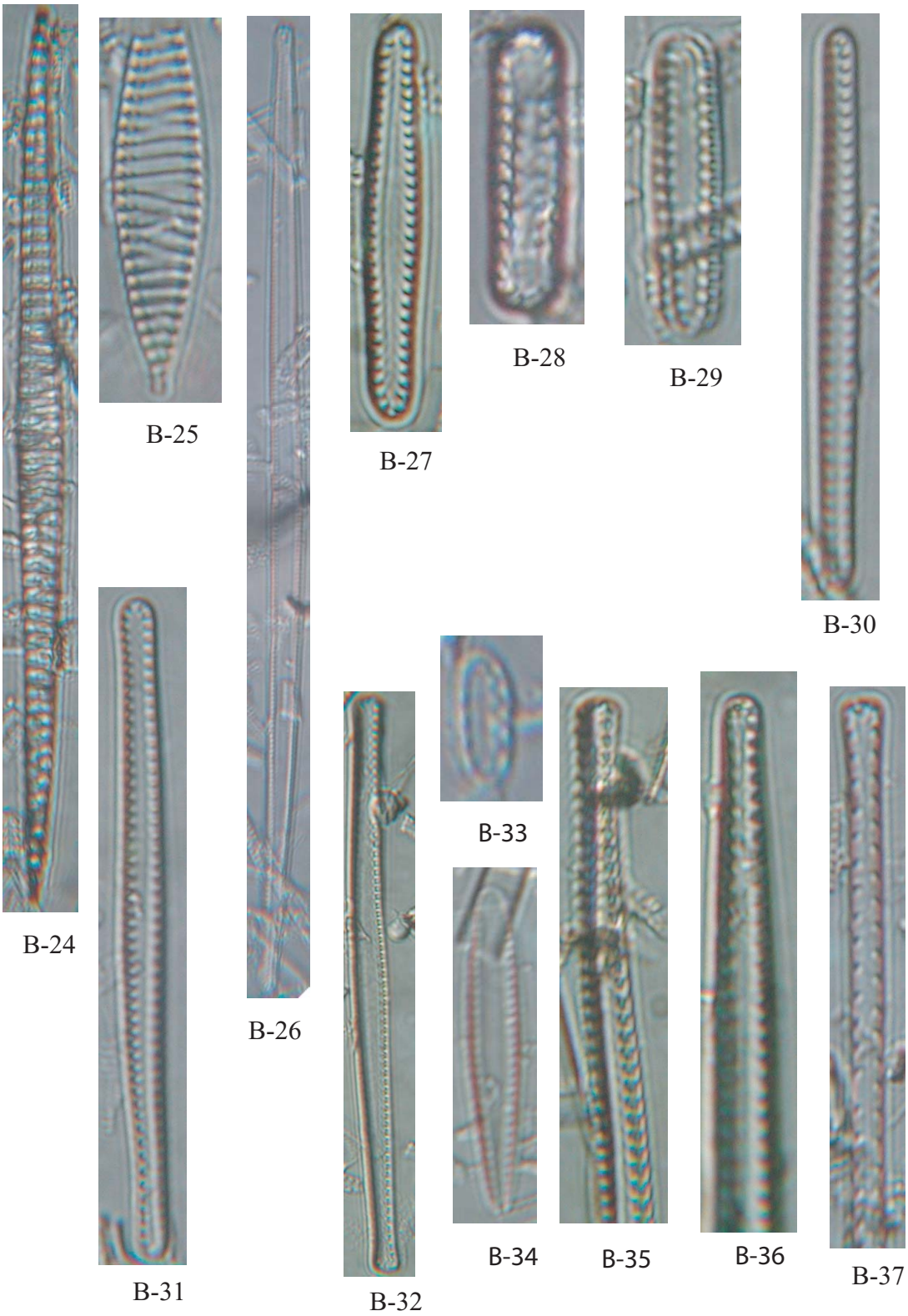

B-24

B-25

B-26

B-27

B-28

B-29

B-30

B-31

B-32

B-33

B-34

B-35

B-36

B-37

PLATE 5

Figure B-38 *Thalassiothrix longissima*, 4.4 µm (spine tip to spine tip width).
Figure B-39 *Thalassiothrix longissima*, 7.7 µm (tip width).
Figure B-40 *Thalassiothrix longissima*, 64 µm (fragment length).
Figure B-41 *Thalassiosira excentrica*, 57 µm (diameter).
Figure B-42 *Thalassiosira excentrica*, 35 µm (diameter).
Figure B-43 *Thalassiosira lepotus*, 61 µm (diameter).

B-38

B-39

B-40

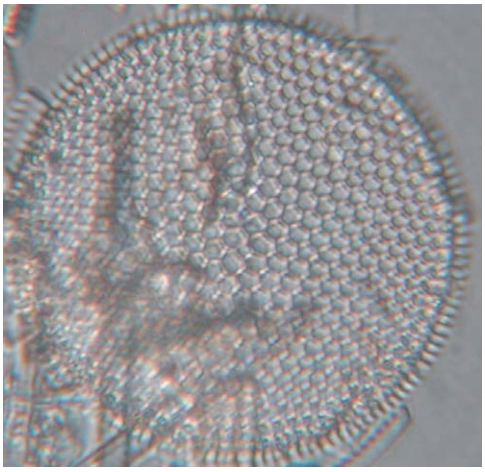

B-41

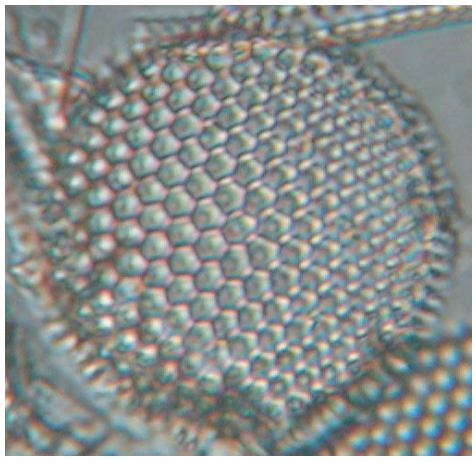

B-42

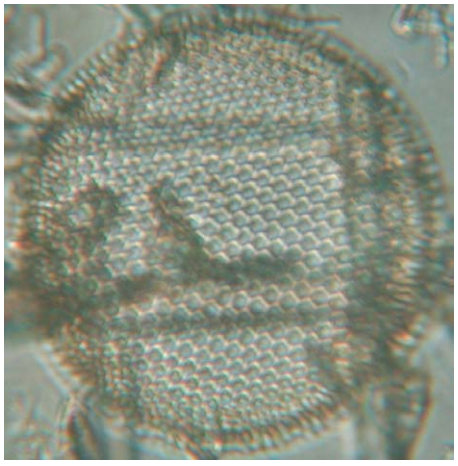

B-43

PLATE 6

Figure B-44 *Thalassiosira lepotus*, 22 µm (diameter).
Figure B-45 *Thalassiosira lepotus*, 24 µm (diameter).
Figure B-46 *Thalassiosira lepotus*, 55 µm (diameter).
Figure B-47 *Thalassiosira praeconvexa*, 29 µm (diameter).
Figure B-48 *Thalassiosira sp. 4*, 35 µm (diameter).
Figure B-49*Triceratium cinnamomeum group*, 118 µm (length from angle to opposite).

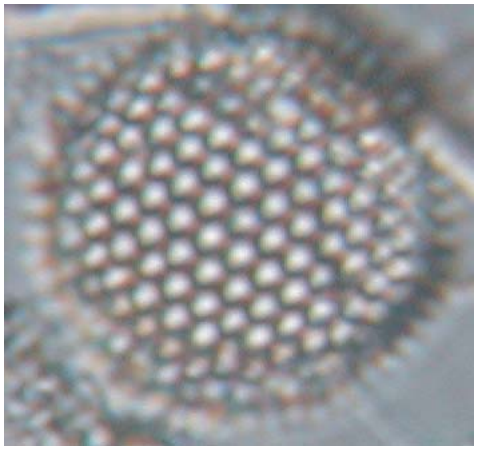

B-44

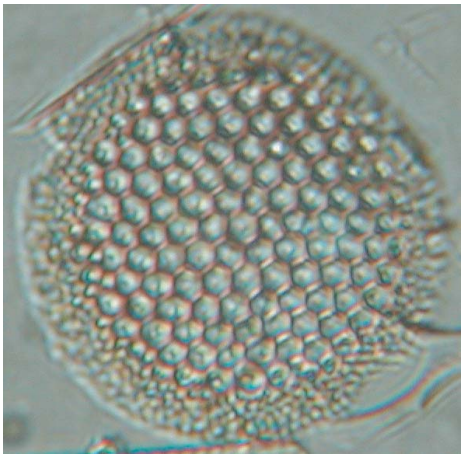

B-45

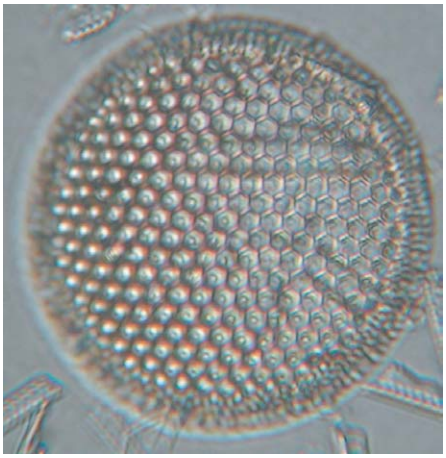

B-46

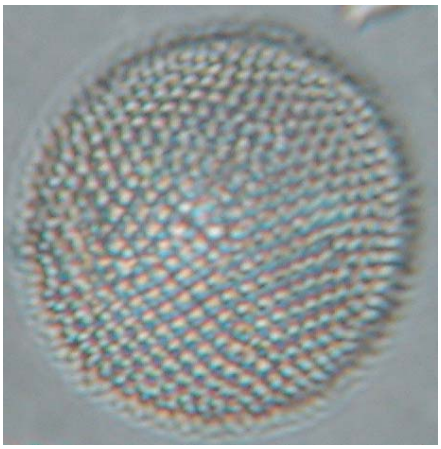

B-47

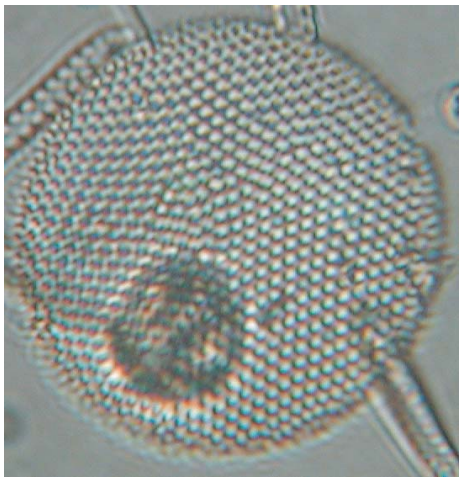

B-48

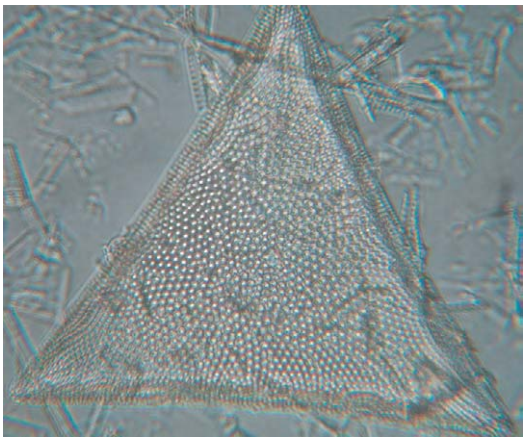

B-49

APPENDIX C

Data range charts are referred to within the text of this thesis. This data is contained within a Microsoft Excel file. The description of the file containing the data is as follows:

Final data range charts.xls – contains three spread sheets consisting of abundance data for the entire sampling range entitled *counts*, *relative* and *absolute*.

VITA

BRIAN NEVILLE BROOKSHIRE JR.
B. S. – Eckerd College 1999
Major: Marine Science

Employment
▪USGS Center for Coastal Geology – St. Petersburg, FL (May 1998 – February 1999)
▪Florida Marine Research Institute – St. Petersburg, FL (January 2000 – June 2000)
▪Texas A & M University – College Station, TX (August 2000 – Present)

Teaching Experience
▪Geology 101 Lab Instructor (TA) – Texas A & M Department of Geology and Geophysics (August 2000 – December 2002)

Field Experience
▪Piston coring
▪Gravity coring
▪Vibra-coring
▪Box coring
▪Side scan sonar data acquisition
▪Water sampling
▪68 days of ship time

Interests
▪Paleoceanography
▪Paleoclimatology
▪Paleoecology
▪Micropaleontology
▪Isotope Geochemistry

Contact Information
Brian Brookshire
Department of Oceanography
O & M Building Room 320
3146 TAMU
College Station, TX 77843-3146